INTERFACIAL CHALLENGES OF ALL-SOLID-STATE LI-ION BATTERIES: MULTI-SCALE COMPUTATIONAL APPROACH

By

Hong-Kang Tian

A DISSERTATION

Submitted to
Michigan State University
in partial fulfillment of the requirements
for the degree of

Chemical Engineering – Doctor of Philosophy

2019

ABSTRACT

INTERFACIAL CHALLENGES OF ALL-SOLID-STATE LI-ION BATTERIES: MULTI-SCALE COMPUTATIONAL APPROACH

By

Hong-Kang Tian

All-solid-state Li-ion batteries (ASSLB) with solid electrolytes (SEs) have enhanced safety and higher volumetric/gravimetric energy density than conventional Li-ion batteries with liquid electrolytes. However, the applications of ASSLB are still limited by the interfacial issues, such as Li dendrite growth through the SEs and the high SE/electrode interfacial resistance. This thesis developed a multi-scale computational approach, combining Density Functional Theory (DFT) calculation and Finite Element Method (FEM), to investigate the interfacial challenges in ASSLB. The Li dendrite growth through pores in SEs and the resulting short-circuit limit the highest current density in ASSLB. The underlining mechanism of Li dendrite nucleation and growth in SEs is still unclear. A DFT model was developed to evaluate the electronic properties of the bulk and surface structures of different SEs. It was revealed that the reduced bandgap and trapped electrons on the pore and crack surfaces are the main reasons for Li dendrite to form. The DFT computed material properties were compared for different SEs, and it was found that the ranked Li dendrite resistance in these SEs, based on the surface electronic properties instead of mechanical properties, is consistent with a broad range of experimental observations. The DFT results also served as the input to a phase-field model, which predicted the formation of isolated Li dendrite that matched with experimental observations. Furthermore, materials design strategies were proposed based on the critical material properties that can resist Li dendrite growth in SEs.

The physically imperfect contact at interfaces is formed during the fabrication process of ASSLB and gets worse during cycling, resulting in high interfacial resistance and damaging to the

battery performance. A 1D FEM battery model was constructed to investigate the relationship between the contact area and the discharging performance. Furthermore, the multi-scale Persson's contact theory was applied to predict the necessary pressure to prevent ASSLB capacity degradation due to contact area loss during the cycling of ASSLB.

Cracked SE and SE/electrode interfaces also increase the impedance in ASSLB. The mechanical degradation of ASSLB is expected to be more severe than that in traditional Li-ion batteries with liquid electrolytes, as the solid-electrolyte also imposes mechanical constraints on the deformation of electrodes. A coupled electrochemical-mechanical FEM model was developed to evaluate the stress development in ASSLB. Two sources of volume change, namely the expansion/shrinkage of electrodes due to lithium concentration change and the interphase formation at the SE/electrode interface due to the decomposition of SEs, were considered. The favorable SE decomposition reactions and the associated volume change were predicted by DFT calculations. It was found that the SE-decomposition induced stress can be much larger than the electrodes volume changes due to Li concentration change, up to tens of GPa, if there are no voids in ASSLB to release some induced-stress. This model can also be used to design 3D ASSLB architectures to minimize the stress generation in ASSLB.

Copyright by HONG-KANG TIAN 2019

ACKNOWLEDGEMENTS

It has been a long and hard but fruitful journey since I came to MSU to start the Ph.D. program in 2015, I could not go this far without the patient mentoring and guidance from my advisor, Prof. Yue Qi. In addition to the professional skills in the world of computational study of batteries, she also taught me a lot in different aspects: the way looking at a bigger picture of the research problems; how to polish and impress others with our work by writing grants and doing presentations; and how to communicate with others and expanding the network in social events. I want to express my most enormous gratitude to Prof. Yue Qi for all her significant amount of help. It is my honor to be guided and received numerous help from my committee, Prof. Carl T. Lira, Prof. Wei Lai, and Prof. Benjamin G. Levine. I would like to thank them for all the helpful mentoring through my Ph.D. comprehensive exam to the defense and thesis writing. It is the critical questions aroused from their intelligent perspectives that make this dissertation more completed. I would like to thank the funding that fully supported my Ph.D. study for four years, Nanostructures for Electrical Energy Storage (NEES), an Energy Frontier Research Center funded by the U.S. Department of Energy, Office of Science, Basic Energy Sciences under Award number DESC0001160; and the Department of Energy, Office of Energy Efficiency and Renewable Energy (EERE), under the Award #DE-EE0007803.

I am also grateful for having many opportunities to collaborate with other excellent research groups, which provided me more insight into understanding science from different perspectives. I want to sincerely thank Prof. Philip Eisenlohr from CHEMS department at MSU for the 3D battery project; Prof. Long-Qing Chen and Dr. Zhe Liu from the Penn State University for the Li dendrite project and the phase-field model; Prof. Gary Rubloff and Dr. Chuan-Fu Lin

from University of Maryland for the FeOF project and grant writing; Dr. Alec Talin and Dr. Kevin Leung from Sandia National Lab for the 3D battery project and the valuable discussion; Dr. Xingcheng Xiao, Dr. Qinglinzhang, and Dr. Jiagang Xu from General Motors for the SEI projects. The lab is the place where I spend most of the time until my baby Riley was born. My lab mates provided me the excellent support for many intelligent discussions on both struggled research and life. I would like to thank Dr. Sungyup Kim, Dr. Tridip Das, Dr. Kwangjin Kim, Dr. Thanaphong Phongpreecha, Dr. Jialin Liu, Dr. Yuxiao Lin, and Dr. Chi-Ta Yang for helping me getting familiar with our lab and teaching me the computational skills. Thank Dr. Christine James for being a great friend not only to me but also to my family as well, and all her encourage and support through my Ph.D. life. Thanks to Dr. Yunsong Li and Dr. Michael Swift for patiently answering me many research-related questions. Thank the younger group members, Jiyun Park, Min Feng, and Yuqin Wu, for your company and help in my last year at MSU.

To my friends out of the lab at MSU and East Lansing, my Ph.D. life would have been arduous and lonely without your company. My CHEMS squads, Sabyasachi Das, Kanchan Chavan, Alex Mirabal, Aritra Chakraborty, and Kirti Bhardwaj, thank you for always making fun of me and insisting that is how you treat good friends. My volleyball family, Kevin Mai, Ana Belza, Pamela Heijerman, and Po-Jen Lin, thank you all for not only having a great team together but also bonding us like a family. Thank Emily Veltri and Anthony Veltri for always friendly sharing American culture with us and trying to learn our Taiwanese culture as well and even organizing a wonderful baby shower party for us. Thank my NCKU friends in the US, Szu-Hao Cho, Chieh-Yin Wang, and Tzu-Yu Lai for coming to Michigan visiting us many times and all the supports. To my beloved family, thank you, Dad (Chi Tien), for all of your sacrifices and love since the day I was born. Thank you, mom (Mu-Dan Luo), I know you have been watching and accompanying

us from heaven. I wish you are here with us. Thank you, my aunt, Ying Tien, for taking care of us two brothers with love like your own kids for over 20 years. And my brother, Hung-An Tian, for your full support physically and mentally. Last but not least, thank you, my wife, Judy, and our cute baby Riley. Your unconditionally support and love are the reasons I am able to face any challenges.

Thank you all for making these four years a savoring journey. I wish you all the best.

TABLE OF CONTENTS

LIST OF TABLE	ESx
LIST OF FIGUR	ES xi
CHAPTER 1. 1.1. 1.2. 1.3. 1.4. 1.4.1.	Background
	An integrated computational approach for interfacial challenges
2.1. 2.2. 2.3. 2.3.1. 2.4. 2.4.1. 2.4.2. 2.4.3. 2.4.4. 2.4.5. 2.5. APPENDIX	Interfacial electronic properties dictate Li dendrite growth in solid electrolytes and how to prevent it by rational design of interlayer materials
CHAPTER 3.	Simulation of the Effect of Contact Area Loss in All-Solid-State Li-Ion Batteries
3.1. 3.2. 3.3. 3.3.1. 3.3.2.	Summary
3.3.3. 3.4. 3.4.1. 3.4.2.	Calculate the contact area under applied load at self-affine rough interfaces84 Results and discussion
3.4.3.	Estimation of needed pressure for recovering the loss of contact area94

CHAPTER 4.	Evaluation of the electrochemo-mechanically induced stress in all-solid-s	state Li-
	ion batteries	99
4.1.	Summary	99
4.2.	Introduction	
4.3.	Computation methods	102
4.3.1.	Battery Architecture	103
4.3.2.	Volume change induced by Li concentration gradient during charging	104
4.3.3.	Volume change induced by the decomposition of solid electrolyte	107
4.3.4.	Stress induced by the volume change from different sources	108
4.4.	Results and discussion	109
4.4.1.	Stress due to Li composition gradient during Charging	109
4.4.2.	Strain due to the Solid Electrolyte Decomposition	113
4.4.3.	Stress due to the Solid Electrolyte Decomposition	114
4.5.	Discussions	118
4.6.	Conclusion	119
APPENDIX		121
BIBLIOGRAPH	Y	124

LIST OF TABLES

Table 2-1. Comparison of the intrinsic material properties of different solid electrolytes47
Table 2-2. Comparison of the cycling results of a symmetrical cell from literature47
Table 2-3. Chemical potentials (eV/atom) used in surface energy calculations64
Table 2-4. Comparison of the surface energy for different surface structures of LATP64
Table 2-5. Calculated surface energy (Jm-2) for t-LLZO slabs with different orientation and termination
Table 2-6. DFT Computed Surface Energy. 67
Table 2-7. Amount of additional electrons in each slab based on difference cross-section area, plotted in Figure 2-2
Table 2-8. Amount of additional electrons in each slab based on difference cross-section area, plotted in Figure 2-6
Table 3-1. The conditions and dependent variables in this model
Table 3-2. The parameters used in this model, which have been fitted to experimental data [94].
Table 3-3. Elastic properties for solid electrolyte and cathode materials
Table 4-1. Grand potential equilibrium phases of Li ₂ PO ₂ N
Table 4-2. The maximum first principal stress in different domains and boundary conditions117
Table 4-3. Parameters used in this simulation

LIST OF FIGURES

Figure 1-1. Comparison of the different battery technologies in terms of volumetric and gravimetric energy density [8].
Figure 1-2. Representation of the Li-ion and electron movement in a battery during charging/discharging [9]
Figure 1-3. Ionic conductivity of ceramics, solid electrolytes, organic liquid electrolytes, polymer electrolytes, ionic liquids and gel electrolytes [19, 20]
Figure 1-4. Comparison of conventional lithium-ion battery and all-solid-state lithium battery at the cell, stack, and pack levels with potentials for increased energy density [30]5
Figure 1-5. Diagram of Li dendrite growth and penetration through solid electrolytes during charging [36]
Figure 1-6. Schematic of the imperfect contact between electrodes and the solid electrolyte after cycling [37]
Figure 1-7. Different types of SEI formed at the solid electrolyte/electrode interface [25]8
Figure 1-8. (Left) SEM image of surface morphology of a sintered pellet made from c-LLZO particles [65]. (Right) Transmission optical microscopy image of polycrystalline β-Li ₃ PS ₄ . Black regions are the Li metal in the solid electrolyte after cycling [52]10
Figure 1-9. Schematic of a cross section in garnet ceramic electrolyte where the potential Li-ion reduction mechanisms are proposed [66]. Li metal forms by plating (a) or dendrite formation and propagation (b) with an electron provided by the external circuit. Li ions reduce by recombination with an electron from the oxygen network (c) or from the residual electronic conductivity (d). Li dendrites and clusters can fill the pores (shades on the drawing).
Figure 1-10. A schematic representation of different battery configurations using solid electrolytes. Current collectors are depicted in grey (positive) and brown (negative), and active materials in pink and green, respectively [93]
Figure 1-11. (Left) An SEM image of an as-produced film-type ASSLB [94]. (Right) SEM images of a bulk-type ASSLB with Li anode and garnet solid electrolyte [95]. Both figures show the poor wettability between electrodes and the solid electrolytes
Figure 1-12. Electrochemical window (solid color bar) of solid electrolyte (green) and other interlayer materials (orange). The oxidation potential to fully delithiate the material is marked by the dashed line [24].

Figure 1-13	3. Schematic diagram about the electrochemical window (color bars) and the Li chemical potential profile (black line) in the all-solidstate Li-ion battery [24]18
Figure 1-14	Cross-sectional SEM images of LAGP after cycling [105]
Figure 1-15	5. Impedance of a different cell as a function of the total amount of charge transferred. The damaged area, measured as the fractional area with visible cracks in the cross-sectional X-ray images, increases concurrently with the cell impedance [42]19
Figure 1-16	5. Theories and physics at different length/time scale, DFT and FEM methods are used in this thesis. The inset images are taken from literature [168, 169]27
Figure 2-1.	The calculated total density of states (TDOS) for the four SE surface structures aligned with the vacuum level. The position of CBM of the corresponding bulk structure is labeled as the cyan dot lines. The position of the vacuum level, and the Fermi level of Li metal (Li E _F), and the potential corresponding to the Li ⁺ /Li ⁰ deposition is labeled. E _{g,surface} stands for the surface bandgap, and T _g is the energy difference from Li-metal in vacuum to the CBM of the SE
Figure 2-2.	The distribution of additional electrons (yellow region), which is calculated from the difference in charge density before and after inserting additional electrons40
Figure 2-3.	Calculated partial density of states for different surface structures, only the states around the CBM are shown
Figure 2-4.	Phase-field simulation results on the impacts of surface trapped electrons and grain size on the morphologies and electric potential distributions after 800s Li electrodeposition in a $500 \times 500 \mu m2$ half-cell. A comparison of the final phase morphologies in (a1-d1) the ideal SEs with excess electron-free surfaces and (e1-h1) the real SEs with the calculated surface electron concentrations from DFT, in a series of grain sizes. And a comparison of their corresponding final electric overpotential distributions for the SEs in (a1-h1). The dynamic evolution of (i) the Li dendrite penetration depths and (j) the total amount of metallic Li in SEs of different grain sizes. The initiation of isolated dendrite nucleation is demonstrated by (k1) the phase morphology and (k2) the corresponding electric potential distribution in the SE of the 75 μm grain size at 200s
Figure 2-5.	Comparison of the TDOS between the bulk and slab structures. (a) Stoichiometric c-LLZO (bulk and slab) (b) Nonstoichiometric c-LLZO slab, (c) Nonstoichiometric t-LLZO slab, and (d) Li ₂ PO ₂ N (bulk and slab). Vertical dash lines stand for the position of Fermi levels, and shaded areas represent the bands that are occupied. The orange arrow points out the additional states.
Figure 2-6.	The charge density difference for different slab structures from (a) top view and (b) side view. Only the positive isosurfaces are shown to illustrate gaining electrons. All isosurfaces are at 0.0001 Å ⁻³ charge density level. In (a), only the atoms (spheres) on the surface are shown.

Figure 2-7.	A schematic of metallic Li ₀ (blue color) formation on the pore surfaces inside of c-LLZO due to the electron pathway provided by the pore surfaces and possibly grain boundaries (subject to modeling in the future). The dashed purple lines represent the Li ⁺ ions passing through c-LLZO, and the red regions represent the excess electrons. Due to the different electronic structures on the pore/crack surfaces, it is proposed that (b) Li ₂ PO ₂ N interlayer will suppress dendrite formation by blocking electrons while (a) t-LLZO interlayer will not.
Figure 2-8.	Proposed future design direction of materials to prevent Li dendrite growth through SEs
Figure 2-9.	The most energetic-favorable surface structure for different solid electrolytes62
Figure 2-10	LATP surface structures with different orientations, terminations, and Al distributions detailed calculation results are listed in Table 2-3 and Table 2-465
Figure 2-11	. Symmetric slab structures of t-LLZO oriented along (a) (110) direction and (b) (001) direction. The labels represent the terminated atoms
Figure 2-12	2. Electron potential in slab cell for different materials from (a) GGA-PBE and (b) HSE06 calculations. V_{vac} stands for the potential at vacuum, E_F is the Fermi level, Vslabinterior is the potential in slab, and Φ is the work function
Figure 2-13	3. Total density of states calculated by DFT HSE06 calculation. Li E _F stands for the Fermi level of Li metal, the vacuum level is plotted as vertical dashed line69
Figure 2-14	. (Top view) The difference of charge density on the stoichiometric surface of c-LLZO, the level of isosurface has been increased to 0.0002 Å ⁻³ 72
Figure 3-1.	Representation of this 1-D model. (a) The considered concepts and (b) the contact between cathode and solid electrolyte
Figure 3-2.	(a) Schematic of the interfacial contact for bulk-type and film-type batteries, and the contact area observed at different length scale. (b) Logarithm relationship between power spectrum and wave number at different RMS roughness [279]. Only the self-affine region is shown
Figure 3-3.	The effect of the contact area on the concentration of Li at electrolyte/cathode interface $(x = 1500 \text{ nm})$ at different discharge time. (a) 1 C-rate (b) 10 C-rate. (c) The open circuit voltage of LiCoO ₂ at different amount of inserted Li90
Figure 3-4.	Discharge curves at (a) $\gamma = 1$ and different C-rate, (b) C-rate = 1 and different γ , (c) C-rate = 10 and different contact factor, γ
Figure 3-5.	The relationship between the discharging capacity and the loss of contact area at cutoff voltage of (a) 3.8 V and (b) 4.0 V

Figure 3-6.	The relationship between the ratio of real contact area to the maximum contact area (A/A_0) and the applied external pressure (σ) for the interface of (a) film-type and (b) bulk-type battery
Figure 4-1.	A schematic that shows the whole idea in this work, a chemo-mechanical model that includes the volume change and resulting stress from the lithiation/de-lithiation and the SEI formation.
Figure 4-2.	2D plane geometry (a) that is rotated around the y-axis to result in the full 3D battery geometry. (b) The electrochemical reactions occur at the two interfaces that are labeled in (a). (c) SEM cross-section image of 2.5D ASSLB [85]
Figure 4-3.	Charging results of the 3D battery at different charging rates, which are to compare with experimental results [85]
Figure 4-4.	Li concentration profile at different charging time at 1.2 C. The arrows in LiPON electrolyte represent the transport direction of Li-ions
Figure 4-5.	Induced first principal stress during charging process for two different cases. The lines represent the direction of the stress. Positive and negative stress mean the tensile and compressive stress, respectively.
Figure 4-6.	First principal stress distribution at different conditions. Lines represent the direction of the stress. Positive and negative stress mean the tensile and compressive stress, respectively.
Figure 4-7.	Comparison of maximum first principal stress from different sources and in different domains at different charging time at 1.2C. The data of 50 nm interphase layer is used in this plot. Decomposition-induced stress occurs before charging the battery119

CHAPTER 1. Background

1.1. Advantages of all-solid-state batteries and challenges

Lithium-ion batteries enabled many applications because of their high gravimetric and volumetric energy density [1], as in Figure 1-1, such as mobile electronics, stationary energy storage systems, and electric/hybrid vehicles, since its first commercialization by Sony in 1990. However, traditional lithium-ion batteries usually use a highly flammable organic liquid as the electrolyte, which results in the safety concerns issue if they are improperly used or crashed [2, 3]. To mitigate the safety concerns entirely, the use of highly flammable organic liquid electrolytes should be avoided. Therefore, all-solid-state Li-ion batteries (ASSLB) with inorganic solid electrolytes have been attracting much attention recently because of its exceptional advantages over liquid electrolytes [4-7]: Increased safety from the use of solid electrolyte, and enhanced volumetric/gravimetric energy from dense packing of ASSLB.

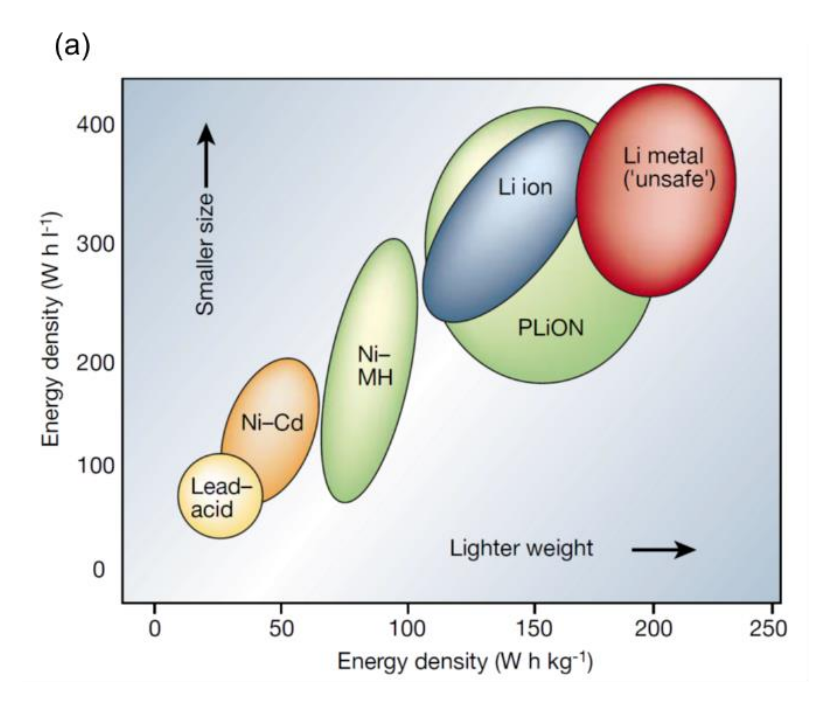


Figure 1-1. Comparison of the different battery technologies in terms of volumetric and gravimetric energy density [8].

The working principles of the Li-ion batteries with either liquid or solid electrolytes are similar. As Figure 1-2 shows, during charging, Li-ions released from the positive electrode via oxidation reaction, diffusing through the electrolyte, getting into the negative electrode via reduction reaction, and the electrons move from cathode to anode through the external circuit. While discharging, all the directions of Li-ions and electrons are reversed. The primary function of the electrolyte should be transporting the Li-ions easily but inhibiting the transport of electron. In traditional Li-ion batteries, the electrolyte is composed of organic liquid and a separator, while in ASSLB, the solid electrolyte serves as the ionic conductor and separator simultaneously.

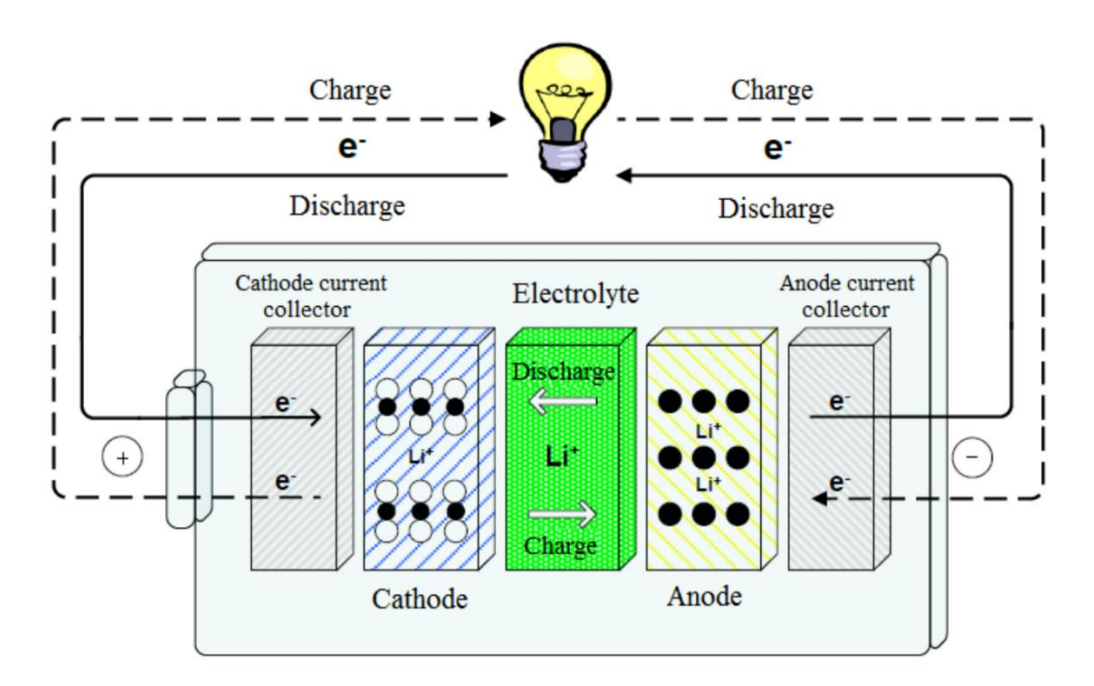


Figure 1-2. Representation of the Li-ion and electron movement in a battery during charging/discharging [9].

The use of solid electrolyte eliminates the safety concern of using an organic liquid electrolyte, as the solid electrolyte does not evaporate and generate organic gas within the battery operating temperature, which is usually up to 60 °C [10]. A primary drawback associated with solid electrolytes used to be the low ionic conductivity. Since the transport of Li-ions in solid electrolytes

was much slower than that in liquid electrolytes, the capacity and the performance of ASSLB used to be limited. With the efforts and improvements in the past decade, several promising solid electrolytes with the ionic conductivity that is similar to the liquid electrolytes, around 10^{-2} S cm⁻¹ at room temperature, have been synthesized and shown in Figure *1-3*. The fast ionic conductors include the garnet-type oxide, NASICON, perovskite, LISICON, Li₃N, sulfide, argyrodite, and anti-perovskite [11-14]. For the solid electrolytes with a lower ionic conductivity (~ 10^{-6} S cm⁻¹ at room temperature), such as LiPON [15-17], making as thin-film ASSLBs can still have a comparable energy density as the liquid electrolytes if the thickness of LiPON can be less than 70 nm [18].

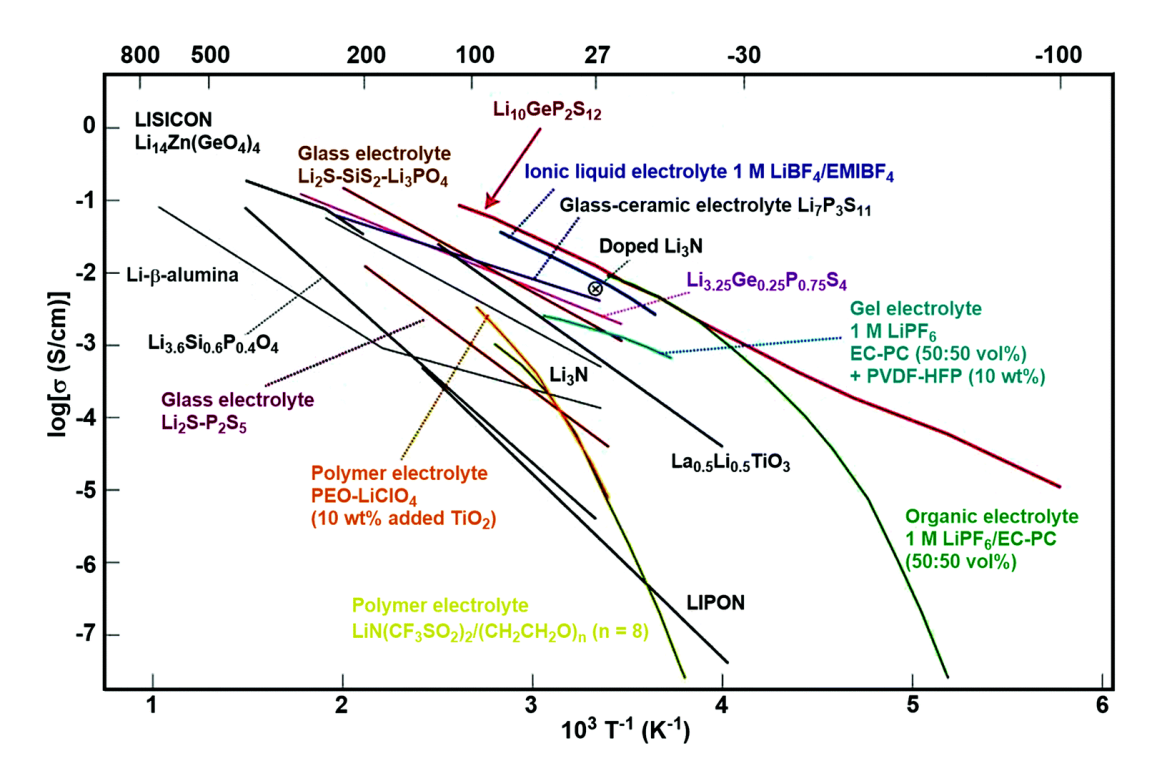


Figure 1-3. Ionic conductivity of ceramics, solid electrolytes, organic liquid electrolytes, polymer electrolytes, ionic liquids and gel electrolytes [19, 20].

Another benefit of using solid electrolytes is the increase of volumetric/gravimetric energy density, as shown in Figure 1-4. First, the organic liquid and separator are replaced by solid electrolytes, which serves as an electrical insulator and ionic conductor at once. Also, It has been proposed that the electrochemical stability of some solid electrolytes enables the use of Li metal as the negative electrode (anode), which increase the volumetric energy density up to 70% compared to the traditional anode material (e.g., graphite [21, 22]), as shown in Figure 1-4 (a) and (b). Li metal also has the highest theoretical capacity (3860 mAh/g⁻¹) and a low anode potential of -3.04 V vs. standard hydrogen electrode (SHE), which gives a higher voltage for the battery [23]. Besides, the better electrochemical stability of solid electrolytes facilitates high-capacity (e.g., sulfur-based) or high-voltage (e.g., LiNi_{0.5}Mn_{1.5}O₄, LiCoO₂) materials as the positive electrode (cathode) [24-29], which further enhance the energy density. At the cell stack level, the liquid electrolyte in conventional soaked Li-ion batteries interconnects to all the components in a galvanic cell [30], which results in the parallel stacking with lots of external current collectors to ensure the separation of each galvanic cell and prevent the interconnection if liquid electrolyte leaks out, as Figure 1-4 (c) shows. In contrast, the solid electrolyte is confined between positive and negative electrodes in a galvanic cell of ASSLB, which makes bipolar serial stacking possible that gives a higher voltage, as shown in Figure 1-4 (d), and there is no need to separate the cells so the volumetric energy can be enhanced. Furthermore, at the battery pack level, due to the flammability of organic solvent in traditional Li-ion battery, a cooling system, as shown in Figure 1-4 (e) is necessary to prevent the thermal runaway and the resulting danger. In ASSLB, such a cooling system can be completely removed since it does not have a safety concern compared to liquid electrolytes. Therefore, ASSLB has a large potential in increasing the volumetric/gravimetric energy density compared to conventional Li-ion batteries.

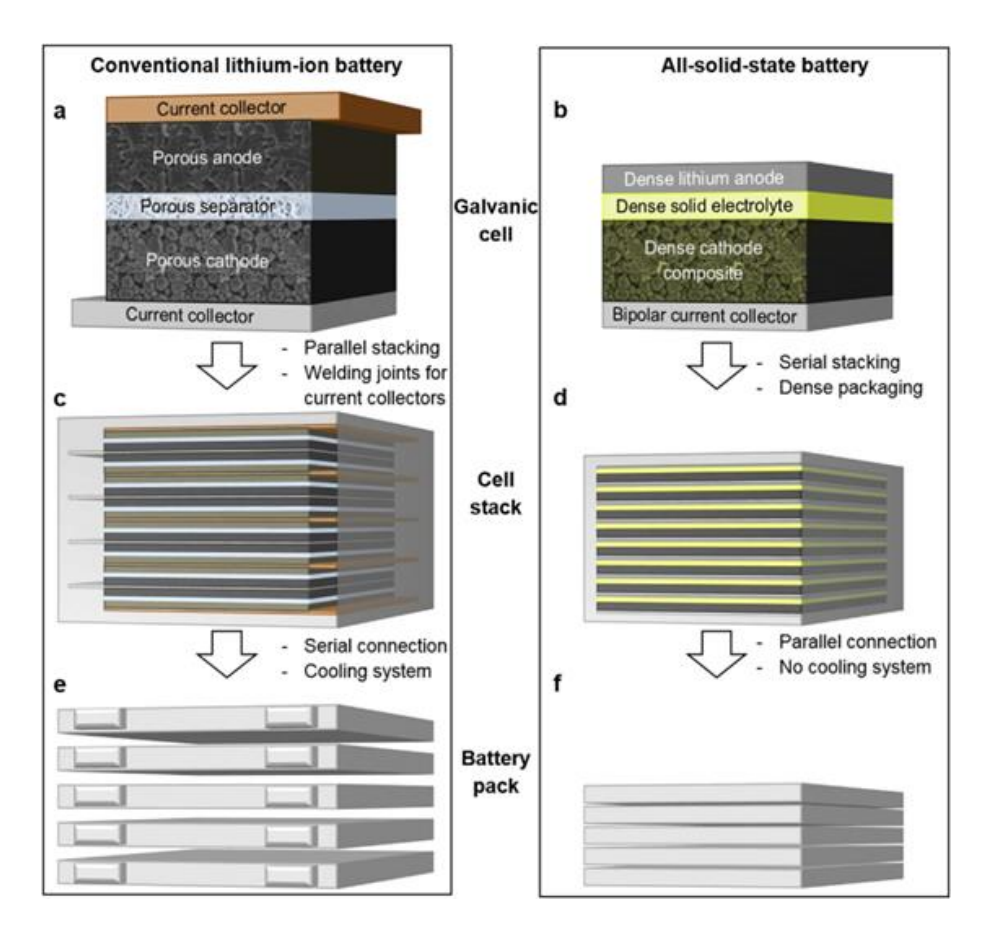


Figure 1-4. Comparison of conventional lithium-ion battery and all-solid-state lithium battery at the cell, stack, and pack levels with potentials for increased energy density [30].

However, there are still some challenges in ASSLB that limit its development and application, which primarily occur at the interfaces, such as solid electrolyte/electrode interface, pore surfaces, and grain boundaries. The interfacial challenges are mainly composed of two issues [18, 31, 32]: Li dendrite growth and penetration through the pores and grain boundaries in solid electrolytes and the high interfacial resistance.

The metallic Li dendrites formation and growth in solid electrolytes happen when cycling the battery, and further penetrate and connect the negative and positive electrode eventually, which causes the short-circuit of the battery, a schematic in Figure 1-5 shows how the Li dendrite may grow and lead to the short-circuit in the end. This phenomenon usually gets much worse and results

in shorter cycling numbers when increasing the current density. Therefore, the Li dendrite problem substantially limits the highest current density of ASSLB, which is around 0.3 mA/cm² [33] in solid-state batteries, much smaller than the typical value of 10 mA/cm² [34, 35] used in traditional Li-ion battery with liquid electrolyte. However, the mechanism and driving force of Li dendrite grow along with the pores and grain boundaries solid electrolytes are still being argued and unresolved. Thus, understanding this Li dendrite growth mechanism in solid electrolytes is necessary for improving the highest current density of ASSLB.

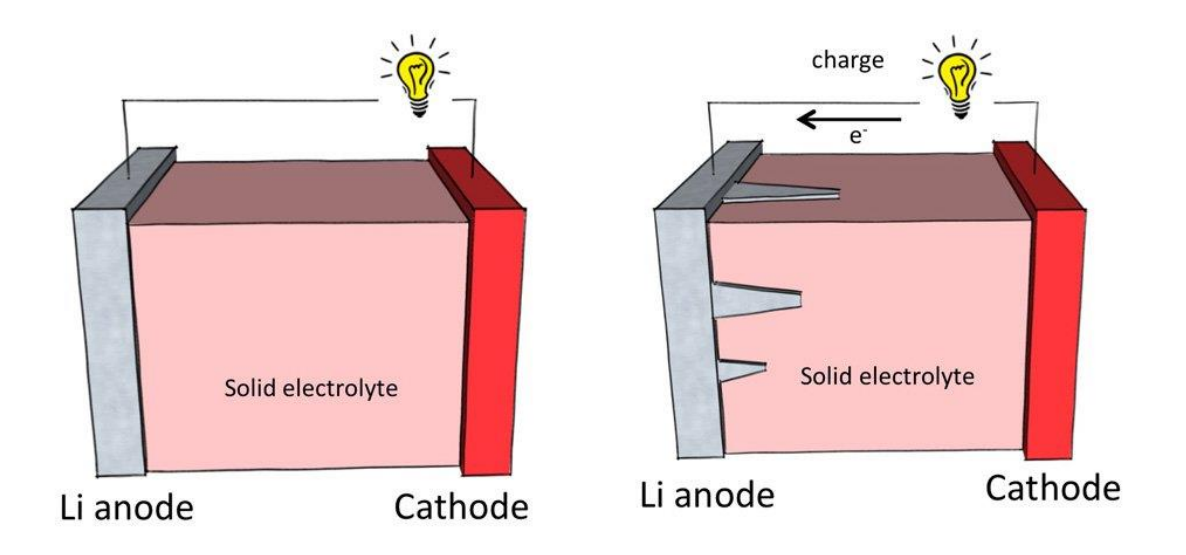


Figure 1-5. Diagram of Li dendrite growth and penetration through solid electrolytes during charging [36].

Another interfacial challenge of ASSLB is the high interfacial resistance that affects the battery performance, which can be divided into the physical effect and chemical effect at the solid electrolyte/electrode interface. For the physical contact issue, since both fsides are solids, usually only point-to-point connection can be obtained at the interface even with the hot pressing process, which leads to a large interfacial resistance and localized electric field during cycling. This physical contact problem would become even worse during battery operation, because both the

volume of the positive and negative electrodes change repeatedly and generate internal stress, which causes the loss of interfacial contact and even delamination between solid electrolyte and electrodes. Figure 1-6 illustrates how the interfacial physical contact loses due to the lithiation/delithiation of electrodes after the cycling of batteries.

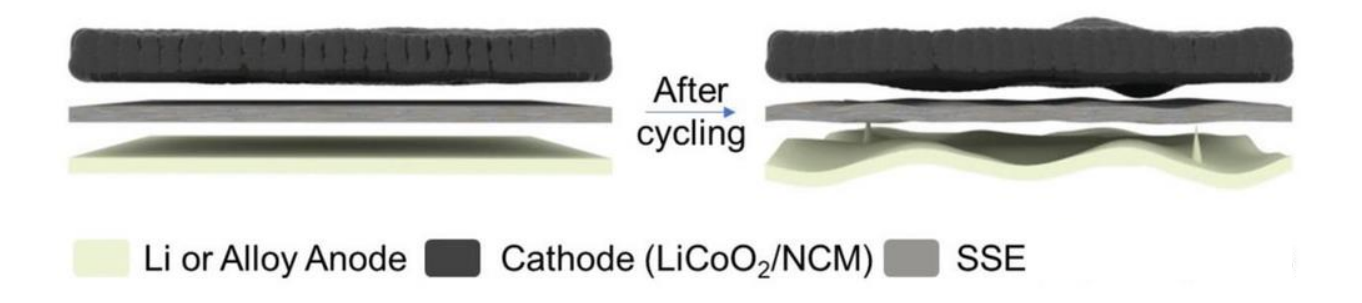


Figure 1-6. Schematic of the imperfect contact between electrodes and the solid electrolyte after cycling [37].

On the other hand, regarding the chemical effect at the solid electrolyte/electrode interfaces, some of the solid electrolytes are found to be electrochemically unstable against Li anode and high-voltage cathodes [24, 25, 38], so it would decompose and form solid electrolyte interphase (SEI) layers at the interfaces. The material properties of the formed SEI vary dramatically depends on the materials used for electrodes and the solid electrolyte and the applied potential [25, 39]. As Figure 1-7 shows there three types of interfaces can be formed: no reaction between solid electrolytes and the electrode; form a mixed ionic and electronic conducting SEI that allows Liions and electrons to pass; an ionic conducting but electronically insulating SEI in that only Liions can get across. Type 1 is the ideal situation, and type 2 is the worst as the electron leakage could result in the continuous growth of SEI [40], which not only consumes available Li-ions but also interfere the Li-ion transport when the thickness of SEI is large enough [41]. Even the Li-ions in type 3 interface is permeable, the ionic conductance could be decreased based on the properties

of the SEI. Furthermore, the formation of the SEI layer could cause a significant volume change due to the decomposition of the solid electrolyte. The induced-stress leads to cracks formation in the solid electrolyte that results in fewer pathways for Li-ions and high interfacial resistance. [38, 42]

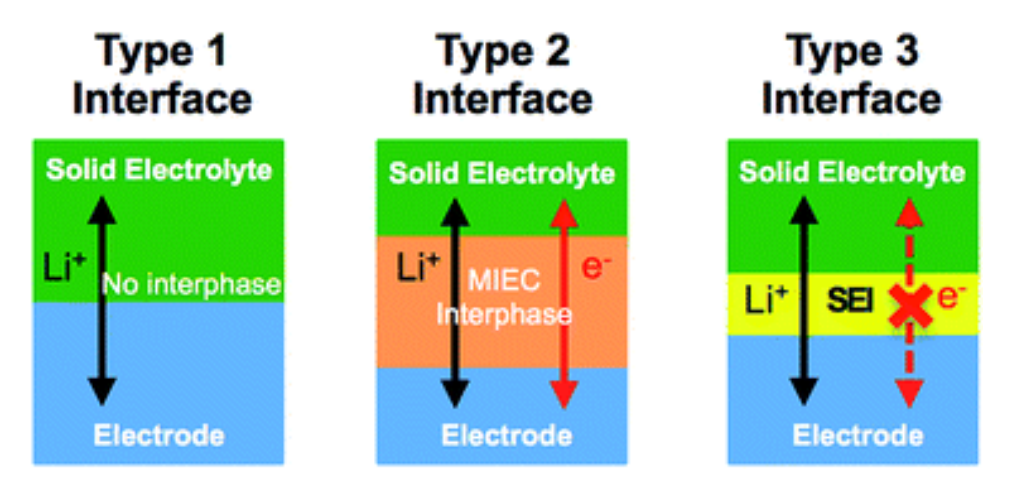


Figure 1-7. Different types of SEI formed at the solid electrolyte/electrode interface [25].

These abovementioned interfacial challenges of ASSLB: Li dendrite growth along with pores and grain boundaries; high interfacial resistance due to physical and chemical effects; have not been adequately tackled and resolved yet. New modeling capabilities are required to reveal the underlining mechanisms in order to solve these interfacial challenges solid-state batteries. In this thesis, multi-scale modeling approaches are developed to address the following key problems a) unrevealing the mechanism of Li dendrite formation and growth in solid electrolytes; b) coupling mechanics and electrochemistry in order to build up the relationship between the interfacial contact area, battery performance, and the applied contact pressure; c) evaluating the chemical-induced stress distribution due to the nonuniform Li concentration in electrodes during charging and due to the decomposition of solid electrolytes at the anode and cathode interfaces in ASSLB. In the rest of the introduction, the current understanding of these interfacial challenges will be discussed

separately in more detail, and the critical research questions will be defined, followed by the need to develop a multi-scale computational approach to address those questions.

1.2. Li dendrites growth mechanisms in solid electrolytes

As the interests in using solid electrolytes increased, a theoretical model proposed by Monroe and Newman [43] that suggested if the shear modulus, G, of the solid electrolyte is two times higher than metallic Li anode, the Li dendrite growth could be suppressed. According to this criteria, many solid electrolytes should be able to prevent the Li dendrite growth, such as β -Li₃PS₄ (G = 6GPa) [44], LiPON (G = 30 GPa) [45], Li_{1.17}Al_{0.17}Ti_{1.83}(PO₄)₃ (LATP, G = 56 GPa) [46], and cubic $\text{Li}_7\text{La}_3\text{Zr}_2\text{O}_{12}$ (c-LLZO, G = 59 GPa) [47]. Nevertheless, many reports have found that Li dendrites still grow in such stiff solid electrolytes, as shown in Figure 1-8, which further caused the short of the electrochemical cell when the current density is higher than certain value (~0.05 mA/cm² for c-LLZO [48-51] and ~0.3 mA/cm² for β-Li₃PS₄ [33]). The highest current density without short, which is also called critical current density (CCD), is much smaller even when using solid electrolytes if comparing with the CCD of liquid electrolyte that is around $4 - 10 \text{ mA/cm}^2$ at room temperature [34, 35]. However, this Li dendrite penetration and short-circuit was not observed in all-solid-state thin-film batteries over extended cycling numbers, such as using LiPON as the solid electrolyte. [29] Thus, the mechanism of Li dendrites grow in solid electrolytes is still unclear and needs to be revealed in order to have a better design of dendrite-free materials.

The Li dendrites have been characterized and found to be growing along with the pores and the grain boundaries (GBs) [52-54], several possible mechanisms have been proposed based on this observation. For example, the Li-ion diffusivity at the grain boundaries was reported to be low that could form dendrites [49, 50, 55]. However, it was also found that increasing the ionic conductivity

of grain boundaries does not improve the capability of surpassing Li dendrite formation. [49, 50] The low relative density was believed as the main reason for Li dendrite to grow along with pores [56], but Li dendrite was still reported to grow in very dense c-LLZO. [57, 58] The pre-existing cracks in the bulk solid electrolytes were also considered to be the reason for Li dendrite growth [59, 60], in which the Li-plating produces crack-tip stresses which drive crack propagation. Nevertheless, this mechanism cannot fully explain why the dendrites form in c-LLZO with different surface roughness at a similar current density. [60]

Many attempts to prevent Li dendrite growth have been tried in terms of the pores and GBs. For example, increase the relative density by sintering and subsequent hot isostatic pressing [61], inserting thin gold layers between Ta-doped c-LLZO pellet and metallic Li anode [56], modifying the grain boundaries of Ta-doped c-LLZO with LiOH to plug the voids [62], or introducing Li₃PO₄ to the internal pores to reduce the interfacial resistance[63, 64]. However, the CCD of the batteries using solid electrolytes is still not comparable with the ones using liquid electrolytes and the commercial requirement, which means the real reason caused the Li dendrite grows in the solid electrolytes is still not fully understood and addressed.

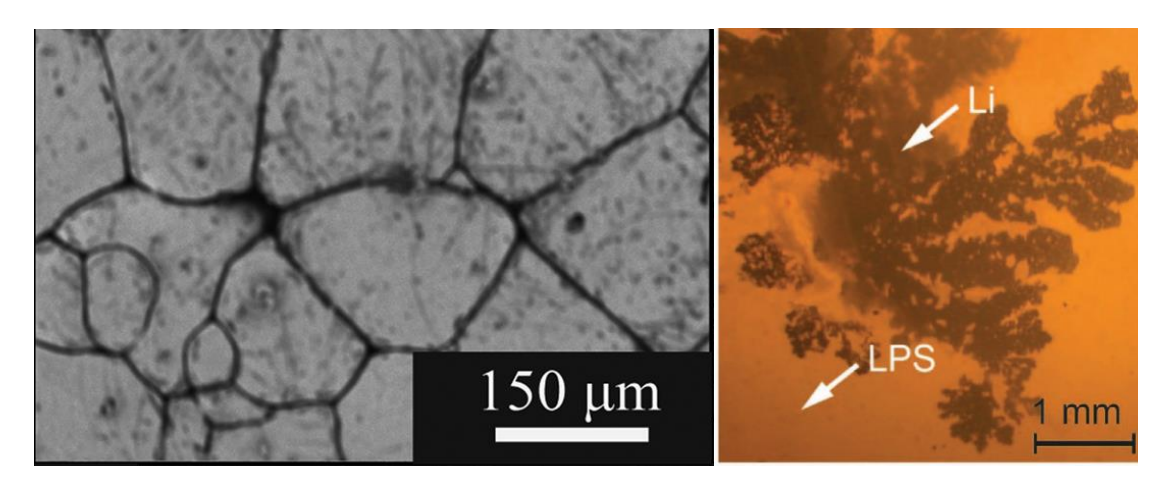


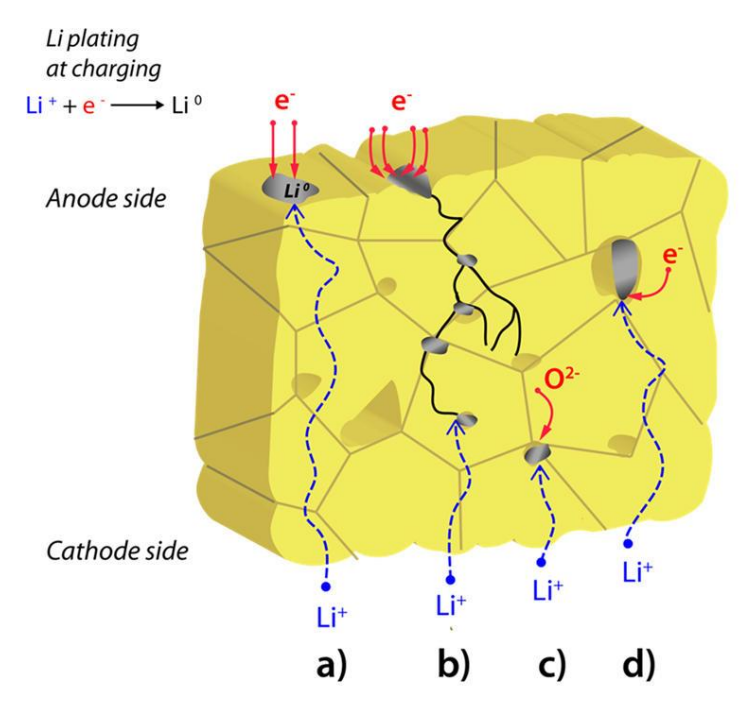
Figure 1-8. (Left) SEM image of surface morphology of a sintered pellet made from c-LLZO particles [65]. (Right) Transmission optical microscopy image of polycrystalline β-Li₃PS₄. Black regions are the Li metal in the solid electrolyte after cycling [52].

In order to design better materials to suppress Li dendrite and further improve the CCD of ASSLB, the underlying reason and the mechanism of Li dendrite growth in the solid electrolyte has to be investigated. As we know, Li-ions must react with excess electrons (e⁻) inside the solid electrolytes to form metallic lithium, Li⁰,

$$Li^+ + e^- = Li^0$$
 Eq. 1-1.

According to Aguesse and Kilner et al. [66], there are four possible ways that Li-ions can obtain electrons, as Figure 1-9 shows: from the Li anode surface; from the propagated Li dendrites; from the oxygen framework, or the residual electronic conductivity. However, there was not enough evidence to show that the Li dendrite growth must be continuous (pathway a and b in Figure 1-9). Until very recently, Han and Wang et al. [51] experimentally reported by time-resolved operando neutron depth profiling that the Li⁰ concentration is uniformed across the whole solid electrolyte during cycling, which implies the formation of isolated Li dendrites. Also, they characterized that the electronic conductivity of c-LLZO and β -Li₃PS₄ is 5.5 x 10⁻⁸ S cm⁻¹ and 2.2 x 10⁻⁹ S cm⁻¹ at 30°C, respectively, which are much higher than what we expected for an electronically insulating electrolyte. Therefore, the pathway d in Figure 1-9 may be the reason for the isolated Li dendrite grows in solid electrolytes. However, there are still some mismatches in the experimental results. According to the Density Function Theory (DFT) calculations with hybrid functional for perfect c-LLZO [67] and β-Li₃PS₄ [68] crystals, the bandgaps are 5.79 eV and 3.7 eV, respectively. This means; theoretically, β-Li₃PS₄ should be more electronically conductive than c-LLZO, but the experiments showed the opposite way. Also, neither should have electronic conductivity on the order of 10⁻⁸ S cm⁻¹ considering the large band gap (> 3.5 eV). This discrepancy suggests that the observed high electronic conductivity, which further causes Li dendrite growth in the solid electrolytes, may not be solely determined by their bulk electronic properties. Instead, the internal

defects, such as pores, cracks, and GBs, may play a critical role in the high electronic conductivity of solid electrolytes and the resulting Li dendrite growth.



- a) Li⁰ plating on electrode
- b) Li dendrite growth and Li⁰ deposition
- c) Li⁰ formation (e⁻ transfer from oxygen framework)
- d) Li⁰ formation (e⁻ transfer from residual conductivity)

Figure 1-9. Schematic of a cross section in garnet ceramic electrolyte where the potential Li-ion reduction mechanisms are proposed [66]. Li metal forms by plating (a) or dendrite formation and propagation (b) with an electron provided by the external circuit. Li ions reduce by recombination with an electron from the oxygen network (c) or from the residual electronic conductivity (d). Li dendrites and clusters can fill the pores (shades on the drawing).

Most of the solid electrolytes mentioned above are ceramics-based electrolytes, in which the internal defects are usually inevitable [69-71]. Extended defects can also be formed during battery assembly and operation [25]. Therefore, understanding the electronic properties of the internal defects in different solid electrolytes is essential for the future design of solid electrolyte material to be free from Li dendrites. In this thesis, four main questions we addressed for different solid electrolyte materials:

- 1. Whether the existence of pore surfaces reduces the band gap of the solid electrolyte that makes excess electrons in the conduction bands?
- 2. Whether the excess electrons stay on the pore surfaces or they move underneath the surfaces?
- 3. Compare the computational and experimental results, can we further determine the critical material properties that dominate the Li dendrites?
- 4. Can we further propose some coating materials or interlayers that may be helpful in preventing the Li dendrite growth?

If we can answer the questions, we would be able to calculate and predict the Li dendrite resistance for many more different solid electrolytes via high through output calculations, and finding the proper materials that may be dendrite-free in ASSLB.

1.3. High interfacial resistance and the causes

Another critical issue when using solid electrolytes is the high interfacial resistance that damages to the battery capacity and performance [37], which can be attributed to the physical and chemical effects. Regarding the physical effect at the solid electrolyte/electrode interface, the mechanical properties of solid electrolytes and the electrodes determine the extent of contact. The solid electrolytes for ASSLB can be classified into polymer-type and inorganic-type. Polymer-type solid electrolytes are composed of polymers and alkali metal salts (such as LiPF₆/LiCF₃SO₃), such as polyethylene oxide, polymethyl methacrylate, polypropylene oxide, polyvinyl chloride, polyacrylonitrile, and polyvinylidene fluoride [72]. Similar to liquid electrolytes that can have perfect contact and wetting on the electrode surfaces, the polymer electrolytes can also generate a close contact toward the electrodes during the assembling of the battery because of the flexible

nature of polymers. However, polymer solid electrolytes usually suffer from the poor ionic conductivity at room temperatures (~10⁻⁶ S cm⁻¹), as shown in Figure *1-3*. On the other hand, inorganic solid electrolytes have much higher ionic conductivity than the polymer electrolytes, and because of their typical ceramic features, these electrolytes usually possess high mechanical strength and are stable in ambient air and at high temperature [73-75]. However, the interfacial contact of inorganic electrolytes with electrodes is poor, not only during the fabrication of the ASSLB but also becoming much worse while cycling of the battery [76]. In order to increase the capacity and further make ASSLB commercialized, using inorganic solid electrolytes with reduced interfacial resistance is a promising direction for ASSLB. Considering that the most inorganic solid electrolytes are ceramics, the dimensional/ volumetric/morphological changes in the ASSLB will be constrained by rigid solid electrolytes.

Also, the fabrication process of ASSLB with inorganic electrolytes plays an important role in the interfacial contact. As shown in Figure 1-10, three main types of ASSLB can be synthesized by different manufacturing processes; the 2D film-type [77, 78], such as using LiPON as the electrolyte; the 2D bulk-type [79-81], such as using c-LLZO and Li₁₀GeP₂S₁₂ (LGPS); and 3D film-type batteries with fully interdigitated electrodes and solid electrolyte architectures [82-84]. There is another type of battery geometry called 2.5D film-type, which is one side with a planar and the other side with a needle-like structure. [85] The contacts between electrodes and solid electrolytes in bulk-type ASSLB are usually non-perfect point-to-point contacts, and the expansion and fracture of electrodes during the cycling process induce contact degradation, resulting in fewer paths for Li-ion transport [86-88]. The film-type ASSLB usually uses the deposition process and forms the amorphous structure with a less rough surface, resulting in a better interface contact. However, even the film-type ASSLB has a better initial contact, during the cycling, the interfacial

contact could still be worsening due to the volume change in the electrodes and solid electrolyte, so as in bulk-type ASSLB. The changes in lattice dimensions, crystal structures, and phase transformations involving both crystalline and amorphous phases of the electrodes upon charging and discharging will result in internal stress development [89, 90]. The stress will be accumulated and cause the fragmentation of electrodes or the delamination of the solid electrolytes from the electrodes [91, 92], as shown in Figure 1-11, in which the interfacial contact between the electrodes (Li and LiCoO₂) and the film-type (Li₃PO₄) and bulk-type (garnet c-LLZO) solid electrolytes are imperfect.

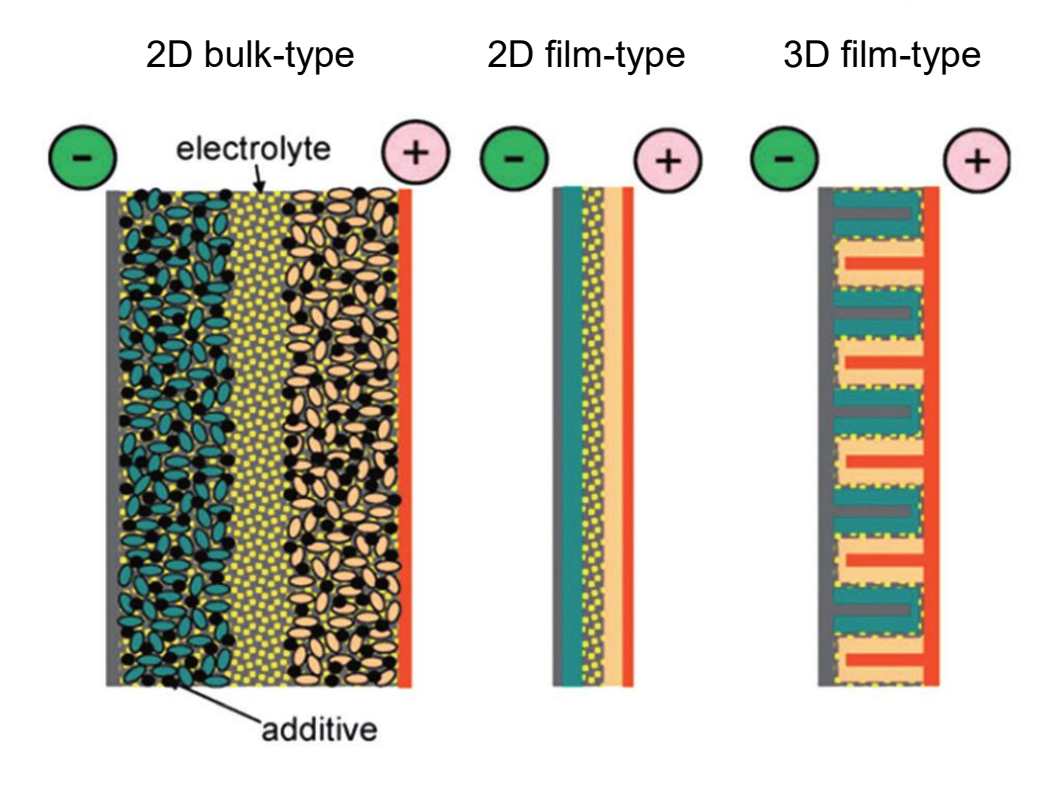


Figure 1-10. A schematic representation of different battery configurations using solid electrolytes. Current collectors are depicted in grey (positive) and brown (negative), and active materials in pink and green, respectively [93].

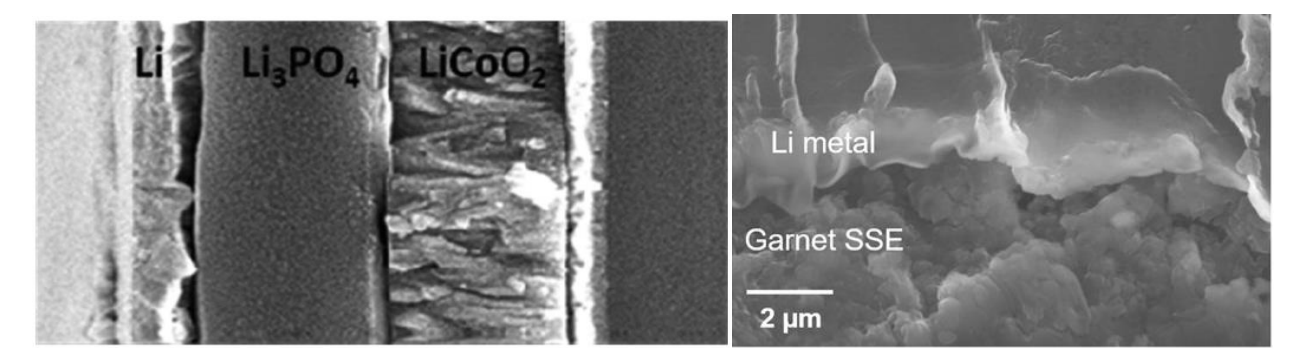


Figure 1-11. (Left) An SEM image of an as-produced film-type ASSLB [94]. (Right) SEM images of a bulk-type ASSLB with Li anode and garnet solid electrolyte [95]. Both figures show the poor wettability between electrodes and the solid electrolytes.

The volume change of the electrodes during cycling can be dramatic. For example, a theoretical volumetric expansion of 179% was calculated when S was lithiated to Li₂S [96], and 263% in volume change when Si was lithiated to Li_{3.75}Si [97]. Frequent Li striping/plating during cycling would cause the loss of contact area between solid electrolytes and electrodes and even separations, as shown in Figure 1-6. A recent study by Li and Kanno et al. [76] investigated the capacity of a bulk-type ASSLB with LGPS solid electrolyte and TiS₂ composite cathode. Even the volume change between TiS₂ and fully-lithiated TiS₂ is only 12% [98], severe drops in the capacity were still observed at the beginning of the cycling, which is due to initial imperfect contact and interphase formation, and also found after cycling that is because of the continuous loss of contact. Also, from their experiments, the degradation of the capacity could be improved by applying a pressure of 228 MPa throughout the electrochemical cycling while maintaining the contact area, which confirmed the importance of the interfacial contact in ASSLB.

On the other hand, the interfacial chemical effect can also generate internal stress that results in the mechanical failure inside both the solid electrolytes and electrodes. The formation of SEI from the decomposition of the electrolytes at the interface is due to the electrochemical instability against electrodes. The SEI issue has been one of the major problems for Li-ion batteries with liquid electrolytes for a long time [99-102], and it was believed that ASSLB could avoid the SEI formation because of the intrinsic electrochemical window (> 3 V). The electrochemical window is the voltage range; within it, the material will not be oxidized nor reduced. A large electrochemical window can prevent electrochemical reactions between electrolyte and electrodes [103, 104]. Until recently, Zhu and Mo et al. [24, 25] reported the theoretical electrochemical window of several solid electrolytes via First principle calculations, as shown in Figure 1-13. It was found that the electrochemical window of most solid electrolytes (green color) is smaller than 2 V, which is similar to that of liquid electrolyte and means the solid electrolyte is not electrochemically stable against most of the electrodes. Nevertheless, they also found that the common interlayer materials of SEI have a relative large electrochemical window that can bridge between the solid electrolyte and the electrode. So, they suggested that the "observed" wide electrochemical from the solid electrolytes is actually beneficial from the kinetic stabilization of SEI, solid electrolytes, and electrodes at the interfaces that extend the electrochemical window, as Figure 1-13 shows.

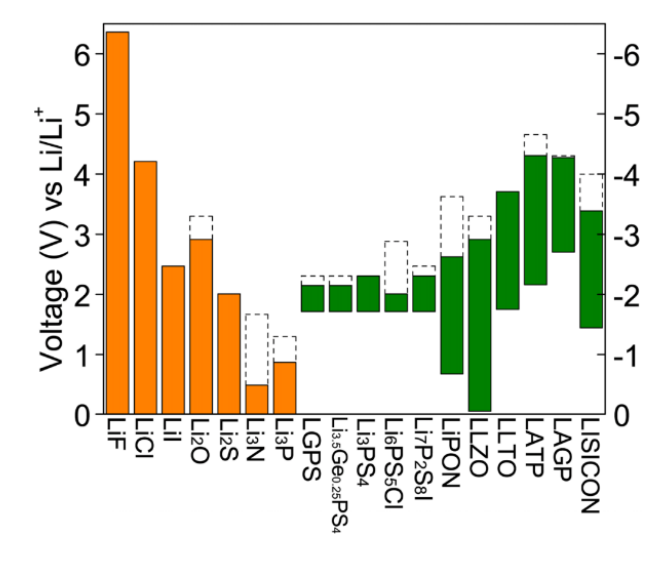


Figure 1-12. Electrochemical window (solid color bar) of solid electrolyte (green) and other interlayer materials (orange). The oxidation potential to fully delithiate the material is marked by the dashed line [24].

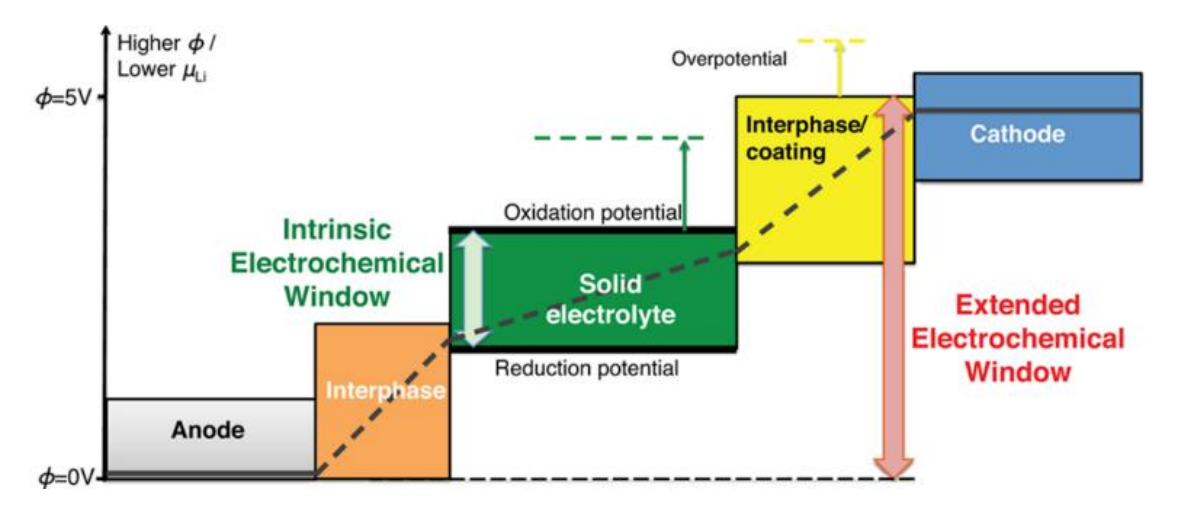


Figure 1-13. Schematic diagram about the electrochemical window (color bars) and the Li chemical potential profile (black line) in the all-solidstate Li-ion battery [24].

Therefore, one can conclude is that most of the solid electrolytes are likely to decompose at the interface of electrolyte/electrode, which can also generate internal stress in ASSLB due to the volume change from the decomposition of solid electrolytes. Chung and Kang et al. [105] and Lewis and McDowell et al. [38] both observed that there are black SEI layers formed at the interface between LAGP and Li in a Li|LAGP|Li symmetrical cell after electrochemical cycling. Also, cracks and fractures were generated after the SEI formed and were seen via SEM, as in Figure 1-14, which shows an SEI layer on the top surface of the LAGP surface and cracks inside of it. The volume expansion of LAGP to the SEI layer was calculated to be as high as 273% [42]. It was also found that a massive increase in impedance after the cracks formed due to the interfacial transformations and volume expansion. As a strong relationship shown in Figure 1-14, the impedance of the LAGP solid electrolytes is increased with the amount of crack (damaged area). Therefore, the electrochemical instability of solid electrolytes against electrodes and the resulting volume change and the induced-stress can be severe enough to increase the interfacial resistance.

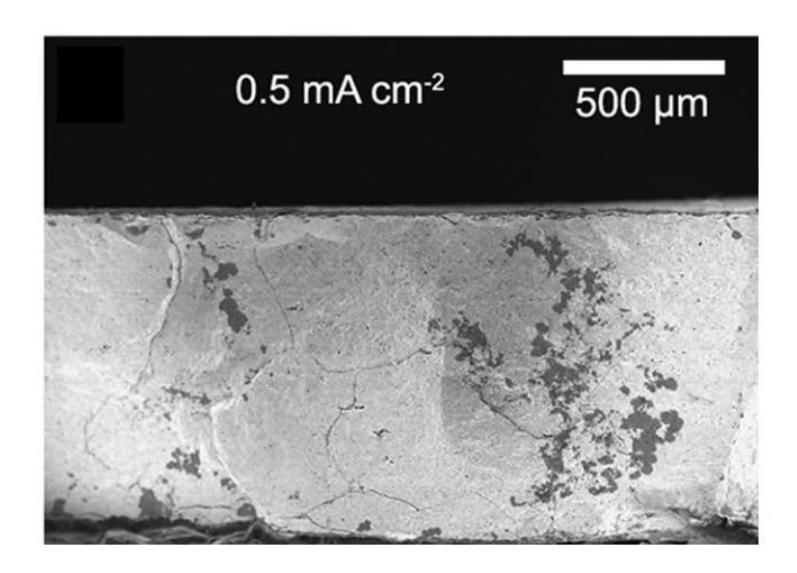


Figure 1-14. Cross-sectional SEM images of LAGP after cycling [105].

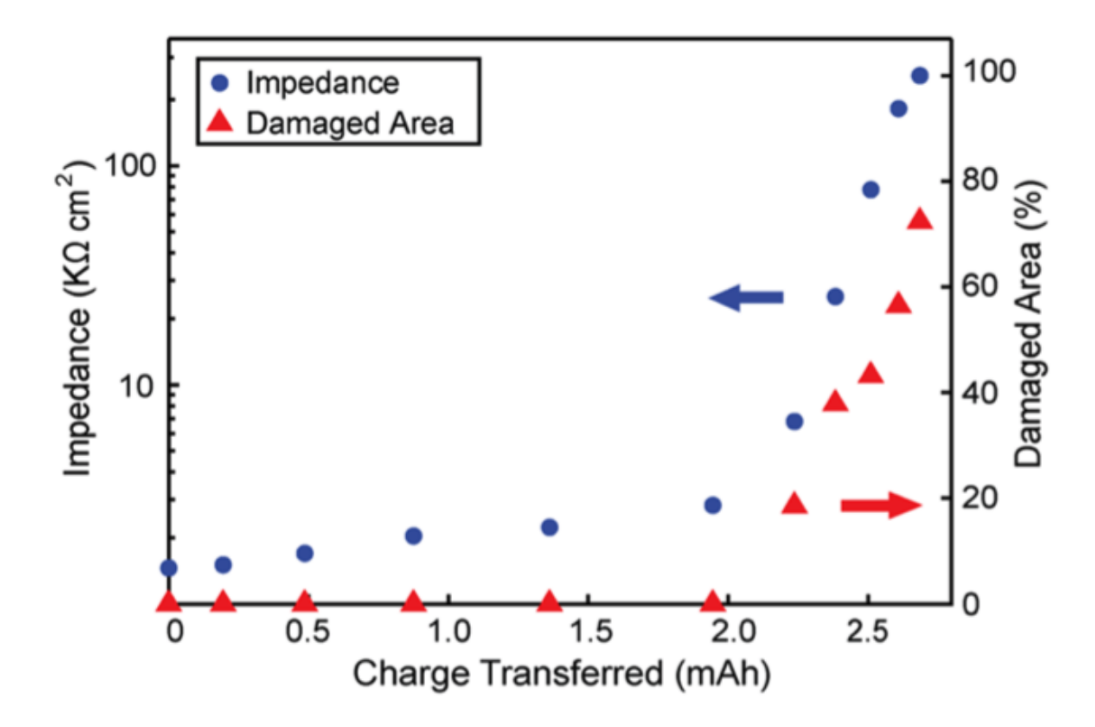


Figure 1-15. Impedance of a different cell as a function of the total amount of charge transferred. The damaged area, measured as the fractional area with visible cracks in the cross-sectional X-ray images, increases concurrently with the cell impedance [42].

Both the physical and chemical effects mentioned above can cause the volume change and generate internal stress that results in the mechanical failures in ASSLB. Several attempts have been tried

to improve the mechanical failures. For example, depositing a buffer layer by pulsed laser deposition (PLD) technique or atomic layer deposition (ALD) between solid electrolyte and electrodes [106-109], preparing nanocomposites by a ball milling process to reduce the particle size [110, 111], increasing the surface area and utilization of supercooled liquid of glass electrolyte [112], and applying high pressure throughout the fabrication process and electrochemical cycling [76]. However, there are still unresolved challenges regarding the mechanical failures induced from the volume change in ASSLB:

- 1. In practical use, can we distinguish how much of the contact area lost while cycling, and further evaluate how much pressure should be applied to recover the contact area and capacity? It is also expected that different material combinations in ASSLB would have a different suitable range of applied pressure. Can we predict the necessary pressure for different materials?
- 2. Can we predict which parts of the ASSLB are more likely to have mechanical failures due to the cycling and the decomposition of solid electrolytes, based on different battery architectures? Several ASSLB geometries have been synthesized to improve the diffusion of Li-ions between electrodes [113], such as 2D thin-film batteries [16] that has planar geometries, 2.5D architecture [85], and 3D geometry [82-84]. The induced-stress and its distribution could be largely non-uniformed and different based on architecture. If we can predict the areas that are more likely to have cracks, appropriate methods or coating materials can be designed to prevent mechanical failures.

1.4. Multi-scale computational approach

Quantitative modeling needs to be developed in order to address the research questions raised in sections 1.2 and 1.3. With the improvement of computer ability in the past decade, it is now possible to calculate the targeted materials based on different physics and theories at different length/time scale, from the quantum level to the continuum level, as shown in Figure 1-16. In this thesis, we conducted combined multi-scale simulations, which include first-principles Density Function Theory (DFT) and Finite Element Method (FEM) [114], for different research problems. Each method has its strengths and limitations.

1.4.1. Quantum mechanics - Density Functional Theory (DFT)

Quantum mechanics describes atomistic interactions and energies based on electronic structures based on solutions of the Schrödinger equation [115] as the equation below, through reasonable approximations.

$$\widehat{H}\psi = E\psi$$
 Eq. 1-2,

where \widehat{H} is the Hamiltonian operator, ψ is the state vector of the quantum system, and E is a constant equal to the energy level of the system. The exact solution of the Schrödinger equation is extremely difficult to be solved for systems comprising more than one electron. Several quantum mechanics methods have been developed based on different treatments for the electron-electron correlations and approximations, such as Hartree–Fock (HF) [116], Møller–Plesset Perturbation theory (MPn) [117], Coupled Cluster (CC) [118], Configuration Interaction (CI) [119], Multi-Configurational Self-consistent Field (MCSCF) [120], and Density Functional Density (DFT) [121, 122]. Normally, the theory with higher accuracy requires a longer time and more expensive computation resources. Regarding the battery materials, DFT is a suitable method [123] to yield

accurate material properties, such as lattice parameters, formation energy, open-circuit voltage, diffusion activation energy etc., with reasonable computing time for many classes of materials. Plane-wave DFT imposes periodic conditions for the computation cell, which are efficient for crystal materials up to several hundreds of atoms. DFT was first developed in 1964 by Hohenberg and Kohn [122]; they determined that all ground-state properties can be expressed as a function of the charge density that must be minimized in energy. Kohn and Sham further modified DFT in 1965 [121] by expressing the most complex electron interactions with an "exchange-correlation" functional. Even the exact form of the exchange-correlation functional is still unknown, approximations based on electron gas models and further extensions have been successful for many classes of materials [124].

DFT was first applied to the battery-related problems in the 1990s by Ceder et al. [125-127], in which they are the first to demonstrate that DFT could be used to calculate the open-circuit voltage of the batteries that determines the energy stored per unit charge. With the connection, DFT was used to predict the promising electrode materials, such as doping Al into layered LiCoO₂ could enhance the voltage [126]. Moreover, some other DFT-computable properties have been developed successfully, such as phase stability, thermal safety, and Li-ion diffusion [128-130]. To optimize the transport of Li-ions, DFT can be used to calculate the energy barrier of migration of Li-ions and to make suggestions for the design of materials, such as Kang et al. [131] computed the effect of LiMn_{0.5}Ni_{0.5}O₂ layer spacing on Li-ion migration barriers. They found that even small expansions of the layer spacing could produce significant improvements in Li diffusivity. The prediction was also adopted to experimentally synthesize new electrode materials by the ion exchange of Li for Na in NaMn_{0.5}Ni_{0.5}O₂, which has been found to have increased energy and power density [131]. Similarly, Ong et al. [132] calculated the stability of LGPS solid electrolyte

by DFT and predicted the effects of different cation/anion doping on the phase stability, electrochemical stability, and Li-ion conductivity. Regarding the Li-ion conducting mechanism in different solid electrolytes, Mo et al. [133] applied DFT and *Ab initio* molecular dynamics (AIMD) for different solid electrolytes, such as LGPS, LATP, and c-LLZO. They found that the fast diffusion in super-ionic conductors does not occur through isolated ion hopping, as is typical in solids. Instead, it proceeds through concerted migrations of multiple ions with low energy barriers. Also, Curioni et al. [134] used DFT and nudged-elastic band (NEB) calculations to identify the Li-ion diffusion mechanisms responsible for the considerable difference in ionic conductivity between the tetragonal and the cubic phases of LLZO. Hence, DFT is capable of addressing and investigating the research problems that relate to the mechanism, electronic properties, phase stability, and help for exploring new materials. Most of these DFT examples consider bulk materials with perfect crystals, although the properties of interfaces and surfaces can also be tackled by DFT, they have not been explored extensively for materials in ASSLBs.

Despite the widespread popularity and success of DFT for battery-related calculations, its application can still be limited and suffer from significant pervasive errors, which cause qualitative failures in predicted properties. The errors mostly come from the approximate exchange-correlation functionals that are hard to construct and have remained elusive. The major limitation of DFT comes from the delocalization error of approximate functionals, which is due to the dominating Coulomb term that pushes electrons apart [135]. Furthermore, typical DFT calculations cannot adequately describe degenerate or near-degenerate states, such as the breaking of chemical bonds, arise in transition metal systems, and strongly correlated materials. Therefore, regarding the battery materials, especially that have elements with electrons in d-orbital, the DFT

cannot completely capture the electronic properties. Also, DFT treats materials as perfect crystal that may miss the full configurations in reality, such as defects and amorphous structures.

Since DFT calculation is at the quantum level that is around several nanometers, and the affordable numbers of the atom are up to several hundred, the propertied obtained from DFT may not be able to connect to the real batteries directly, as shown in Figure 1-16. Therefore, a combined multiscale computational approach is needed to bridge the gap between calculations at different lengthscale. In this thesis, FEM calculations were also conducted to connect the DFT-calculated properties to the battery cell-level phenomena.

1.4.2. Continuum modeling – Finite Element Method (FEM)

Continuum modeling is necessary to simulate battery performance at the range of micro-meter to meters and microseconds to hours [136]. Several continuum models have been developed and applied for battery modeling, each of which makes use of its methodology to achieve specific targets. For example, Peukert's law [137, 138], which was published in 1897, is the first theory that relates the available capacity of a lead-acid battery to the discharge rate for a constant current discharge. Electrical and analytical models include dynamic characteristics of the battery, from nonlinear open-circuit voltage, current, temperature, cycle number, and storage time-dependent capacity to transient response in Li-ion batteries [139-141]. Modeling batteries by equivalent circuit simulate the battery with a combination of variable resistors, voltage sources, and capacitors [142-144], such as Thevenin equivalent circuit models [145], runtime-based models [146], impedance-based models [144]. A widespread class of model is based on the Cahn-Hilliard theory [147] and called the phase-field model, which smears the phase boundary in a narrow region of finite thickness, avoiding localized discontinuities. In the phase-field model, the dynamics of phase

segregation is ruled by the Helmholtz free energy of the system, which includes interface energy that relates to the gradient of concentration. The phases in batteries, such as interphase layers, pores, grain boundaries evolution in electrodes, and electrolyte, are able to be calculated via the phase-field model [148-150]. Another common class of model is based on the numerical method, such as Finite Element Method [114] and Finite Difference Method [151]. FEM subdivides the targeted geometry (1D to 3D) into tiny but finite-sized elements of geometrically simple shapes, each element is mathematically represented by partial differential equations (PDEs) that describe the physics. So, it gives an approximate local description of the physics by a set of simple linear/nonlinear equations. The difference between FEM and FDM is typically defined on a regular grid, while FEM can be used for more irregular geometries.

Within the continuum modeling methods, FEM is selected in this thesis to investigate the interfacial mechanical problems in ASSLB, as FEM can simultaneously simulate different battery architectures from 1D to 3D, the Li-ion transports within solid electrolyte and electrodes, and the electrochemical reactions at the interfaces. A well-known pseudo-two-dimensional (P2D) model based on FEM to describe the internal behavior of a lithium-ion battery was developed by Doyle and Newman et al. [151] in 1993, which is also called Newman battery model. This P2D model includes a sandwich battery structure, porous electrodes, a separator, and current collectors, and solves for the electrolyte concentration, electric potential in electrodes, electrolyte potential within the separator, solid-state potential, and solid-state concentration within the porous electrodes. The electrochemical reactions are described by Butler-Volmer kinetics [152]. This physics-based P2D model is by far the most used by battery researchers, leading to the development of many similar models [153-162]. Some continuum models have been developed for ASSLB as well. For example, electro-chemo-thermal models to couple the heat generation and transfer during the ASSLB

operation [163, 164]; including the dynamic double layer effect and Stern layer potential drop in the ASSLB simulation [165]; model the particle size, overpotential, and strain dependence of phase transition pathways in storage electrodes [166]; electro-chemo-mechanical model for the ASSLB with composite electrode, in which the electrode particle deformation was modeled during the cycling [167].

In FEM, the properties of the material are assumed as continuous across different elements in the model, so the size and the numbers of meshes affect the accuracy and the calculation time. Also, except particularly specify, in FEM, the condition is assumed as ideal, which means no imperfections, defects, interlayers in the material. To model the ASSLB more accurately at the continuum level, it may be necessary to include the non-ideal properties, such as the internal defects, SEI layers, and double layers, to be included as input parameters. Furthermore, some parameters in FEM may be difficult to be obtained separately and accurately by simply fitting to the experimental data, such as rate constant, reaction energy barrier, and diffusivity. Instead of doing experiments, some of the abovementioned properties and parameters can be approximated through DFT calculation, and serve as input back to FEM. Therefore, in this thesis, DFT calculation and FEM will be combined to address the interfacial problems in ASSLB, such as predicting the volume change from the decomposition of solid electrolytes due to the electrochemical instability.

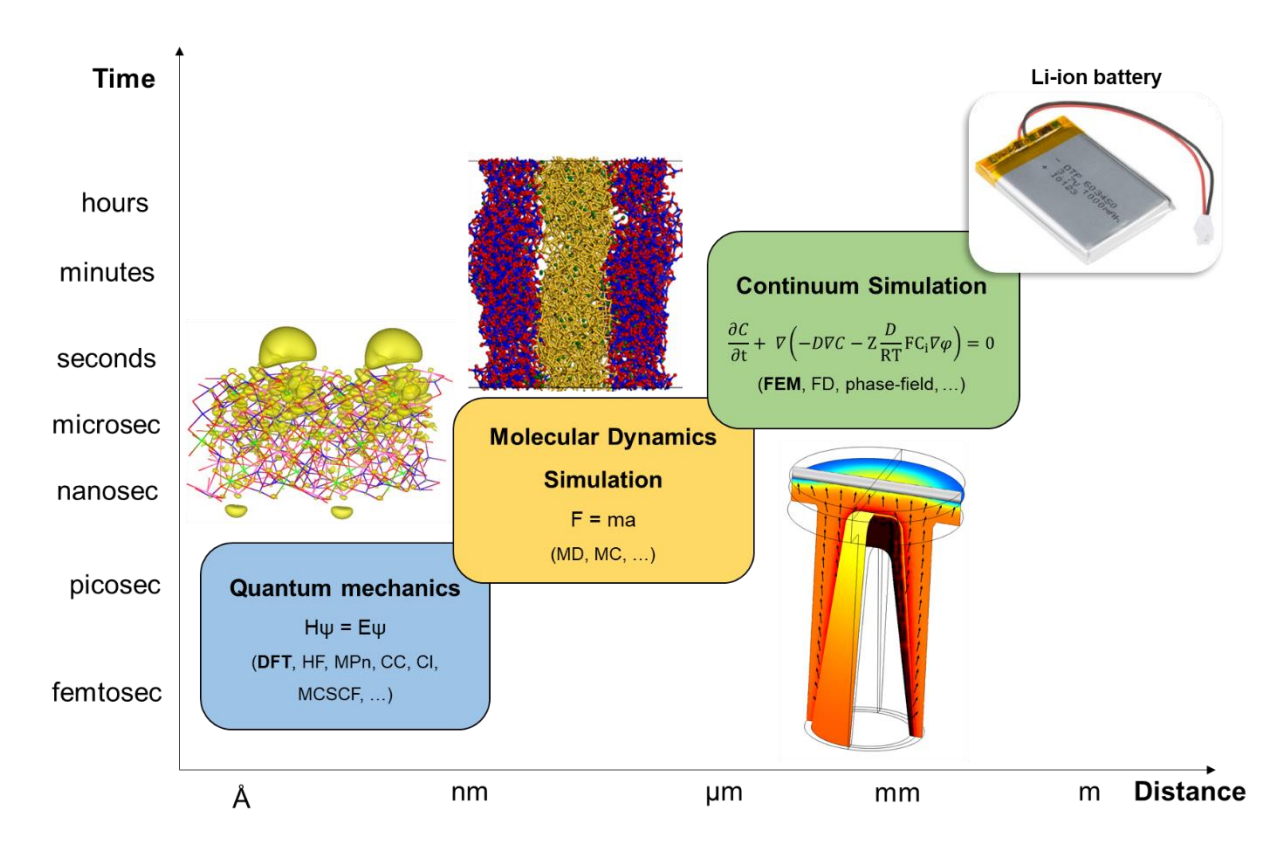


Figure 1-16. Theories and physics at different length/time scale, DFT and FEM methods are used in this thesis. The inset images are taken from literature [168, 169].

1.4.3. An integrated computational approach for interfacial challenges

For battery electrochemical and mechanical responses, continuum modeling is appropriate to incorporate battery geometry, coupled diffusion, reaction, and solid mechanics. These models rely on accurate material properties, which can be predicted from first-principle calculations. More importantly, the DFT-based models are predictive, so they can be used to discover new mechanisms that are hard to reveal experimentally. In this thesis, these methods were either performed separately or integrated to address the key questions associated with interfaces in ASSLBs.

As we discussed the Li dendrite problem in section 1.2, one of the main challenges is realizing why Li dendrite still grow in the solid electrolytes and what the critical material properties are on

preventing the Li dendrite growth. To tackle this quantum-level problem, we applied DFT calculations to explore the electronic properties of the surface and bulk structures for different solid electrolytes, including c-LLZO, β-Li₃PS₄, LATP, and Li₂PO₂N (ALD-LiPON), in CHAPTER 2. By comparing with experimental cycling results for these solid electrolytes, we are also able to filter the critical material properties that dominate the Li dendrite resistance, such as the distribution of excess electrons on the pore surfaces, the surface band gap, and the energy gap to Li-metal. Furthermore, we compared the interlayer and surface materials, like nonstoichiometric/stoichiometric tetragonal LLZO (t-LLZO) and Li₂PO₂N, and proposed that Li₂PO₂N could be a proper coating material to prevent dendrite growth. With the DFT-calculated material properties, it enables the high throughput calculations to explore new solid electrolytes that can be resistive to Li dendrite growth.

In terms of the mechanical failures in ASSLB, as explained in section 1.3, the FEM calculation is appropriate because the stress/strain in ASSLB architecture is usually at the length scale of nm to µm. First, as introduced later in CHAPTER 3, we built up a 1D continuum electrochemical model of an ASSLB with Li₃PO₄ solid electrolyte, Li anode, and LiCoO₂ cathode. This model incorporates the imperfect contact at the Li₃PO₄/LiCoO₂ interface with the discharging capacity, so it calculates how much the contact area lost during cycling. Moreover, this model couples the contact mechanics and the pressure, which could be used to predict how much pressure should be applied to recover the lost contact area and the capacity. Not only for the materials used here, but this model can also calculate for different material combinations, such as film-type and bulk-type ASSLB. In the last part, CHAPTER 4, we introduce a 3D electrochemo-mechanical model based on FEM to investigate the induced-stress/strain from the volume change of Si anode and LiCoO₂ cathode while cycling and the decomposition of LiPON solid electrolyte at interfaces. This model

simulates a 2.5D geometry that Talin and White et al. [85] synthesized. With this model, we are able to predict the stress distribution in the 3D domain and calculate the maximum stress that may occur and cause fractures. Also, the effect of experimentally observed voids in between these micro-ASSLB has been studied as well in this model. In addition, different 3D ASSLB architectures and their induced-stress distribution could be investigated as well, which leads to a better design of geometry for ASSLB in terms of preventing mechanical failures.

CHAPTER 2. Interfacial electronic properties dictate Li dendrite growth in solid electrolytes and how to prevent it by rational design of interlayer materials

This chapter is reproduced from the work published as: **Hong-Kang Tian**, Bo Xu and Yue Qi. "Computational Study of Lithium Nucleation Tendency in Li₇La₃Zr₂O₁₂ (LLZO) and Rational Design of Interlayer Materials to Prevent Lithium Dendrites." Journal of Power Sources 392, (2018): 79-86 [170] and **Hong-Kang Tian**, Zhe Liu, Yanzhou Ji, Long-Qing Chen and Yue Qi. "Interfacial Electronic Properties Dictate Li Dendrite Growth in Solid Electrolytes." Chemistry of Materials, (2019). [168]

2.1. Summary

The experimental observation of Li dendrite growth inside mechanically hard solid electrolytes (SEs) raised an important question; can hard solid electrolytes mechanically stop Li-dendrite growth? In this chapter, we report a multiscale model coupling Density Functional Theory (DFT) calculations with the phase-field method to address the question. In particular, we investigate the roles of internal defects, such as pores and crack surfaces, inside a number of solid electrolytes, including cubic Li₇La₃Zr₂O₁₂ (c-LLZO), β-Li₃PS₄, Li_{1.17}Al_{0.17}Ti_{1.83} (PO₄)₃ (LATP), and Li₂PO₂N. It is shown that LLZO surfaces have a much smaller bandgap than the corresponding bulk and thus could trap significant excess electrons, while the other three systems do not exhibit significant differences in the surface and bulk bandgaps. A fully coupled phase-field model was then developed to further examine the impact of excess surface electrons on the Li dendrite growth morphology in polycrystalline LLZO. This model successfully explained the experimentally observed dendrite intergranular growth and revealed that the trapped electrons may produce isolated Li-metal nucleation, leading to a sudden increase of Li-dendrite penetration depth. Also,

we compared the basic material properties and found that the Li ranked dendrite resistance in these SEs, based on the surface electronic properties instead of mechanical properties, is consistent with a broad range of experimental observations. Therefore, surface bandgaps and the alignment with Li-metal, as well as the excess electron distribution, can be used as key material properties to determine Li dendrite resistance of SEs. Lastly, we propose that an interlayer of Li₂PO₂N at the Li/c-LLZO interface would be efficient and defect tolerant to suppress Li dendrite formation than the tetragonal LLZO (t-LLZO) that was found at the Li/c-LLZO interface.

2.2. Introduction

All-solid-state Li-ion batteries are actively pursued as the next-generation energy storage devices due to its increased safety and energy density [32, 104, 171, 172]. However, the lithium dendrite penetration in the solid-electrolytes (SEs) and the resulted short-circuit severely limit the applicable current density [33, 49-52, 56-58, 65, 173-183]. Several mechanisms and many experimental attempts have been proposed to prevent the Li dendrite growth in SE, such as increasing the shear modulus (suggested by continuum modeling) [43, 184], increasing the relative density[61], modifying the grain boundaries[185], reducing the grain size, [65] introducing Li₃PO₄ to the internal pores to reduce the interfacial resistance[63, 64], and/or depositing Au buffer layers at electrolyte/electrode interface.[53] Nevertheless, with all the efforts so far, the Li dendrite and short-circuit are still observed at higher current density (> 1 mA cm⁻²). [58, 186] A recent study[51] proposed that the high electronic conductivity of cubic LLZO and amorphous Li₃PS₄ might be the reason for isolated Li dendrites formed in the SEs. They reported that Li₃PS₄ had a lower electronic conductivity (2.2 x 10⁻⁹ S cm⁻¹) and more cycle numbers than LLZO (5.5 x 10⁻⁸ S cm⁻¹) at 30°C. However, according to the Density Function Theory (DFT) calculations with hybrid functional

HSE06 for perfect LLZO [67] and β-Li₃PS₄ [68] crystals, the bandgaps are 5.79 eV and 3.7 eV, respectively. Thus, neither should have electronic conductivity on the order of 10⁻⁸ S cm⁻¹. Furthermore, theoretically, β-Li₃PS₄ should be more electronically conductive than LLZO. This discrepancy suggests that the observed high electronic conductivity, which further causes Li dendrite growth in the SE, may not be solely determined by their bulk electronic properties.

Internal extended defects, such as pores, cracks, grain boundaries, and triple junctions, are inevitable in ceramics-based solid electrolytes. [69-71] Extended defects can also form during battery assembly and operation. [25] One source of the defects generation is at the electrode/solid-electrolyte interface where imperfect interfacial contacts [18, 76, 187] can lead to cracks during cycling due to the chemical strain induced by lithium concentration change [188].

In our previous DFT calculations [170], we found that the stoichiometric surfaces of cubic LLZO (c-LLZO) and tetragonal LLZO (t-LLZO), representing the internal pore and crack surfaces, are more electronically conductive than their bulk due to the existence of the electronic surface state and reduced bandgap. A reduced surface bandgap can result in more intrinsic carrier (electrons/holes) concentration from thermal excitation,[189] and/or provide the state to accommodate electrons from the Li anode. It was also proposed that these surface states, existing in the internal extended defects of the SE, can trap excess electrons and drive the formation of metallic Li. [170] In addition, the nonstoichiometric c-LLZO and t-LLZO surfaces are even metallic with excess surface Li. Therefore, the observed high electronic conductivity in solid electrolytes [51] may result from the conductive internal extended defects, such as the pore surfaces and grain boundaries, instead of the bulk. This hypothesis can shed some light on why the Li dendrites seem to form in the pores and grain boundaries [52, 57, 173] and grow in isolation

[51] and randomly [190] in LLZO, however the proof of this hypothesis requires a full description of the electrochemical-mechanical [170] coupled driving forces.

The goal of this chapter is to reveal the origin of Li dendrite growth inside solid electrolytes by developing a multi-scale Li-dendrite growth model in solid electrolytes with microstructure and internal extended defects. First, DFT calculations were used to evaluate the effect of surface electronic properties. Four promising SEs, cubic-Li₇La₃Zr₂O₁₂(c-LLZO), β-Li₃PS₄, Li_{1.17}Al_{0.17}Ti_{1.83}(PO₄)₃ (LATP), and Li₂PO₂N were compared. Also, two interlayer materials will be evaluated. One directly observed interlayer material is the tetragonal LLZO (t-LLZO) formed at the Li-metal/c-LLZO interface, based on the research of Ma et al.[191] Therefore, both c-LLZO and t-LLZO, representing the bulk and interlayer region, respectively, will be included in this study. Lithium phosphorous oxynitride (LiPON) has been successfully coated by the Atomic Layer Deposition (ALD) [192, 193] method on Li-metal electrodes as a protection layer [194] that gives a better physical contact with electrodes.[187] The structure of ALD-LiPON has been characterized to be similar to the crystalline Li₂PO₂N, [195] which consists of parallel anionic chains formed of corner-sharing (PO₂N₂) tetrahedral.[196] Therefore, to evaluate whether the ALD-LiPON coating at the c-LLZO/Li interface can efficiently suppress Li dendrite formation, Li₂PO₂N is compared with c-LLZO and t-LLZO for their Li-metal nucleation tendency on surfaces. The total and local density of states (TDOS and LDOS) and the distribution of excess electrons on the surfaces were investigated and showed a large variation in different SE materials. To demonstrate the electronic impacts on the Li dendrite morphological evolution, we further developed a general phase field model of Li plating in a polycrystalline SE environment incorporating the Butler-Volmer kinetics [197-199], solid mechanics [200], and explicit lithium nucleation process [201]. The DFT calculated concentration of excess electrons on one of the

surfaces served as an input to the phase field simulations. Although the force field based simulations have predicted fracture and Li-ion diffusion at the grain boundaries (GB) in LLZO [169], the electronic structures of GB of LLZO are still beyond normal DFT calculations. Thus, in the phase field model, the GBs adopt the electronic properties of the surfaces at the moment. The influence of the grain size of the polycrystalline SE and the excess electron density in the internal surfaces on the lithium dendrite penetration depth will be discussed. The model captured several observed lithium dendrite growth trends in all-solid-state batteries, i.e., Li dendrite intergranular growth, the isolated Li-metal formation within pores and grain boundaries, and a sudden increase of Li-dendrite penetration depth. [51-53, 173, 202] Finally, we compared the basic materials properties of these SE materials, including the shear modulus, the reduction voltage, the bulk bandgap, the surface bandgap, energy gap to Li-metal, and the location of the excess electrons, in order to identify the key material properties that impact Li dendrite growth inside of the solid electrolytes. Using the surface electronic property as the criteria, the ranked Li dendrite growth resistance in these SE materials is consistent with a broad range of experimental observations, including the measured electron conductivity and the Li dendrite growth rate.[51] Thus, these DFT-computable properties can be used to screen solid electrolyte materials with high Li dendrite resistance via high throughput calculations.

2.3. Computational methods

2.3.1. Atomic bulk and surface structures of solid electrolytes

All the electronic structure calculations were performed via the Vienna Ab initio Simulation Package (VASP) [203] based on plane-wave DFT. Core-valence electron interaction was treated using projector augmented wave (PAW) [204], and two different levels of theory were employed: the semi-local generalized gradient approximation [205] of Perdew, Burke, and Emzerhof (PBE)

[206] and the hybrid functional of Heyd, Scuseria, and Ernzerhof (HSE06) [207, 208]. The convergence criteria for the electronic is the energy difference of 10⁻⁵ eV. Atomic positions were relaxed until all forces were less than 0.03 eV/Å. For geometry optimization, Gaussian smearing with an energy of 0.1 eV was used for the electronic occupancies. Cutoff energy of 600 eV for geometry optimization is enough to have the total energy converged at 1 meV/atom for c-LLZO, LATP, and Li₂PON₂, and smaller cutoff energy of 500 eV is sufficient for β-Li₃PS₄. Monkhorst-Pack scheme [209] of a 3x3x3 k-points grid was used for the bulk structure of c-LLZO, Li₂PO₂N, and β-Li₃PS₄, and 3x3x1 for LATP. For the relaxation of surface structures, a k-points grid of 3x3x1 is enough for all four materials. To have more precise results for the calculations of the density of states (DOS) and the charge distribution, Tetrahedron method with Blöchl corrections were used for the electronic occupancies and larger k-mesh of 11x11x1 for the calculation of DOS and charge density distribution.

The detailed process of selecting and building the surface structures, determining surface termination and Li atoms distribution, and calculating the surface energies can be found in APPENDIX. Here we briefly describe the representing surface structures with the lowest surface energy.

c-LLZO, Un-doped cubic Li₇La₃Zr₂O₁₂ was selected to represent c-LLZO with a space group of Ia3d. The most energetic-favorable surface structure is along (110) direction and terminated symmetrically by La-Li atoms with a stoichiometric ratio, giving the surface energy of 0.85 J m⁻². A nonstoichiometric (110) surface with excess Li atoms was also found to have a comparably low surface energy of 0.88 J m⁻², and the details of this surface can be found in our previous calculations [170].

β-Li₃PS₄, A bulk β-Li₃PS₄ with a space group of Pnma was chosen, and Li atoms were distributed 70% and 30% at 4b and 4c site (Wyckoff notation), respectively. The most energetic-favorable surface structures with a surface energy of 0.19 J m⁻² is along (100) direction with a stoichiometric ratio and terminated symmetrically by S atoms, which also preserved the PS₄ polyhedral. All non-stoichiometric surfaces have much higher surface energy compare to the stoichiometric one.

LATP, The composition of Li_{1.17}Al_{0.17}Ti_{1.83}(PO₄)₃ with a space group of R $\overline{3}$ c was chosen to represent LATP. The most energetic-favorable surface structure was found to be along (012) direction with a stoichiometric structure and terminated by Li atoms and Al atoms distributed symmetrically. This structure gave the lowest surface energy of 0.37 J m⁻², compared to other stoichiometric and nonstoichiometric surfaces.

LiPON, The composition of Li₂PO₂N with a space group of Cmc2₁ was chosen to represent LiPON as the atomic layer deposition. [210] LiPON has been characterized as Li₂PO₂N [195]. The most energetic-favorable surface structure was along (100) direction with a stoichiometric ratio and symmetrical termination of Li atoms, which preserved the P(NO)₂ polyhedral and gave the lowest surface energy of 0.46 J m⁻².

t-Li₇La₃Zr₂O₁₂, The t-LLZO structure is taken from ICSD database[211] (No. 246816), and the occupancy of Li atoms is 1. Symmetric non-stoichiometric slab structures of t-LLZO with different terminated atoms were constructed along (100) and (110) directions by the same procedure as the non-stoichiometric slab of c-LLZO, as Figure S1 of the supporting information shows. Note, for t-LLZO, only the non-stoichiometric slab could be built to maintain the symmetric termination on both ends. The surface energies were calculated to determine the most stable structure.

2.4. Results and discussions

2.4.1. The distribution of the excess electrons in the internal surfaces of solid electrolytes

The total density of states (TDOS) of stoichiometric surface structures is plotted in Figure 2-1 along with the position of conduction band minimum (CBM) of its bulk structure (cyan dashed line), which shows how much the bandgap decreases from bulk to surface. The filled states stand for valance bands and the unfilled states are conduction bands. All the energy levels have been shifted with respect to the vacuum level based on computed work functions (in Figure 2-12 in APPENDIX). The Fermi level of Li metal is marked as the vertical black solid line, which is from the work function of 3 eV for Li [41]. E_{g,surface} stands for the bandgap of surface and T_g represents the energy gap between the Li metal Fermi level to the CBM of the solid electrolyte. Considering GGA calculation may not be accurate enough to capture the electronic properties and band structures, we also performed calculations with hybrid functional (HSE06) for comparison, as listed in Table 2-1 and the TDOS is plotted in Figure 2-13 in APPENDIX. The calculated band gap of bulk and surface from GGA is generally lower than that of HSE06 calculation, but the trend between different solid electrolytes is the same. Also, the charge distribution is similar in these two calculations. Therefore, to be consistent with the surface energy calculations, GGA results are shown in the main text while the HSE06 results can be found in APPENDIX.

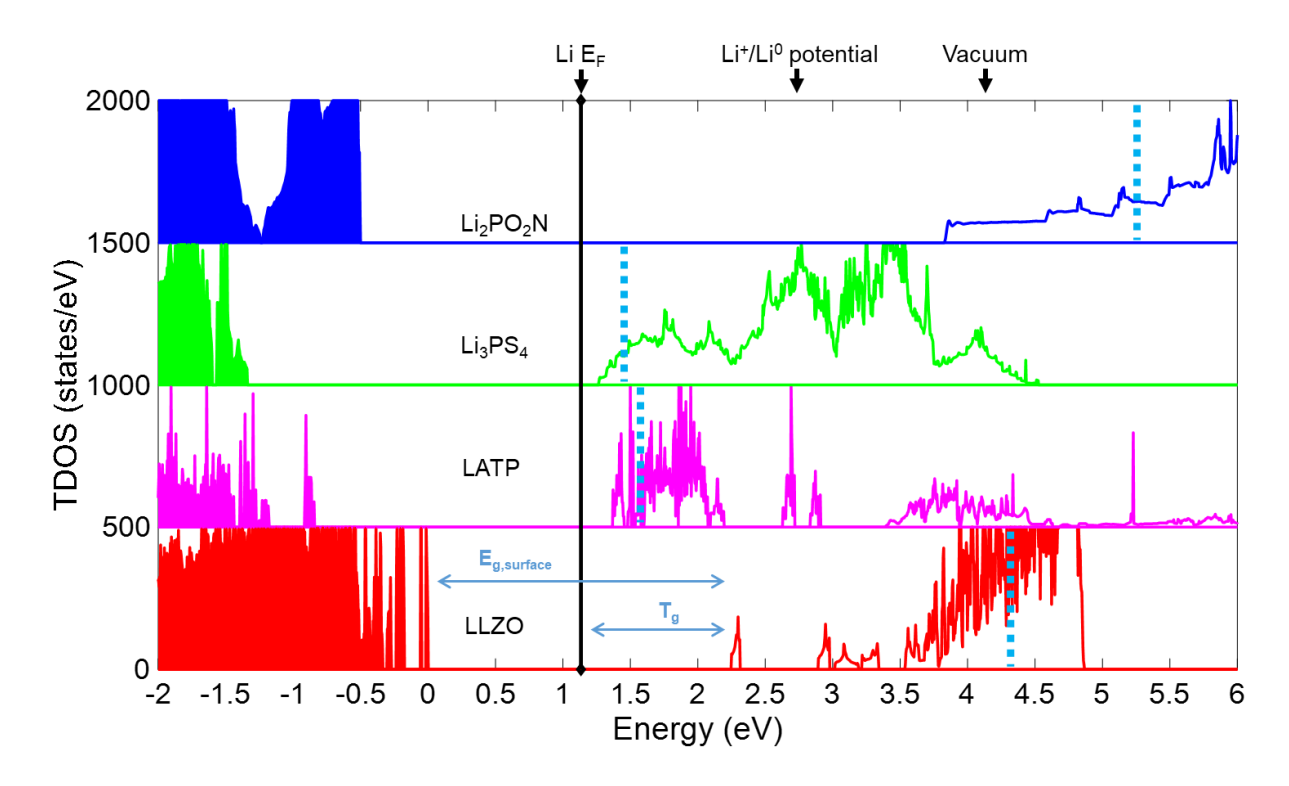


Figure 2-1. The calculated total density of states (TDOS) for the four SE surface structures aligned with the vacuum level. The position of CBM of the corresponding bulk structure is labeled as the cyan dot lines. The position of the vacuum level, and the Fermi level of Li metal (Li E_F), and the potential corresponding to the Li $^+$ /Li 0 deposition is labeled. $E_{g,surface}$ stands for the surface bandgap, and T_g is the energy difference from Li-metal in vacuum to the CBM of the SE.

It has been reported in our previous study [170] that the Li₂PO₂N surface still has a large bandgap of around 4.35 eV, while c-LLZO surface shows a considerable drop in bandgap from 4.30 eV of bulk to 2.20 eV of the surface due to the existence of surface states, as the E_{g,surface} in Figure 1. On the other hand, there is no apparent change of bandgap on the β-Li₃PS₄ and LATP surface, and both have a small decrease of around 0.2 eV in bandgap from bulk to surface structure. As a previous study [212] stated that a material with a bandgap smaller than 2.2 eV is considered as a narrow bandgap semiconductor, and based on that practical definition the β-Li₃PS₄ surface (2.67 eV) would be more like a wide bandgap semiconductor. As the intrinsic carrier (electrons/holes) concentration and electronic conductivity increases with decreased surface bandgap, the TDOS results suggest that the surfaces of c-LLZO, LATP, and Li₂PO₂N are more conductive than their

bulk structure that is electronically insulating, but Li₂PO₂N surface could still be insulating due to its large bandgap.

The reduced surface band gap can also push the conduction bands below the Li plating potential, so electrons can transfer from Li-metal to the solid electrolyte. Assuming the Li-plating (Li⁺/Li⁰) potential in the solid electrolyte is still -3.04 eV with respect to Standard Hydrogen potential (SHE), applying the Trasatti relation [213, 214], the Li⁺/Li⁰ plating voltage is 1.77 eV above the Li Fermi level in vacuum or 1.39 eV below the vacuum level, as labeled in Figure 2-1. Therefore, both the bulk and surface CBM are below the Li-plating voltage for β -Li₃PS₄ and LATP, allowing electron transfer. Although the CBM for bulk c-LLZO is above the Li⁺/Li⁰ potential, the surface state is not. Therefore the surface state in c-LLZO is critical for the electron transfer from Li to LLZO.

The following question needs to be addressed is if the electrons can transfer to the solid electrolyte containing defects, such as surfaces, where the excess electrons will be located. Figure 2-2 mimics the situation of when excess electrons arrive on the surfaces by calculating the charge density difference before and after inserting the electrons at a density of $0.0046/\text{Å}^2$ for all the solid electrolyte slab models. The distribution of the excess electrons is plotted as the yellow region at the selected isosurface that ensures the plotted charge density is the same across different materials. It can be seen that the additional electrons are localized mostly on the c-LLZO surface. However, for Li₂PO₂N, β -Li₃PS₄, and LATP, those additional electrons seem to stay underneath the surface mainly. This observation generally agrees with the overall electron affinity indicated by the energy difference between CBM and vacuum level.[215, 216] As shown in Figure 2-1 for LLZO, the bulk CBM is higher than the vacuum level, indicating a negative electron affinity; while the surface state is below the vacuum level with a positive electron affinity. As we mentioned before,

experiments showed the Li dendrites in c-LLZO and β-Li₃PS₄ seem to grow in the pores and crack surfaces and grain boundaries. This analysis of the excess electron distribution could be used to evaluate how likely the additional electrons localize on the surface, which would make reducing Li-ions to Li-metal possible. Based on this results, it is suggested that the c-LLZO surface would be more likely to have Li-ions reduced on the surface than other three solid electrolytes, because of the tendency that additional electrons localized on the c-LLZO surface. Also, based on the discussion we had in the previous study [170].

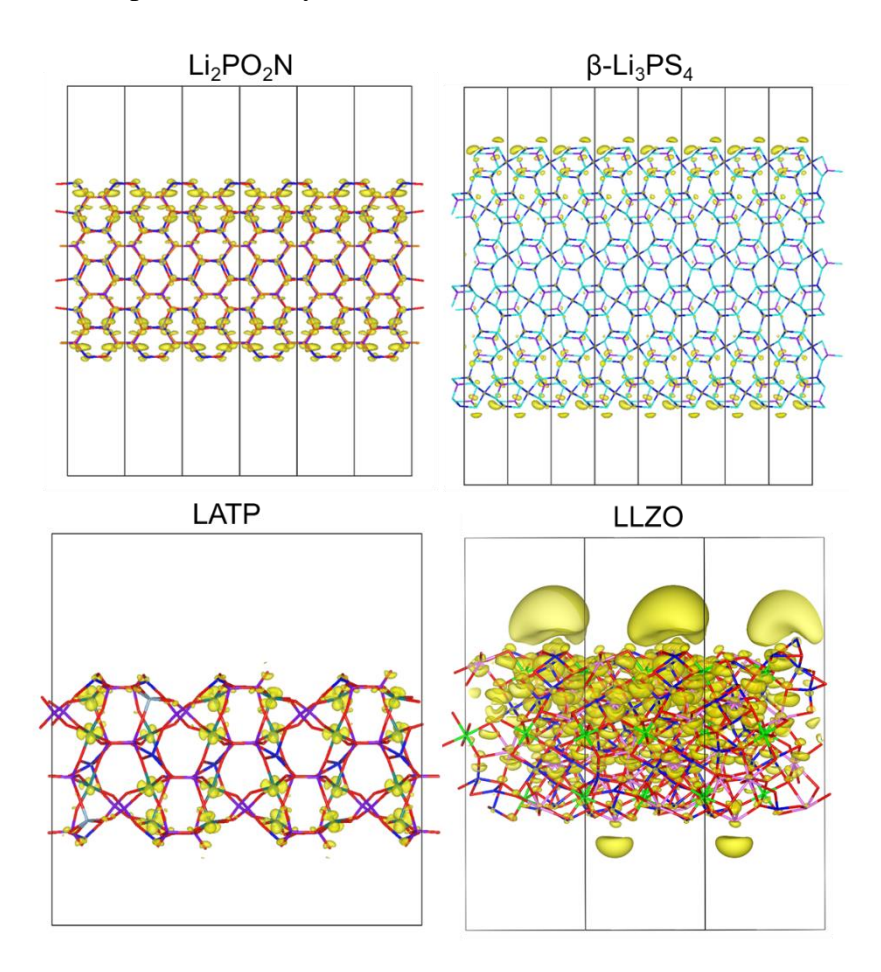


Figure 2-2. The distribution of additional electrons (yellow region), which is calculated from the difference in charge density before and after inserting additional electrons.

To further investigate which element takes most of the additional electrons and how much of electrons trapped by the surface atoms, we plotted the local density of states (LDOS) in Figure 2-3,

which shows only the density of states near the CBM because that is where the additional electrons would occupy. The solid lines represent the projected density of states from the total atoms of each element, while the dashed lines stand for the contribution from only the atoms on the surface, or the first layer underneath the surface. As Figure 2-3 shown, the CBM of the c-LLZO surface is mainly composed of La atoms and followed by O atoms. One thing to be noticed is the La contribution to the c-LLZO CBM is mainly from the surface La atoms, which is shown as the red dashed line in Figure 2-3. On the other hand, the main contribution to the CBM of β-Li₃PS₄, Li₂PO₂N, and LATP is S and P, O, and Ti, respectively, not only from the surface atoms but from all the atoms in the slab structure. The LDOS results in Figure 2-3 indicate that if there are excess electrons in the c-LLZO surface, they would be trapped firstly by the La atoms above the surface. However, for the other three materials, the additional electrons would be distributed throughout the bulk instead of localizing on the surface.

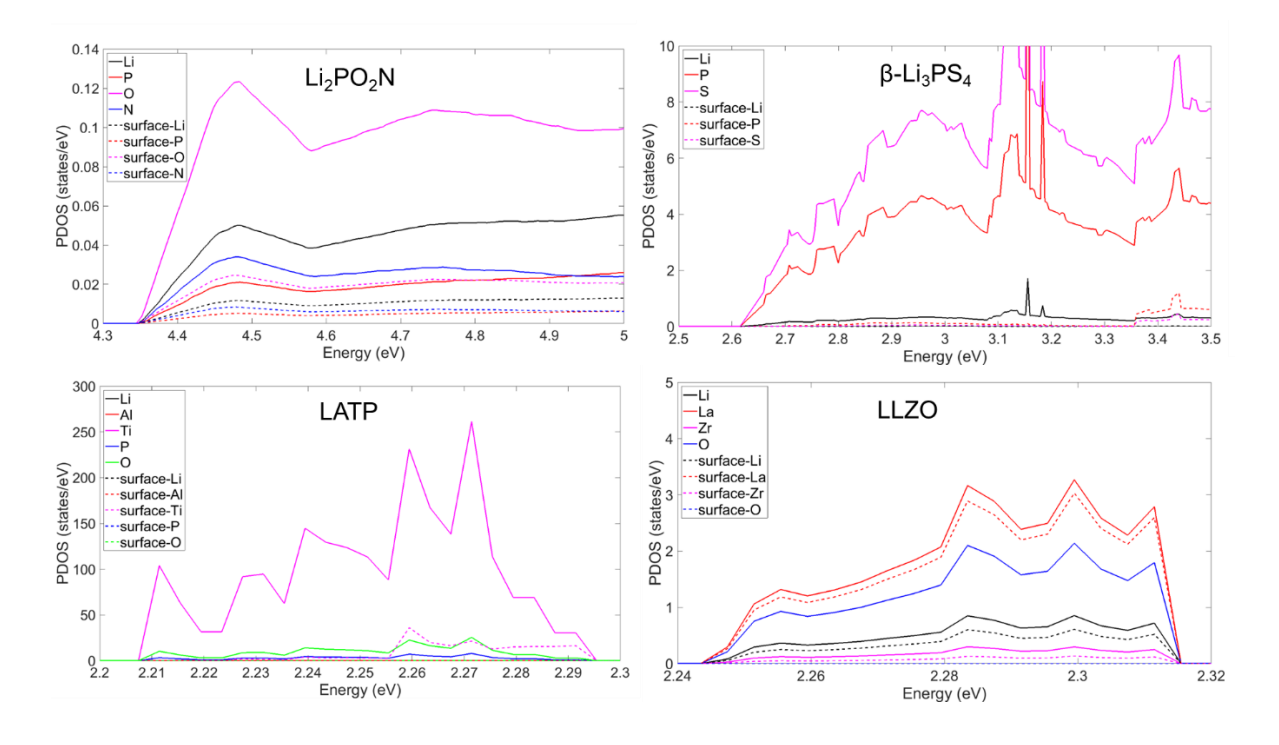


Figure 2-3. Calculated partial density of states for different surface structures, only the states around the CBM are shown.

2.4.2. The thermodynamic driving force to reduce Li⁺ on the surface of c-LLZO

From the above results, it is suggested that the La atoms on the surface of c-LLZO can trap some extra electrons, which could be released from the electrodes. It is necessary to determine whether these localized electrons will reduce La³⁺ or Li⁺. Zr⁴⁺ ions are unlikely to be reduced, as they are not exposed on the surface, although its reduction voltage is above Li-metal. [25, 217] It could be evaluated by comparing the thermodynamic driving force for the two competing products, Li₂O and La₂O₃, which are both the thermodynamically stable phases predicted by Zhu et al. via DFT calculations. [25] From the thermodynamics handbook by Robie and Hemingway [218], the Gibbs free energy at 298 K for Li₂O and La₂O₃ is -1123.97 and -1137.31 kJ/mol per oxygen consumed at room temperature, respectively. Therefore, when excess electrons come, it is more likely to reduce Li⁺ instead of La³⁺ as La₂O₃ has a lower formation energy than Li₂O. In fact, La is among very few metals, such as Mg and Ca, which can reduce the Li⁺-ion from Li₂O.[217, 219] Considering the distribution of the excess electrons are more delocalized on the non-stoichiometric surface of c-LLZO and t-LLZO than that of stoichiometric c-LLZO, they could react with Li-ions and reduce it to Li metal more easily. Since the stoichiometric and non-stoichiometric c-LLZO have similar surface energies, both are likely to exist in LLZO. Therefore, the external electrons in c-LLZO could be either localized or dispersed on the surface. In this case, the Li ions could be reduced on the surface of c-LLZO.

2.4.3. The impact of surface electrons on Li dendrite growth

To go beyond the simulation size limit of DFT and demonstrate the impacts of the as-calculated surface electronic states to the Li-dendrite growth in polycrystalline SEs, we further investigated the Li electrodeposition in polycrystalline SEs by the phase-field method using the surface excess electron concentrations estimated from DFT results. The phase-filed model was conducted by Zhe

Liu, Yanzhou Ji, and Long-Qing Chen at The Pennsylvania State University, and the computation detail of the phase-field model can be found in publication. [220] Here we treated the internal pore surfaces and grain boundaries with the same electronic properties. More detailed band structure calculations of grain boundaries need to be performed in the future. Since electrons respond almost instantly to the electrostatic potential compared with Li ion transport kinetics in solid electrolytes, we calculated the static surface electron concentration in each material based the DFT DOS results, as detailed in APPENDIX.

The Li electrodeposition processes in SEs of grain sizes ranging from 75 to $500\mu m$ were simulated in identical $500 \mu m \times 500 \mu m$ 2D half-cells with a constant electric overpotential of 0.1V. The properties of bulk c-LLZO (i.e. elastic moduli, Li ion conductivity, surface energy, etc.) were used for all SEs in this study (detailed in literature [168]). To directly demonstrate the influence of excess surface electrons on electrodeposition, we compared two idealized scenarios of surface electronic states: "real" LLZO polycrystalline SEs referring to the extended internal defects with excess surface electron concentration ($c_e = 0.337 \, mol/L$) and "ideal" LLZO SEs referring to the extended internal defects with no surface electrons, while both have identical structures. The spatial and temporal evolution of the multiphase morphology, Li ion concentration, and electric potential during electrodeposition were tracked over the simulation time of 800s. In both cases, the Li dendrite growth is driven electrochemically by the applied overpotential. The location of dendrite penetration is governed by SE local mechanical strength, which is weaker at GBs and extended defects. Based on the phase morphology, the far most position of Li-metal phase toward the Li-anode surface is defined as the Li-dendrite penetration depth.

The final morphologies of 800s electrodeposition show larger amount of metallic Li and deeper dendrite penetration depth in real LLZO (Figure 2-4 a1-d1) than the ideal LLZO (Figure 2-4 e1-

h1) for all SE grain sizes. This difference is due to the additional electrochemical driving force from excess surface electrons in real LLZO. The contrast between the real and ideal cases becomes more prominent when isolated nucleation of metallic Li took place in the real SEs with the grain sizes of 75 μ m and 150 μ m (Figure 2-4 g1 and h1, respectively.). This is because the additional electrodeposition sites provided by the isolated nucleation inside SE significantly increase the intergranular dendrite penetration depth and growth rate. A more clear comparison is quantitatively demonstrated by the dynamic evolution curves of the total amount of Li (corresponding to capacity loss) and the dendrite penetration depth in SEs, where the two abrupt rising steps in the penetration depth (Figure 2-4 i) and the sudden deviations in the Li dendrite amount increasing rates (Figure 2-4 j) highlighted by red arrows, indicate the initiation of isolated nucleation (Figure 2-4 k1). On the other hand, the formation of metallic Li at the isolated nucleation sites will slow down or even block the intergranular Li ion transport and cause an abrupt drop in the local electric potential (Figure 2-4 k2), which impedes the normal electrodeposition at the anode substrate.

Without the trapped electrons at the GBs, the Li growth is continuous (Figure 2-4 a-d). With the electrons on GB, the dendrite growth can be discontinuous. By comparing the morphologies of real LLZO SEs of different grain sizes ranging from 75 to 500 μ m (Figure 2-4 e1-h1), we observed an increasing trend in the total amount of metallic Li in SE (Figure 2-4 j), and potentially a higher probability of isolated nucleation. This is because the SE of finer grain size or lower mass density contains higher volumetric percentages of internal extended defect surface, e.g. from pores, cracks and grain boundaries. Therefore, they create more space and driving force for intergranular growth and more sites for isolated nucleation, leading to the observed trends.

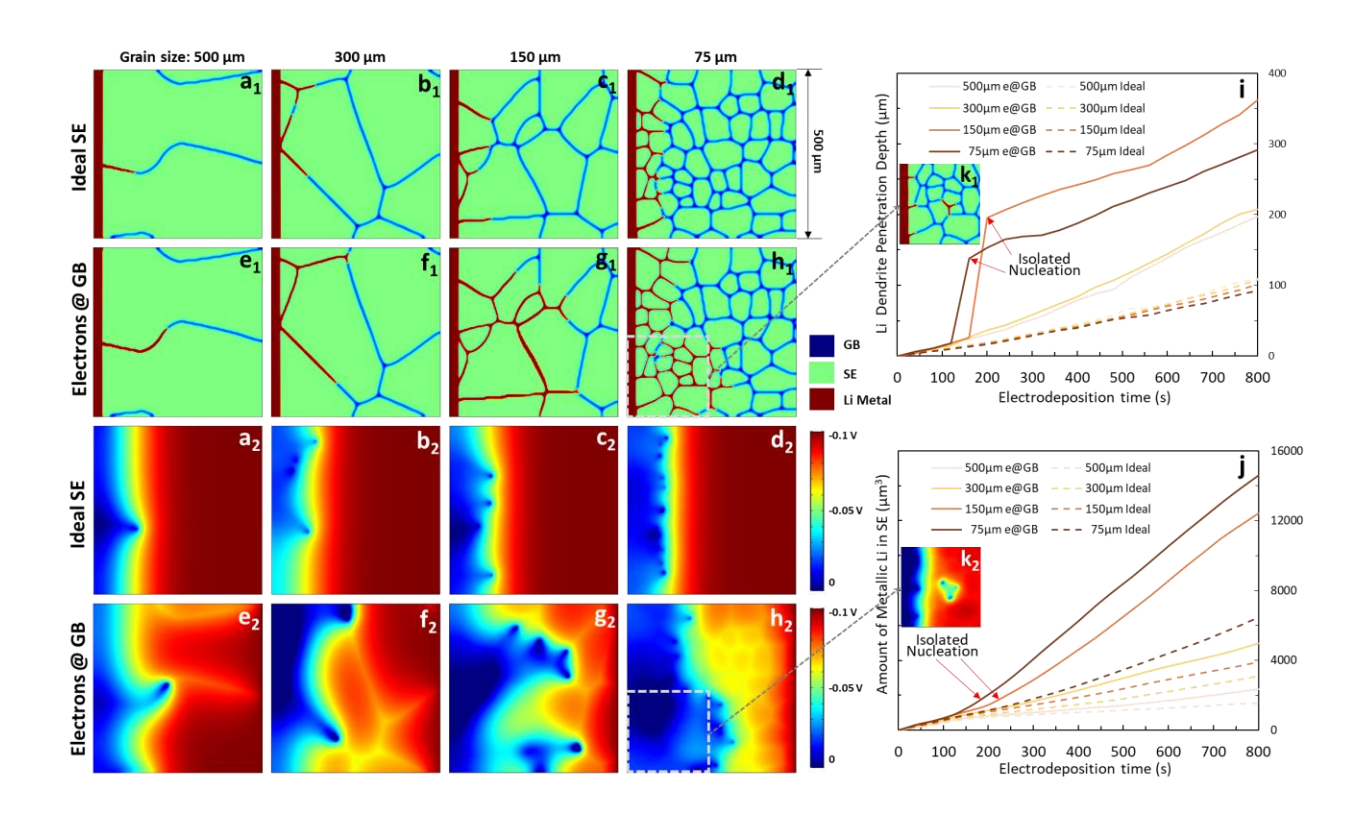


Figure 2-4. Phase-field simulation results on the impacts of surface trapped electrons and grain size on the morphologies and electric potential distributions after 800s Li electrodeposition in a $500 \times 500 \ \mu m^2$ half-cell. A comparison of the final phase morphologies in (a1-d1) the ideal SEs with excess electron-free surfaces and (e1-h1) the real SEs with the calculated surface electron concentrations from DFT, in a series of grain sizes. And a comparison of their corresponding final electric overpotential distributions for the SEs in (a1-h1). The dynamic evolution of (i) the Li dendrite penetration depths and (j) the total amount of metallic Li in SEs of different grain sizes. The initiation of isolated dendrite nucleation is demonstrated by (k1) the phase morphology and (k2) the corresponding electric potential distribution in the SE of the 75 μm grain size at 200s.

The model captured several major reported trends of lithium dendrite growth in all-solid-state batteries, i.e. Li dendrite intergranular growth, the isolated Li-metal formation within pores and grain boundaries, and the sudden increase of Li-dendrite penetration depth. These simulated electrodeposition behaviors can further lead to the observation of the abrupt rise in charging current (under constant voltage condition) and effective electronic conductivity of SEs, and will eventually cause accelerated capacity loss during cycling and a higher risk of short-circuiting. [221]

2.4.4. The critical material properties that dominate the Li dendrite growth

It is important to identify the key material property for the Li dendrite growth resistance in solid electrolytes by correlating the computed material properties and experimental dendrite formation trends. Table 2-1 listed the calculated/collected the mechanical, thermodynamic, and electronic properties for the four SE materials for comparison. The shear modulus was obtained from literature and can also be computed directly from DFT as well. [222, 223] The fracture energy is twice of the DFT calculated surface energy of the most stable surface structure (Table 2-1), and it indicates how likely the Li dendrite will cleave the crystal structure and form new cracks. One to notice is the dramatic difference in fracture energy between c-LLZO (1.72 J/m²) and β-Li₃PS₄ (0.38 J/m²), which implies that β-Li₃PS₄ is more likely to have crack propagation and fractures than c-LLZO. The microstructure of Li dendrites in β-Li₃PS₄ and c-LLZO from the transmission optical microscopy images [52, 53] reflected this phenomenon. It was shown that the metallic Li grows and penetrate β-Li₃PS₄ with a very spiky morphology, which may result from the continuous crack opening of β-Li₃PS₄. On the other hand, the metallic Li in c-LLZO is more likely to go through the existing grain boundaries and pores without breaking the grains, as it was also confirmed by experiments and DFT calculation that c-LLZO exhibits sufficient stiffness with isotropic shear modulus within the range of 56-61 GPa and large fracture energy. The reduction potential was based on the DFT-calculated phase equilibrium vs. Li potential, which shows the electrochemical stability against Li metal (anode). [25] The bulk bandgap and surface bandgap and the location of excess electrons are calculated in this work.

Table 2-2 listed a collection of experiments of the cycling tests for Li|SE|Li symmetric cells performed at room temperature under different current densities. The experiments showed the critical current density (CCD), which is the maximum current density without short-circuiting.

Given the fact that short-circuiting is caused by the Li dendrites penetrated the solid electrolyte, the higher the CCD is, the more resistive to the Li dendrite growth the solid electrolyte is.

Table 2-1. Comparison of the intrinsic material properties of different solid electrolytes.

	Shear Modulus (GPa)	Fracture Energy (J/m²)	Reduction Potential vs. Li (V) [25]	GGA-PBE			HSE			Location of
				E _{g,bulk} (eV)	$\begin{array}{c} E_{g,surface} \\ (eV) \end{array}$	T _g (eV)	E _{g,bulk} (eV)	$\begin{array}{c} E_{g,surface} \\ (eV) \end{array}$	$\begin{array}{c} T_g \\ (eV) \end{array}$	excess electrons
Li ₂ PO ₂ N	30 [45]	0.92	0.87	5.98	4.35	2.69	6.92	5.61	2.88	Bulk - O
β -Li ₃ PS ₄	6 [44]	0.38	1.71	2.82	2.67	0.13	3.49	3.38	0.25	Bulk - S,P
LATP	56 [46]	0.88	2.16	2.42	2.24	0.47	3.31	3.05	0.07	Bulk - Ti
c-LLZO	59 [47]	1.72	0.05	4.30	2.20	1.11	5.46	2.19	1.23	Surface - La

Table 2-2. Comparison of the cycling results of a symmetrical cell from literature.

	Current density (mA/cm ²)	Areal capacity (mAh/cm ²)	Short-circuit?	Cycle number	Temperature (°C)	Reference
c-LLZO (Al-substituted)	0.046	0.092	No	20	RT	[65]
c-LLZO (Al- substituted)	0.049	0.098	No	5	RT	[224]
c-LLZO (Ta-substituted)	0.05	-	Yes	-	25	[51]
c-LLZO (Ta-substituted)	0.1	0.41	Yes	10	25	[58]
c-LLZO (Ta-substituted)	0.3	0.15	Yes	5	RT	[180]
β-Li ₃ PS ₄	0.1	0.2	No	20	25	[205]
β -Li ₃ PS ₄	0.3	-	No	500	RT	[225]
β -Li ₃ PS ₄	0.38	1.5	Yes	4	RT	[33]
β -Li ₃ PS ₄	0.75	-	No	24	RT	[186]
LATP	0.1	0.1	No	19	RT	[226]
Glass-LATP	0.1	0.1	No	5	RT	[227]
LATP	0.01	0.01	No	300	RT	[228]
LiPON	0.3	-	No	-	25	[51]

Comparing c-LLZO and β -Li₃PS₄, c-LLZO appears to be a stiffer (highest shear modulus), more electrochemically stable against Li (lowest reduction potential), and difficult to fracture (highest

fracture energy) solid electrolyte. If the mechanical and electrochemical stabilities are more important, c-LLZO would have been more resistant to Li dendrites growth than β-Li₃PS₄. However, the experiments reported the opposite trend. The CCD is around $0.05 - 0.1 \text{ mA/cm}^2$ for c-LLZO and 0.75 mA/cm2 for β-Li₃PS₄, as shown in Table 2-2. Meanwhile, The recent study [51] reported that the electronic conductivity of c-LLZO and Li₃PS₄ at 30 °C is 5.5 x 10⁻⁸ S cm⁻¹ and 2.2 x 10⁻⁹ S cm⁻¹ at 30 °C, respectively, and there were more dendrites shown in c-LLZO. The bandgap for c-LLZO is higher than β-Li₃PS₄, which does not follow the same trend of experimental electronic conductivity values. The surface electronic properties are more important here. The bandgap for the surface of c-LLZO is lower than that in β-Li₃PS₄, suggesting more electron carriers in the conduction bands. In the aligned surface TDOS, it is more favorable for electrons to transfer to the slab of β-Li₃PS₄ than c-LLZO from the Li anode, as the CBM in β-Li₃PS₄ is closer to Li-metal Fermi level. However, these excess electrons will still not localize on the surface, so the isolated dendrite nucleation is less likely to occur on the crack and pore surface inside the β-Li₃PS₄, which is similar to the continuous Li dendrite growth scenario shown in Figure 2-4 a1-d1. In contrast, the internal surfaces (pore or cracks) in c-LLZO tend to trap excess electrons, which facilitate faster Li dendrite growth due to isolated Li nucleation, similar to the scenario shown in Figure 2-4 e1h1. This suggests that the surface electronic properties in solid electrolytes, such as the surface bandgap, the relative position with respect to the Li-metal Fermi level, and the distribution of excess electrons, are the dominating factors for Li-dendrite growth in solid electrolytes, instead of the shear modulus, fracture energy, the reduction potential, and the bandgap in the bulk of the SE. Based on these DFT-calculated surface properties, we ranked the four SE materials by their resistance to Li dendrites as the following, $\text{Li}_2\text{PO}_2\text{N} > \beta\text{-Li}_3\text{PS}_4 \approx \text{LATP} > \text{c-LLZO}$. This ranking was determined based on the calculated results that c-LLZO has the lowest surface bandgap and

the largest tendency to trap electrons on the surface; Li_2PO_2N has the largest surface bandgap, and the additional electrons tend to move under the surface; both β - Li_3PS_4 and LATP would trap the additional electrons under the surface and their CBM level is similar with respect to the Li-metal Fermi Level.

From the reported cycling results and CCD, as shown in Table 2-2, the observed resistance of solid electrolytes to the Li dendrites could be ranked as: LiPON (Li₂PO₂N) \approx LATP $> \beta$ -Li₃PS₄ > c-LLZO. Note there is no reported short-circuit in the symmetric cell of LATP and LiPON, no matter the LiPON structure is amorphous or crystalline. Instead, both LiPON and LATP show a large overpotential of around 4 V when the current passed through [51, 226]. This order is generally consistent with our prediction, except for LATP, which seems to be very resistive to the Li dendrite growth. A possible reason is the formation of electronically insulating solid electrolyte interphase (SEI) from the decomposition of LATP. A DFT study [25] that calculated the stability window of different solid electrolytes and LATP exhibits the highest reduction potential, among the solid electrolytes in this study, as in Table 2-1. This means LATP it is likely to decompose at the Li/LATP interface and c-LLZO would be electrochemically more stable because of its relatively low reduction potential. From a recent experimental study [226], which also found more Li dendrites penetrate c-LLZO than LATP, the large overpotential observed in LATP was attributed to the formation of electronically insulating SEI. Such insulating SEI would further block the electron pathway and stop the dendrite growth. This could explain why there was no short-circuit happening to LATP and why it did not follow our prediction since the SEI effect has not been included in this study yet, but it will be the next step that is worth to focus. Even both β-Li₃PS₄ and LATP are not stable against Li metal and would form SEI based on their high reduction potential, short-circuit only happens in β-Li₃PS₄ but not in LATP. Therefore, whether the SEI

forms may not be the critical factor, it is the electronic conductivity of SEI that would affect the resistance to Li dendrite.

Based on the DFT-computable electronic properties of surfaces, high throughput calculations are possible. The design direction for the future solid electrolyte materials that resist Li dendrite growth inside should follow the following material properties: A large surface bandgap, the surface CBM state above the Li plating potential, being able to localize the additional electrons underneath the surface, and having an electronically insulating SEI or no SEI. In addition to discovering new materials, doping different elements to change the distribution of additional electrons or modifying the interface to alter the surface structure might be also beneficial to the prevention of Li dendrites.

2.4.5. Interlayer material to prevent metallic Li grow into the c-LLZO

To further propose interlayer materials that are resistive to Li dendrite growth, we investigated the surface electronic properties of t-LLZO as well and compared with Li₂PO₂N, which has been synthesized at the interface by ALD process [192, 193]. Several different terminated slabs of t-LLZO were built, and the surface energies were compared in Table 2-5 in APPENDIX. The La-Li co-termination and Li termination (only Li atoms on the surface) have the lowest energies for the (110) and (001) surface, respectively. The surface energy of (110) surface is slightly lower than (001) surface. Therefore, the (110) La-Li terminated non-stoichiometric slab of t-LLZO with the lowest surface energy (Li₆₄La₂₈Zr₁₆O₉₆) was picked for the further analysis of electronic properties. The difference of the electronic properties between bulk and slab structures is compared by calculating the TDOS, as shown in Figure 2-5. The TDOS of t-LLZO-bulk structure (not shown) is almost identical to that of c-LLZO-bulk. Figure 2-5 (b) shows that the non-stoichiometric slab of c-LLZO has an occupied gap state, which is at the similar energy level as the stoichiometric c-LLZO slab. Figure 2 (c) shows that the non-stoichiometric slab of t-LLZO also has some additional

states in the bandgap being occupied. Also, the Fermi level of both the non-stoichiometric slabs of c-LLZO and t-LLZO have moved into the conduction band due to the excess Li and La atoms (ions and electrons) in the structures. In contrast, the calculated bandgap of bulk Li₂PO₂N in Figure 2-1, which is around 6 eV, is similar to the measured bandgap of LiPON.[18] However, there are no additional states shown in the bandgap of slab structure of Li₂PO₂N, only the conduction band energy is shifted down to 4.4 eV due to the surface contribution.

From the result of the TDOS, it is shown that t-LLZO and Li₂PO₂N with bulk structures are all good insulators since the bandgaps are large (>4 eV). However, on the non-stoichiometric surface of c-LLZO and t-LLZO, they become electronically conductive since the Fermi levels have already moved into the conduction band. The additional states in the bandgap are contributed from the atoms on the surface, which is the main difference between bulk and slab structures. The surface state could trap external electrons because it does not connect with conduction bands. Therefore, the surface of t-LLZO can trap some external electrons, but the Li₂PO₂N surface cannot, since it has no surface state.

Figure 2-6 shows the top and side views of the excess electron distributions by taking the charge density difference before and after the excess electrons were added to the slabs. The yellow isosurfaces highlight the regions that are gaining charge density. All the levels of isosurface (transferred electron density) are 0.0001 Å⁻³ for a fair comparison. From the side view (bottom panel), the excess electrons are mainly distributed on the surfaces of the LLZO, as Figure 2-6 (a) to (c) show. In contrast, for Li₂PO₂N (Figure 2-6 (d)), the electrons are distributed underneath the surface. Even the few electrons on the surface are particular localized around O and N atoms, which have stronger electronegativity than Li.

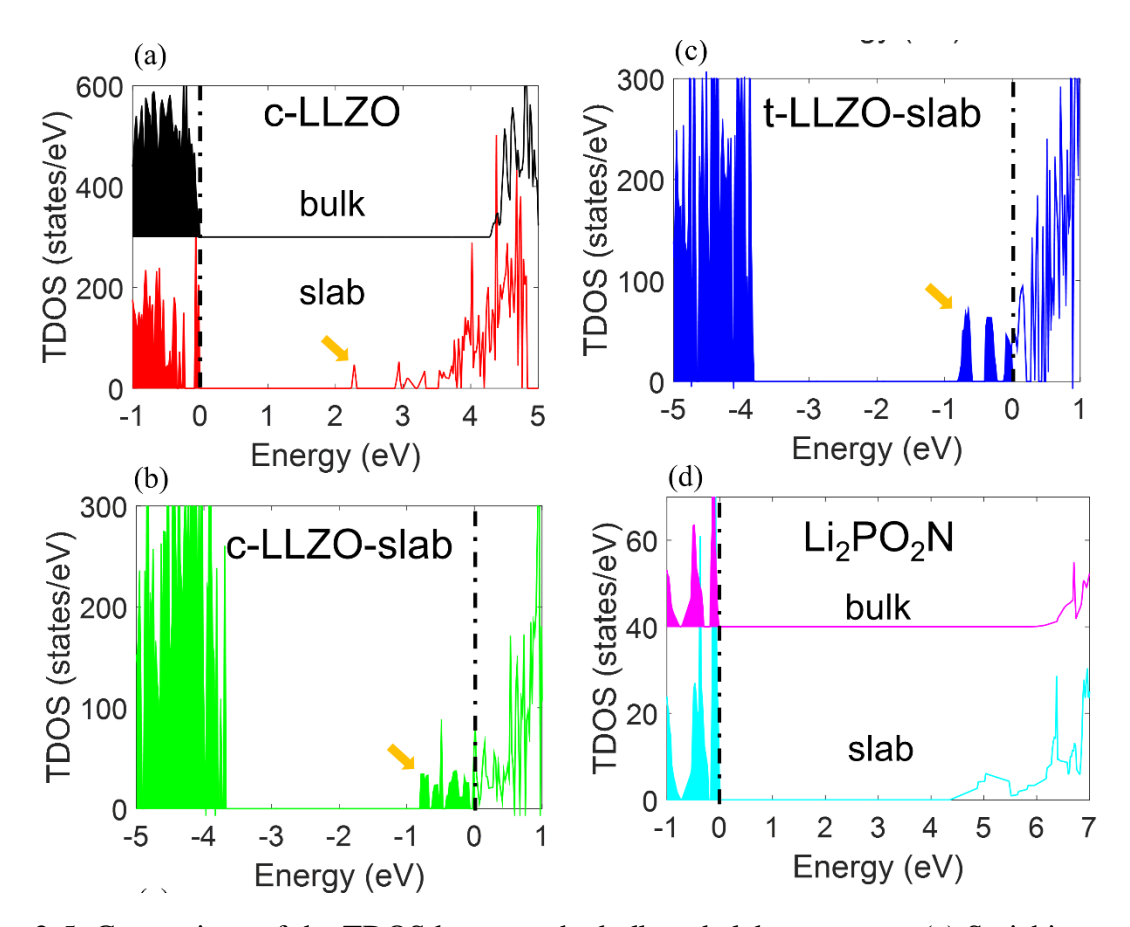


Figure 2-5. Comparison of the TDOS between the bulk and slab structures. (a) Stoichiometric c-LLZO (bulk and slab) (b) Nonstoichiometric c-LLZO slab, (c) Nonstoichiometric t-LLZO slab, and (d) Li₂PO₂N (bulk and slab). Vertical dash lines stand for the position of Fermi levels, and shaded areas represent the bands that are occupied. The orange arrow points out the additional states.

Figure 2-6 also show that the excess electrons on the non-stoichiometric surface of c-LLZO and t-LLZO are more dispersed at a lower electron density (maximum electron density of 0.0028 Å⁻³ and 0.0014 Å⁻³ for the non-stoichiometric surface of c-LLZO and t-LLZO, respectively) compared to that on the stoichiometric surface of c-LLZO (maximum of 0.0044 Å⁻³). Besides, the non-stoichiometric surface of t-LLZO has more dispersed excess electrons than the non-stoichiometric c-LLZO.

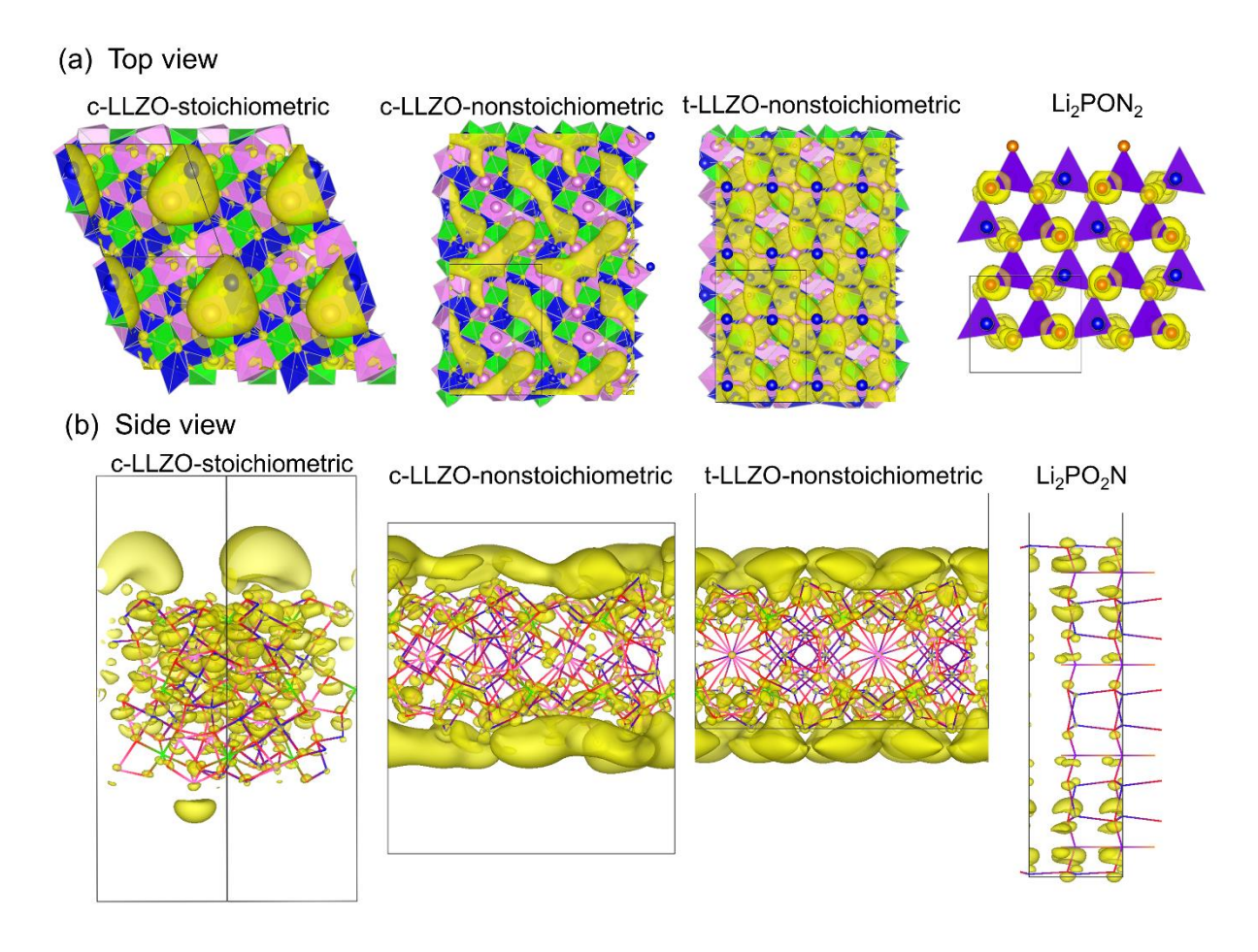


Figure 2-6. The charge density difference for different slab structures from (a) top view and (b) side view. Only the positive isosurfaces are shown to illustrate gaining electrons. All isosurfaces are at 0.0001 Å⁻³ charge density level. In (a), only the atoms (spheres) on the surface are shown.

The Li/c-LLZO interface will evolve during cycling. However, the atomistic details of this interface are still under debate. Thermodynamics calculations predicted that c-LLZO, Li₇La₃Zr₂O₁₂, can be lithiated at a voltage slightly above zero, forming a reactive layer consisting 2Zr + 1.5La₂O₃ + 7.5Li₂O with Li anode.[25] Some of these decomposed products, such as Zroxides at lower oxidation state have been identified by XPS, but metallic Zr is hard to identify in experiments.[229] In another direct TEM observation, Ma et al.[191] showed that when c-LLZO contacts with Li metal, a 6 nm thick t-LLZO layer was formed due to the diffusion of Li into thec-LLZO. This configuration is schematically drawn in Figure 2-7 (a).

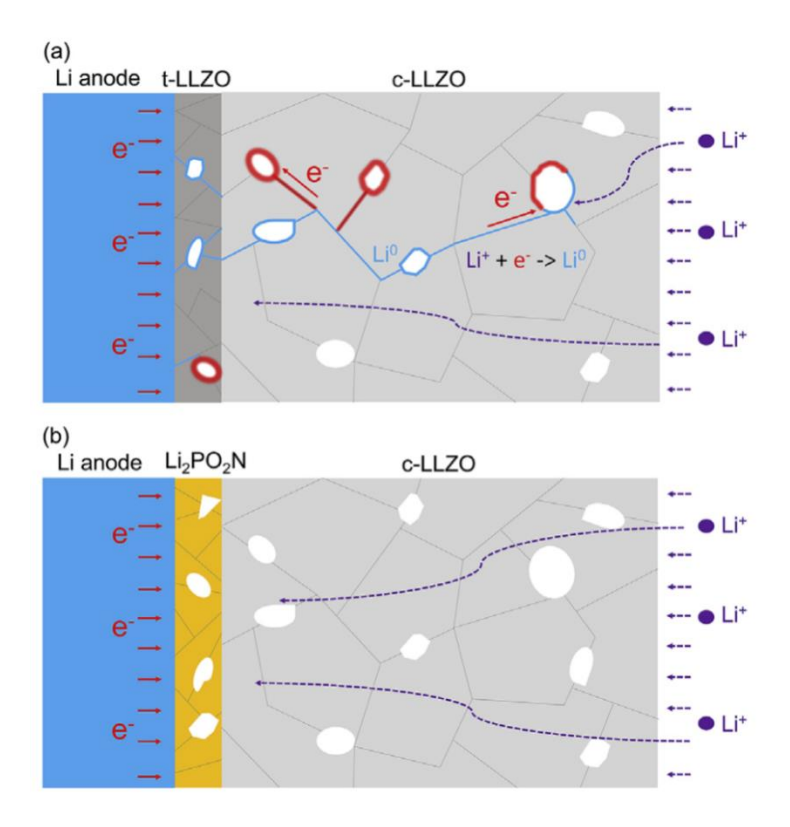


Figure 2-7. A schematic of metallic Li₀ (blue color) formation on the pore surfaces inside of c-LLZO due to the electron pathway provided by the pore surfaces and possibly grain boundaries (subject to modeling in the future). The dashed purple lines represent the Li⁺ ions passing through c-LLZO, and the red regions represent the excess electrons. Due to the different electronic structures on the pore/crack surfaces, it is proposed that (b) Li₂PO₂N interlayer will suppress dendrite formation by blocking electrons while (a) t-LLZO interlayer will not.

However, any interlayer formed at Li/LLZO interface, including t-LLZO, may not be defect free. Cracks or pores are likely to be generated due to volume change during cycling. As shown in Figure 2-7 (a), the Li-electrode can provide some excess electrons to the pore/crack surface of the t-LLZO. The dispersed electronic state on the t-LLZO surface suggests that electrons can still transport through the surface states in t-LLZO, combine with Li⁺, and reduce it to metallic Li⁰ based on the previously discussed mechanisms. Therefore, the interlayer t-LLZO cannot stop Lidendrite formation.

Based on our calculation, Li₂PO₂N coating layer might be more efficient and more defect tolerant to suppress the formation of Li dendrite. Figure 2-7 (b) illustrates the mechanism. Even pores or cracks are generated inside the Li₂PO₂N coating layer due to the cycling. From the analysis of charge density and the DOS, not only there are no surface states in Li₂PO₂N that could trap electrons, but electrons are unlikely to pass through due to the larger bandgap of 4.5 eV on the surface of Li₂PO₂N compared to the 2.3 eV band gap at the stoichiometric c-LLZO surface. Thus, Li₂PO₂N is a good insulator, with or without defect surfaces, and effectively blocks electrons passing through (even there are cracks and pores). Without the excess electrons reaching the solid electrolyte of c-LLZO, metallic Li formation inside the c-LLZO will be suppressed. Therefore, the deposition of Li₂PO₂N (ALD-LiPON) will be helpful to prevent the growth of Li dendrites. The usage of ALD-LiPON does not conflict with the effect of other buffer layers, such as Ge or Au [53, 230, 231], that modifies the electron transport on the Li-anode surface. The formation of Li-Au or Li-Ge alloy improves the contact between garnet and Li metal and gives a more uniformly distributed current on the surface of Li anode, resulting in a more uniformed deposition of metallic Li. On the other hand, the ALD-LiPON changes the electron pathway normal to the Li-anode surface by severing as a barrier that prevents electrons leaking into the solid electrolyte c-LLZO. Thus it suppresses the formation of metallic Li inside the solid electrolyte. Overall, we expect these two materials jointly prevent the Li dendrites growth.

2.5. Conclusion

We developed a multiscale modeling integration DFT calculation and phase field simulation to investigate the Li dendrite formation and growth inside solid electrolytes with microstructures and internal defects. Through DFT calculations, we discovered that the bandgap of surfaces (pores and

cracks) is lower than that in bulk in solid electrolytes. The reduced band gap pushed unoccupied state below the Li-plating potential and facilitate electron transfer from Li-metal to the surface state. Especially, in c-LLZO, the surface atoms can trap excess electrons. Also, we incorporated the new electron trapping mechanism in the phase-field model by introducing surface electron density and dendrite nucleation process, and revealed that the electrons trapped on the internal defect surfaces accelerate the Li dendrite growth and allow isolated Li nucleation to occur, leading to non-uniform dendrite growth. It also suggested that the solid electrolytes with finer grain size or higher volumetric percentage of internal defect surface have a higher probability of isolated Li nucleation. This causes an abrupt increase in dendrite penetration growth depth and growth rate. The DFT-predicted resistance of solid electrolytes to Li dendrite growth inside was ranked as: $\text{Li}_2\text{PO}_2\text{N} > \beta\text{-Li}_3\text{PS}_4 \approx \text{LATP} > \text{LLZO}$. The results are consistent with the experimental results in the literature. With this model, we can further determine the critical material properties that impact Li dendrite growth inside of the solid electrolytes, which are the internal defect surfaces (pores, grain boundaries, and junction) and their electronic conducting properties. Furthermore, via these DFT-computable electronic properties of surfaces, high throughput calculations are desirable to provide the design direction for Li dendrite resistant solid electrolyte materials.

With the revealed mechanism of Li dendrite growth through SEs and the key material properties to prevent Li dendrite, we proposed three future design directions of materials that may be helpful to resolve the Li dendrite problems in ASSLB, as shown in Figure 2-8. First, new SEs can be explored via high through output calculations based on the DFT-based surface electronic properties that we proposed in this study, such new SEs maintain larger bandgap even on the surface, and the excess electrons will not be trapped on the surfaces. Second, if searching for new SEs does not return promising results, we can further modify the pore surfaces and grain

boundaries in SEs to increase the smaller bandgap and prevent excess electrons from staying on the surfaces. Lastly, as discussed before, coating a buffer layer at the Li/SEs interface, such as Li₂PO₂N (ALD-LiPON), can also mitigate the Li dendrite growth in SEs.

Li anode Li₂PO₂N Solid electrolyte

B' OLI'

Figure 2-8. Proposed future design direction of materials to prevent Li dendrite growth through SEs.

APPENDIX

c-Li₇La₃Zr₂O₁₂

Although it is believed the Al doping, such as Li_{6,24}Al_{0,24}La₃Zr₂O_{11,98},[232] is essential to maintain the cubic structure and achieve high Li conductivity, a cubic Li₇La₃Zr₂O₁₂ as characterized by Xie et al.[233] was used in our model due to the low concentration of Al. Herein, the unit cell of c-LLZO contains 192 atoms that include eight formula units of Li₇La₃Zr₂O₁₂. The Li atoms were assigned on the partially-occupied 24d and 96h sites in c-LLZO via the distribution principle proposed by Cussen and O'Callaghan[234, 235] and Xie et al.[233], which minimizes the energy by avoiding the electrostatically-unfavorable Li⁺ configurations. Through this guided distribution principle, the energy deviation among different Li configurations can be reduced to ~0.1 eV/unit cell, which is much smaller than the entirely random Li distribution, which leads to an energy deviation as high as ~3 eV/unit cell. The structure with the lowest energy was taken for further study, and the number of Li atoms in 24d and 96h sites is 13 and 43, respectively, which is similar to the measured occupancies [233].

Slab models were used to mimic the surface structures of LLZO. The slab models of c-LLZO were cut from bulk structures on the direction of (110) with 20 Å of vacuum. This orientation has been shown to be the most stable surface for c-LLZO.[67] For the stoichiometric surface, the slabs were constructed first with only La, Zr, and O atoms, which increased the symmetry to P2/C. Then Li atoms were inserted into the slab structure by the abovementioned guided distribution principle. In this case, the configuration with both La-Li co-terminated surfaces gives the lowest energy, which is consistent with the previous report.[67] The stoichiometric ratio could be maintained if 50% of the La atoms on the surface are deleted and thus resulting in the elemental ratio of Li₄₂La₁₈Zr₁₂O₇₂. For the non-stoichiometric cases, from the DFT research of Thompson et al.[67], it was suggested that the La-Li co-terminated surfaces are the most stable surface for non-

stoichiometric c-LLZO. Therefore, in this study, the La-Li co-terminated non-stoichiometric slabs of c-LLZO were used, and the lowest surface energy is $0.88J/m^2$, which is similar to what Thompson et al.[67] calculated (0.90 J/m²). Several non-stoichiometric slabs of c-LLZO with different Li concentration were calculated to compare their surface energies and the structure with the lowest energy was picked for the analysis of electronic properties. The thickness of all the slabs is similar to the LLZO slab model of Thompson et al.[67], which is around 13 Å.

β-Li₃PS₄

The Li distribution in bulk β -Li₃PS₄ was measured in another study [236] by x-ray diffraction that showed the 8d site (Wyckoff notation) was fully occupied, 4b and 4c site was 70% and 30% occupied by Li atoms, respectively. On the other hand, a DFT study [237] for different configurations of Li atoms in bulk β -Li₃PS₄ revealed that the structure with 8d and 4d fully occupied but 4c empty has the lowest energy. In this study, we chose the atomic structure that was suggested by the abovementioned computational research, which also simplifies the configuration of Li atoms. A bulk β -Li₃PS₄ unit cell consists of 16 atoms with a space group of Pnma. Considering the PS₄ polyhedral blocks in β -Li₃PS₄, a suitable surface orientation would be the one that preserves the PS₄ units and Li-S bonds, which we found that the (100) direction with a symmetrical termination of S atoms and a stoichiometric ratio matches the requirements. Upon calculating the surface energy, which converged with six or more layers of PS₄, it is low as 0.19 J/m² that indicates this is an energetic-favorable slab.

LATP

It was reported that the ionic conductivity of $Li_{1+x}Al_xTi_{2-x}(PO_4)_3$ reaches the maximum at x=0.3 [238], and the crystal structure and the atom positions have been revealed by a neutron diffraction

analysis [239, 240]. The unit cell contains six formulas with a space group of $R\overline{3}c$. Computational studies of first principle calculation have used Li_{1.17}Al_{0.17}Ti_{1.83}(PO₄)₃ (seven Li atoms) [25] and LiTi₂(PO₄)₃ (six Li atoms) [241] to represent LATP. In this study, we chose Li_{1.17}Al_{0.17}Ti_{1.83}(PO₄)₃ as its ratio is close to the one that has the highest ionic conductivity and also simplifies the distribution of Li atoms. It has been studied that there are two sites for Li atoms, noted as Li(1) and Li(2). Li(1) has been found to be fully occupied at 6b sites, but the Li(2) sites have been argued and claimed to be at 6a [239] or 36f [240, 242] site. The 36f site for Li atom was picked in this study as both experimental and computational results confirmed it. One of the Ti atoms in LiTi₂(PO₄)₃ was randomly chosen to be replaced by Al atom, and the Li was placed at the 36 sites around it, which was based on the computational result [242].

To the best of our knowledge, no computational or experimental study has revealed the most stable LATP surface structure. Same as the preserved -PS₄ polyhedral in β-Li₃PS₄ surface structure, keeping the -PO4 polyhedral was the principle when cleaving the surfaces. Under the condition, (001) and (012) directions were chosen, and the two Al atoms were distributed in two different situations, where they both stay at the surface or bulk to maintain a symmetrical slab for calculating the surface energies, as Figure S2 shows the testing atomic surface structures. The selected (012) direction is same as the lattice plane that was shown in a high-resolution TEM (HRTEM) image of one nanocube edge of NASICON-NaTi₂(PO₄)₃ [243], which consisted an interplanar distance of 6.1 Å that is also similar to the distance of Ti-Ti (6.0 Å) along (012) direction of LATP. Several different symmetrical terminations of the slabs, such as O, Li, Ti, and Al have been calculated along these two orientations for the surface energies to evaluate the most stable surface structure. Among those, only the (012) direction is possible to have a stoichiometric and symmetrical slab that is terminated by Li atoms after deleting the surface O atoms (from TiO₆ blocks) and 50% of

the Li atoms with Al distributed on the surface layer, and it also has a relatively small surface energy of 0.37 J/m^2 . Therefore, it was selected to represent the LATP surface structure.

LiPON

The ALD-LiPON composition has been determined as Li₂PO₂N [195], also called SD-Li₂PO₂N. Its atomic structure has been discussed [196] and was taken for this study as well. A unit cell of bulk Li₂PO₂N consists of 4 formulas with a space group of Cmc2₁. The stoichiometric surface structure was taken from the literature [170, 244], which was cut along the direction (100) of bulk structure and preserved the PN₂O₂ polyhedral and terminated symmetrically with Li atoms on both ends. Four (Li₁₆P₈O₁₆N₈) or more layers of –P-N-P- is enough for the convergence of the surface energy.

The final and the most energetic-favorable surface structures used in later DOS and charge density calculation are shown in Figure 2-9.

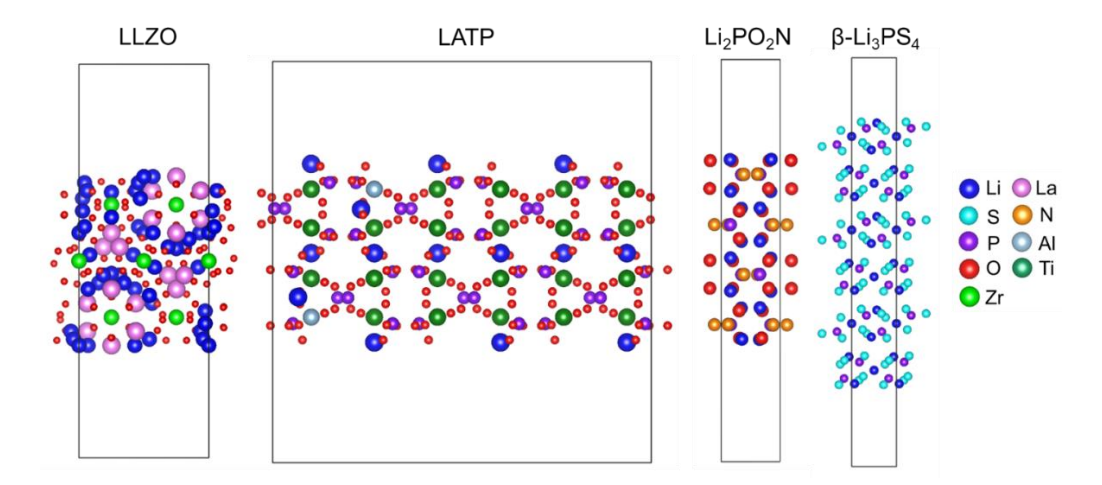


Figure 2-9. The most energetic-favorable surface structure for different solid electrolytes.

Investigation of the most stable surface

First-principles calculations were performed via the Vienna Ab initio Simulation Package (VASP) [203] based on plane-wave DFT. The surface calculations were mainly performed with the semi-local generalized gradient approximation [205] of Perdew, Burke, and Emzerhof (PBE) [206] Since the Zr in c-LLZO and the Ti in LATP are early-transition metals, it may not be necessary to apply Hubbard-type correction U, as of how the previous studies calculated for these two materials [67, 245]. The surface energy calculation was the same ass the previous studies [67, 170] that included the correction of chemical potential for the excess/deficient atoms

$$\gamma = \frac{1}{2A} \left(E_{slab} - n_{formula} * \mu_{bulk} - \sum n_i \mu_i \right)$$
 Eq. 2-1

where A is the cross-section area, E_{slab} is the total energy of the slab, $n_{formula}$ is the integer number of stoichiometric formula units in the slab, μ_{bulk} is the energy of one formula unit of corresponding bulk structure, n_i is the number of atoms of type i in the slab in excess of the stoichiometric amount. μ_i is the chemical potential of element i, which was tabulated from the total energy of its equilibrium phases against Li metal. For example, the equilibrium phases of LATP vs. Li are Ti₃P, TiAl, Li₃P and Li₂O [25] and the relationship between the total energy/formula, E, and their chemical potential, μ_i could be represented as:

$$E(Ti_3P) = 3\mu_{Ti} + \mu_P$$

$$E(TiAl) = \mu_{Ti} + \mu_{Al}$$

$$E(Li_3P) = 3\mu_{Li} + \mu_P$$

$$E(\text{Li}_2\text{O}) = 2\mu_{\text{Li}} + \mu_{\text{O}}$$

$$E(\text{Li}_{\text{BCC metal}}) = \mu_{\text{Li}}$$

The chemical potential of each element of c-LLZO was obtained from the literature [67] and listed with our tabulated results of LATP in Table 2-3. The calculated results of surface energy for different LATP surface structures are listed in Table 2-4, and we chose 012-1-Li as the final surface structure of LATP.

Table 2-3. Chemical potentials (eV/atom) used in surface energy calculations.

	Li	La	Zr	О	
LLZO[67]	-1.904	-5.165	-8.481	-10.542	
	Li	Al	Ti	P	0
LATP	-1.904	-2.537	-8.111	-7.931	-10.377

Table 2-4. Comparison of the surface energy for different surface structures of LATP.

Name	Stoichiometric or nonstoichiometric?	Atomic ratio	Al position	Surface energy (J m ⁻²)
001-1-O	Nonstoichiometric	Li ₁₂ Al ₂ Ti ₂₂ P ₃₆ O ₁₄₄	top-bottom	1.4394
001-2-O	Nonstoichiometric	$Li_{12}Al_{2}Ti_{22}P_{36}O_{144}$	middle	1.2068
001-3-Li	Nonstoichiometric	$Li_{16}Al_{2}Ti_{22}P_{36}O_{144}$	top-bottom	0.4282
001-4-Li	Nonstoichiometric	$Li_{16}Al_{2}Ti_{22}P_{36}O_{144}$	middle	0.4258
012-1-Li	Stoichiometric	Li ₁₄ Al ₂ Ti ₂₂ P ₃₆ O ₁₄₄	top-bottom-1	0.3743
012-2-Li	Stoichiometric	$Li_{14}Al_2Ti_{22}P_{36}O_{144}$	top-bottom-2	0.3741
012-3-Li	Stoichiometric	$Li_{14}Al_2Ti_{22}P_{36}O_{144}$	top-bottom-3	0.3736
012-4-Li	Stoichiometric	$Li_{14}Al_{2}Ti_{22}P_{36}O_{144}$	middle-1	0.4722
012-5-Li	Stoichiometric	$Li_{14}Al_{2}Ti_{22}P_{36}O_{144}$	middle-2	0.4732
012-6-Li	Stoichiometric	$Li_{14}Al_{2}Ti_{22}P_{36}O_{144}$	middle-3	0.4727
012-7-Li	Nonstoichiometric	$Li_{20}Al_{2}Ti_{22}P_{36}O_{156}$	top-bottom	2.6460
012-8-Li	Nonstoichiometric	$Li_{20}Al_{2}Ti_{22}P_{36}O_{156}$	middle	2.7123
012-9-O	Nonstoichiometric	$Li_{14}Al_{2}Ti_{22}P_{42}O_{180}$	top-bottom	2.3751
012-10-O	Nonstoichiometric	$Li_{14}Al_{2}Ti_{22}P_{42}O_{180}$	middle	2.1878

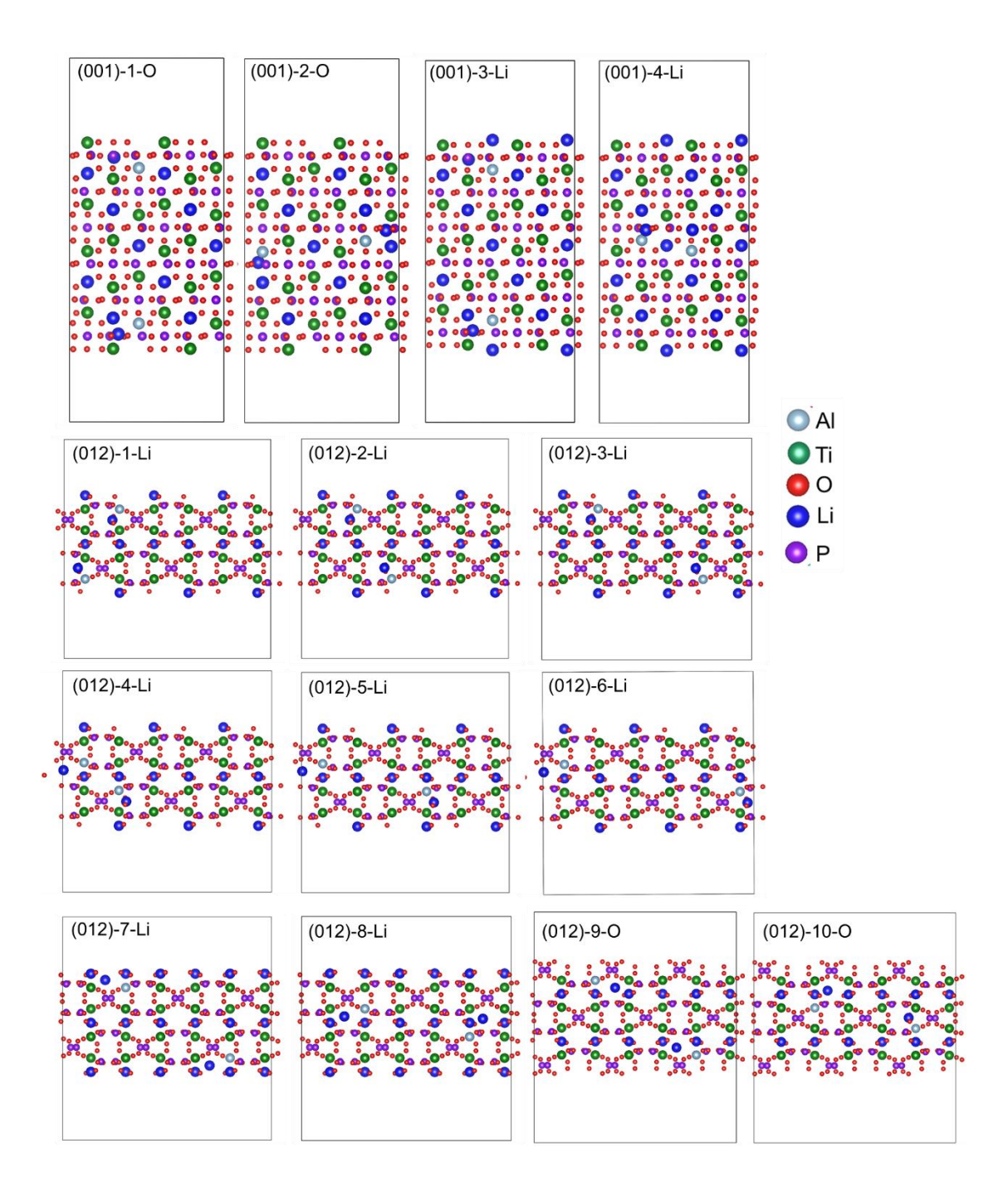


Figure 2-10. LATP surface structures with different orientations, terminations, and Al distributions, detailed calculation results are listed in Table 2-3 and Table 2-4.

The most stable surface of cubic LLZO (c-LLZO) have been calculated and reported [67], but there is no information for tetragonal LLZO (t-LLZO) yet. To find the most stable surface for further study of comparison of electronic properties between bulks and surfaces, first-principle

calculations were performed, and the computational details have been explained in the main text. Several symmetric slabs with different direction and termination were built, as Figure 2-11 shows. Because the Zr sublattice in LLZO is close to Body-Centered Cubic (BCC) crystal, (110) and (001) orientations were selected that are the typical orientations yield the lowest energy. The label on the top of each structure represents the termination of the slab, La-Li means it is a co-terminated by La and Li atoms. The calculated surface energies are shown in Table 2-5, which is based on the equation (1) in the main text. The Li-La co-terminated (110) surface and the Li-terminated (001) surface exhibit relatively low surface energy compared to other termination, which is 1.04 Jm⁻² and 1.08 Jm⁻², respectively. To choose a study example for the analysis of electronic properties, the Li-La co-terminated (110) surface was chosen since its surface energy is the lowest one.

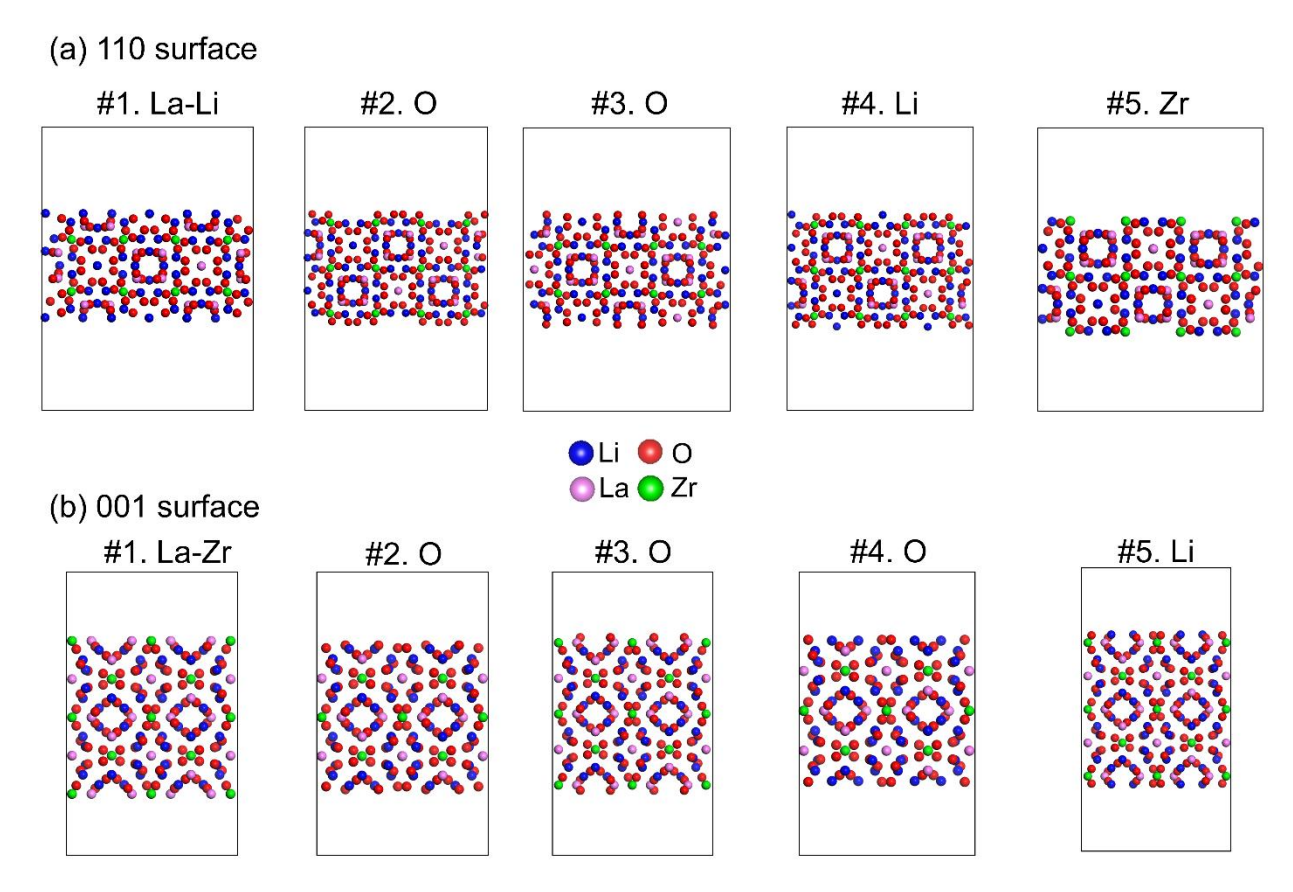


Figure 2-11. Symmetric slab structures of t-LLZO oriented along (a) (110) direction and (b) (001) direction. The labels represent the terminated atoms.

Table 2-5. Calculated surface energy (Jm-2) for t-LLZO slabs with different orientation and termination.

110 surface -	#1. La-Li	#2. O	#3. O	#4. Li	#5. Zr
	1.04	2.29	2.51	1.97	1.38
001 surface -	#1. La-Zr	#2. O	#3. O	#4. O	#5. Li
	1.53	4.61	1.28	1.61	1.08

Table 2-6. DFT Computed Surface Energy.

Surfaces	Slab structures	Surface energy (J/m ²)		
Surfaces	Siao structures	This study	Literature	
c-LLZO-stoichiometric (110)	$Li_{42}La_{18}Zr_{12}O_{72}$	0.85	-	
	$Li_{90}La_{40}Zr_{24}O_{144}$	1.04	— 0.90[67]	
c-LLZO-non-stoichiometric (110)	Li ₆₃ La ₂₈ Zr ₁₆ O ₉₆	0.88	(Li ₅₈ La ₂₈ Zr ₁₆ O ₉₆)	
	Li ₆₁ La ₂₈ Zr ₁₆ O ₉₆	0.91	— (L158La ₂₈ L1 ₁₆ O96)	
t-LLZO-non-stoichiometric (110)	$Li_{64}La_{28}Zr_{16}O_{96}$	1.04	-	
Li ₂ PO ₂ N (100)	$Li_{16}P_8O_{16}N_8$	0.46	-	

Electronic Structure Analysis

Core-valence electron interaction was treated using projector augmented wave (PAW) [204] and two different levels of theory were implemented: the semi-local generalized gradient approximation [205] of Perdew, Burke, and Emzerhof (PBE) [206] and the hybrid functional of Heyd, Scuseria, and Ernzerhof (HSE06) [207, 208]. The HSE06 calculation results about the bandgap information are listed in Table 2-1 and the TDOS is plotted in Figure 2-13. Since the Zr in c-LLZO and the Ti in LATP are early-transition metals, it may not be necessary to apply Hubbard-type correction U, as of how the previous studies calculated for these two materials [67, 245].

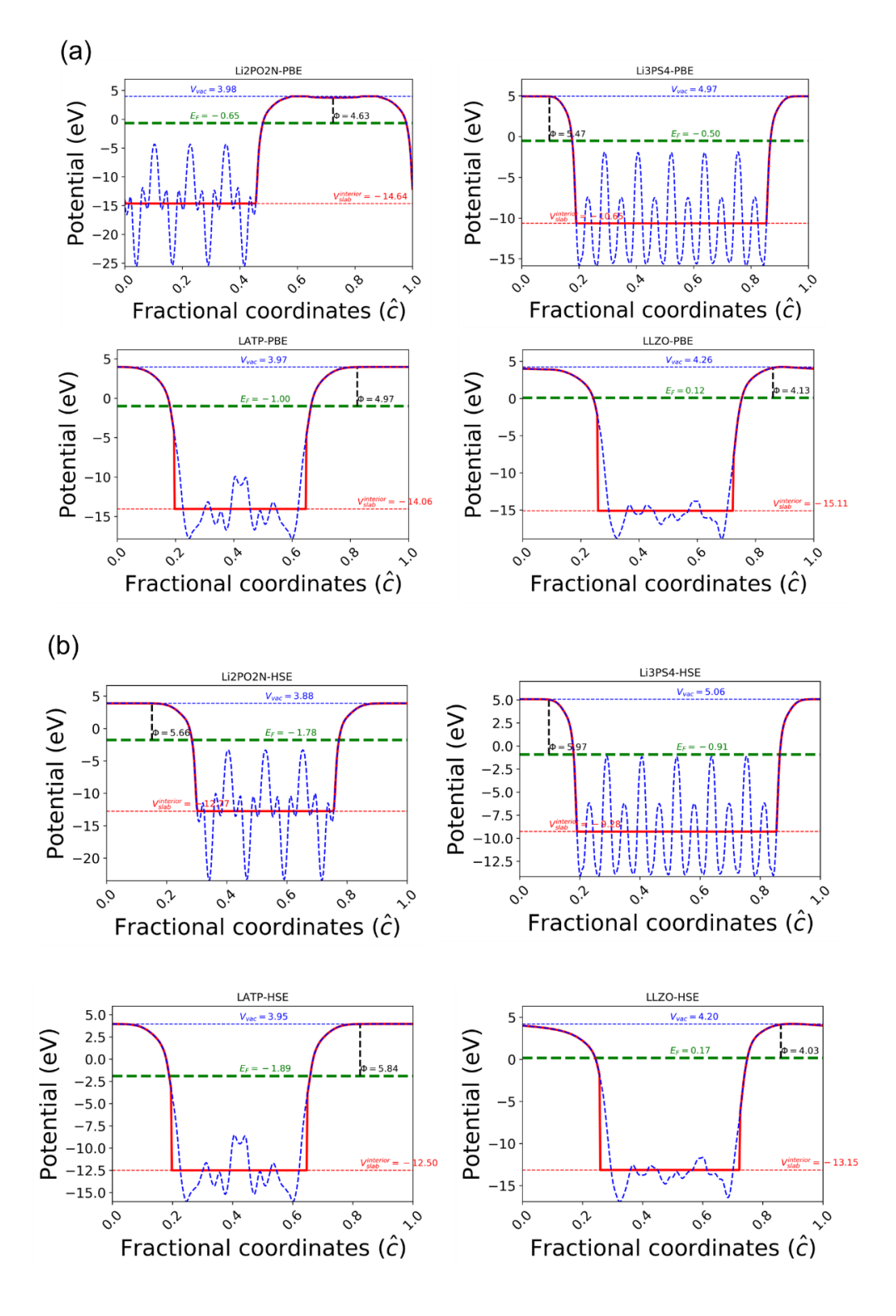


Figure 2-12. Electron potential in slab cell for different materials from (a) GGA-PBE and (b) HSE06 calculations. V_{vac} stands for the potential at vacuum, E_F is the Fermi level, $V_{slab}^{interior}$ is the potential in slab, and Φ is the work function.

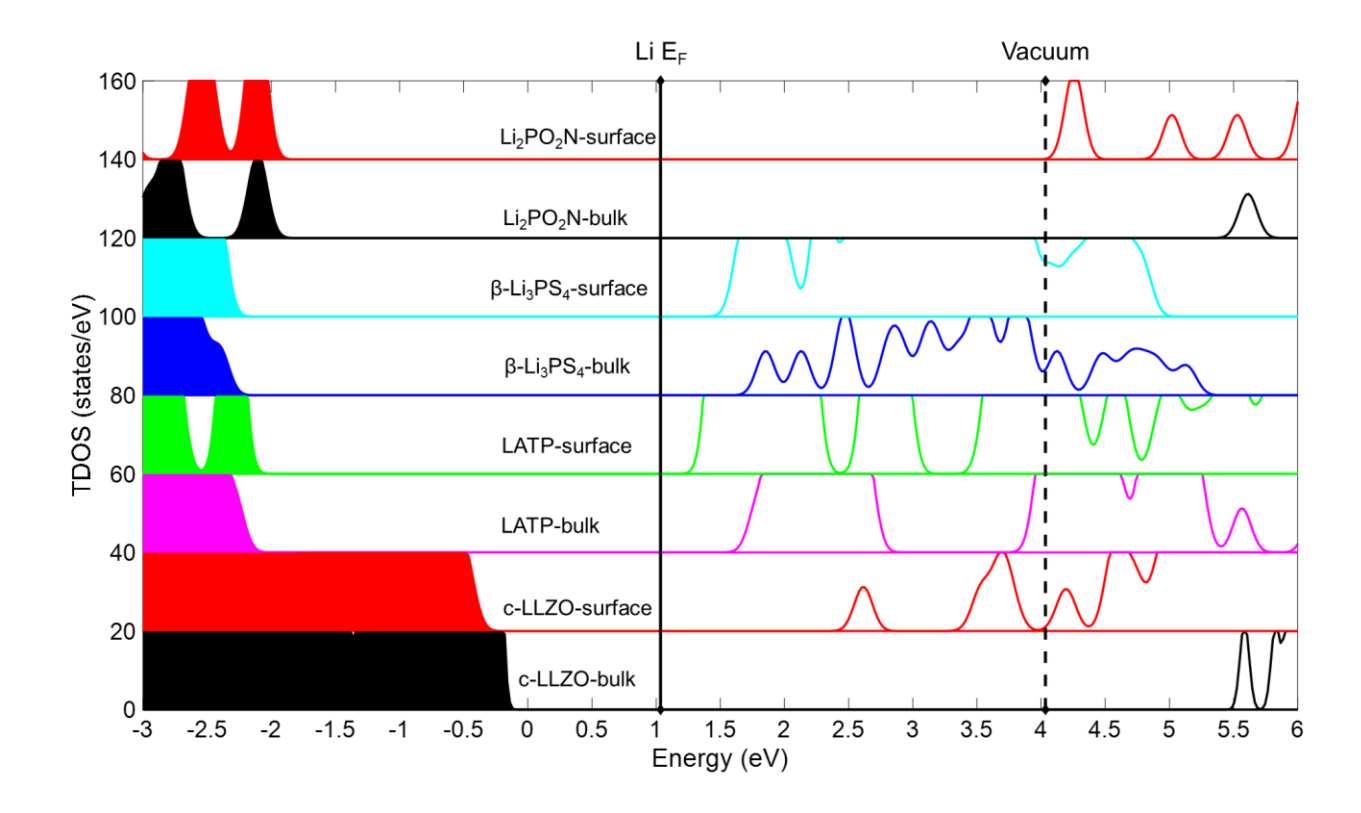


Figure 2-13. Total density of states calculated by DFT HSE06 calculation. Li E_F stands for the Fermi level of Li metal, the vacuum level is plotted as vertical dashed line.

The charge density difference was evaluated before and after the additional electrons were added to the relaxed surface structures (slab with extra electrons minus neutral slab. The amount of inserted electrons was normalized by the cross-section area (along c-axis) of the slab and listed in Table 2-7 and Table 2-8.

Table 2-7. Amount of additional electrons in each slab based on difference cross-section area, plotted in **Figure 2-2**.

Surface structures	Cross-section area per unit cell(Ų)	Excess electrons	Excess electrons per unit area at the surface (#/Ų)
c-LLZO	118.23	0.5460	
LATP	216.54	1	0.0046
β -Li ₃ PS ₄	50.31	0.2323	0.0046
Li ₂ PO ₂ N	25.30	0.1168	

Table 2-8. Amount of additional electrons in each slab based on difference cross-section area, plotted in **Figure 2-6**.

Slab structures	Cross-section area (Ų)	Excess electrons	Excess electrons per unit area at the surface (#/Ų)
c-LLZO-stoichiometric	118.23	0.49	
c-LLZO-nonstoichiometric	239.13	1	0.0021
t-LLZO-nonstoichiometric	235.21	0.98	0.0021
Li ₂ PO ₂ N	25.30	0.11	

Incorporating SE surface excess electron impact

According to the previous study [170], the surface c-LLZO could be either stoichiometric or non-stoichiometric since both have similar surface energies. Not only the lower bandgap (2.3 eV) from the stoichiometric surface would get more electrons in conduction bands than bulk, but also the non-stoichiometric surface (Li segregated) would have metal-like behavior because the Fermi level has been lifted to conduction bands. This implies there are some electrons would transfer from anode to c-LLZO surfaces. Even though, the surfaces could still maintain neutral since the measured electrical conductivity (~10⁻⁸ S cm⁻¹) [51] is much lower than the measured Li-ion conductivity (~10⁻⁴ S cm⁻¹) [246], it is expected that the Li-ion could sufficiently compensate the charges of additional electrons on the c-LLZO surfaces. This amplifies the effect of trapped electrons on the extended internal defects, or a "worst" scenario for Li-dendrite nucleation.

Therefore, to estimate the intrinsic surface electron concentration in c-LLZO, we could use the density of states of non-stoichiometric c-LLZO surface as input for the phase-field model and assume constant equilibrium electronic surface states during electrodeposition. The electron distribution of a given system is described as:

$$n = \int_{-\infty}^{+\infty} F(\varepsilon) D(\varepsilon) d\varepsilon = \int_{-\infty}^{+\infty} \frac{D(\varepsilon)}{1 + e^{(\varepsilon - \varepsilon_F)/k_b T}} d\varepsilon$$
 Eq. 2-2,

where ε is the energy of states, $F(\varepsilon)$ is the Fermi-Dirac distribution, $D(\varepsilon)$ is the density of states per volume in the unit of $[(eV \cdot Å^3)^{-1}]$, ε_F is the Fermi level, k_b is the Boltzmann constant and T is the temperature. The surface trapped electron concentration at room temperature, c_{surf} , can thus be estimated with the 0 K DFT data and a temperature correction factor (λ_T) , by integrating at the Fermi level,

$$c_{surf} \approx n_{Fermi} = \int_{\varepsilon_F - k_b T}^{\varepsilon_F + k_b T} \frac{\lambda_T D(\varepsilon_F)}{1 + e^{(\varepsilon_F - \varepsilon_F)/k_b T}} d\varepsilon \approx 2k_b T \frac{\lambda_T D(\varepsilon_F)}{2} = \lambda_T D(\varepsilon_F) k_b T$$
 Eq. 2-3.

Taking unit value for λ_T and DFT data of $D(\varepsilon_F)$, the concentration of the trapped electrons on the surface of nonstoichiometric c-LLZO was calculated to be around 0.337 mol/L. [170]. Since the focus is on the intrinsic and static material properties on the internal defects in SE, we did not consider how the Fermi level changes with the applied voltage.

The difference of charge density for the stoichiometric surface of c-LLZO

To validate the electrons on the stoichiometric surface of c-LLZO are much localized than other surfaces, the isosurface of charge density in Figure 2-6 (a): c-LLZO-stoichiometric is increased to 0.0002 Å⁻³. At this level, only the slab of c-LLZO-stoichiometric could exhibit the isosurface, which means the charge densities of other isosurfaces are much dispersed instead of being localized because the amount of inserted electrons per area is the same in each slab. Also, the electrons on the surface in Figure 2-14 seem to be localized on the top of La atoms. This result

agrees with the analysis of the local density of states in Figure 2-3, which shows the additional electrons filled the surface states that are mainly contributed by La atoms.

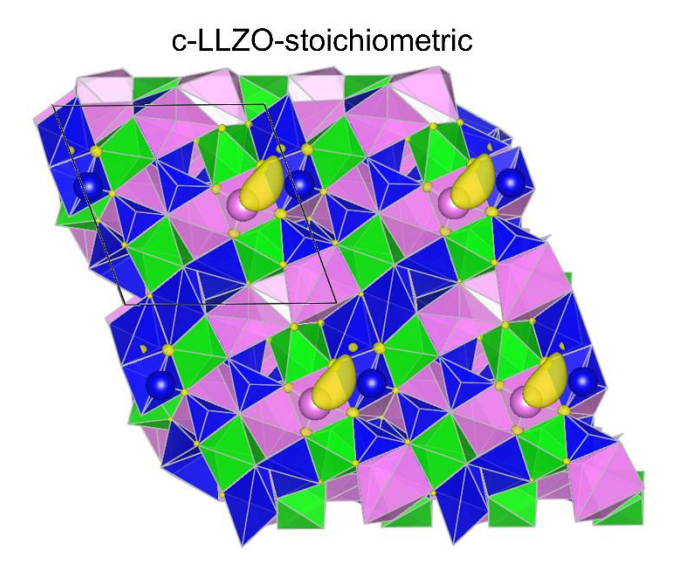


Figure 2-14. (Top view) The difference of charge density on the stoichiometric surface of c-LLZO, the level of isosurface has been increased to $0.0002~\text{Å}^{-3}$.

CHAPTER 3. Simulation of the Effect of Contact Area Loss in All-Solid-State Li-Ion Batteries

This chapter is reproduced from the work published as: **Hong-Kang Tian** and Yue Qi. "Simulation of the Effect of Contact Area Loss in All-Solid-State Li-Ion Batteries." Journal of The Electrochemical Society 164, no. 11 (2017): E3512-E3521. [187]

3.1. Summary

Maintaining the physical contact between the solid electrolyte and the electrode is important to improve the performance of all-solid-state batteries. Imperfect contact can be formed during cell fabrication and will be worsened due to cycling, resulting in degradation of the battery performance. In this paper, the effect of imperfect contact area was incorporated into a 1-D Newman battery model by assuming the current and Li concentration will be localized at the contacted area. Constant current discharging processes at different rates and contact areas were simulated for a film-type Li|LiPON|LiCoO2 all-solid-state Li-ion battery. The capacity drop was correlated with the contact area loss. It was found at lower cutoff voltage, the correlation is almost linear with a slope of 1; while at higher cut off voltage, the dropping rate is slower. To establish the relationship of the applied pressure and the contact area, Persson's contact mechanics theory was applied, as it uses self-affined surfaces to simplify the multi-length scale contacts in all-solid-state batteries. The contact area and pressure was computed for both film-type and bulk-type all-solid-state Li-ion batteries. The model is then used to suggest how much pressures should be applied to recover the capacity drop due to contact area loss.

3.2. Introduction

Conventional Li-ion batteries usually include a liquid electrolyte, which facilitates Li-ions transport between cathode and anode. However, the applications of Li-ion batteries are still limited by the flammability and narrow electrochemical window of the liquid electrolytes [6, 18, 171]. During the past decades, several solid electrolytes [246-251] with the ionic conductivity close to the liquid electrolyte have been developed, thus enabled the development of all-solid-state batteries. The benefits of all-solid-state batteries are high energy density, non-flammability, and the large electrochemical window (if the solid electrolyte form stable interphase layers on electrode surface) [25, 252].

However, a major bottleneck for all-solid-state Li-ion batteries lies at the high interfacial resistance, which is due to two main factors, chemical effect and physical contact [18]. The chemical effect refers to the chemical changes at the solid-electrolyte/electrode interface that cause slower transport. The chemical changes include the interphase layer formation due to solid electrolyte decomposition [25], and/or Li-ion depletion zone at the interface [253] (for example, LiPON/Li₂CO₃). Physical contact induced impedance comes from the imperfect contact at the solid-electrolyte/electrode interface, which plays a more important role for batteries using solid-electrolytes than the conventional batteries employing liquid electrolytes. Liquid electrolytes can easily diffuse through the porous electrode and wet the electrode surface, so, any fracture and disconnection between solid particles will only cause electrical disconnection. However, for solid electrolytes, the fracture and disconnection will impede Li-ion transport, as well as electron transport. Thus, it is the focus of this study.

The imperfect contact at the solid-electrolyte/electrode interface is formed during cell fabrication and worsened due to cycling. The extent of the initial imperfect contact depends on the fabrication

processes. For example, two type of batteries can be synthesized by different manufacturing processes, film-type [94, 254, 255] and bulk-type [80, 256, 257] batteries. The former one usually uses deposition process and forms the amorphous structure with a less rough surface, resulting in a better interface contact than the latter one, which is commonly formed by pressing particles and has much rougher interfaces. With battery cycling, the volume of electrodes changes due to repeated insertion and removal of Li atoms. The loss of contact area would further cause decrease of capacity. Several strategies to improve the interface contact and to reduce the interface resistance have been proposed. For example, depositing a buffer layer by pulsed laser deposition (PLD) technique or atomic layer deposition (ALD) between solid electrolyte and electrodes [107, 258-260], preparing nanocomposites by a ball milling process [110, 111] to reduce the particle size and increase the surface area and utilization of supercooled liquid of glass electrolyte [261]. Another common method to improve the contact area is simply applying high pressure throughout the fabrication process and electrochemical cycling. Recently, Li et al. [76], clearly demonstrated the effect of contact pressure on the capacity of an all-solid-state Li-ion battery, which is composed of an anode of In-Li, a cathode of TiS₂, and a solid electrolyte of Li₁₀GeP₂S₁₂. Based on their results, when the applied pressure during either the fabrication process and/or the operation process increased from 19 MPa to 228 MPa, the cycle stability was enhanced considerably. The least degradation and the best capacity retention were achieved in the case of maintaining 228 MPa for both processes. Therefore, the effect of the contact pressure was illustrated clearly.

However, a quantitative model is not yet available to connect the contact pressure and the battery performance. Existing continuum models of the all-solid-state-batteries have addressed different problems, such as the discharge and charge performance of thin-film batteries [94, 262, 263] and three-dimensional micro-battery [82, 85, 264], Li-ion transport through the solid electrolyte to

intercalation electrode[165, 265], and the mechanical response of electrodes during cycling [266, 267]. Therefore, the goal of this paper is to construct a continuum model to correlate the electrochemical performance with the contact area and contact pressure. As the first step, contact area was introduced into a 1-dimensional (1-D) Newman model to simulate the discharge process of an all-solid-state Li-ion battery, which is composed of a metallic Li anode, LiCoO₂ positive electrode, and a LiPON like solid electrolyte. Since Li metal has low hardness and exhibits creep behavior at room temperature [268-270], it is more likely to maintain a good contact with the solid-electrolyte due to plastic deformation. This is consistent with the reported much higher exchange current density for the metallic Li electrode [271] than that for LiCoO₂ in all-solid-state Li-ion batteries [272, 273]. Therefore, the contact between solid electrolyte and LiCoO₂ is the focus of this study. The model can be used to correlate the loss of contact area with the discharge capacity of an all-solid-state Li-ion battery and further estimate how much pressure should be applied to recover the lost contact area and the capacity.

The relationships between the applied pressure and the contact area between solids with rough surface have been addressed by various mechanics models. The well-known Hertz [274], Greenwood-Williamson [275], and Bush [276] models are not appropriate for large contact area (>50%) because they neglect the interaction between asperity contact regions. The contact between electrode and solid-electrolyte should be viewed as contact via different length scales. The multiscale contact problem is related to the nature of electrode materials that build upon architectures of single crystals, polycrystals, primary particles, and secondary particles. Thus the contacting surface can be simplified to have self-affine property, which means the pattern of interface roughness would be repeated in different length scales. Therefore, the real contact area depends on what the length scale is focused, meaning a perfect contacted interface at macroscopic view

may not be 100% in contact at nanometer scale. The different length scale is described by wavenumbers, and the surface power spectrum density will have an exponential relationship with the wavenumber, prove the self-affine property [277-280]. Therefore, Persson's contact mechanics theory [281], which models the contact area variation from 0% to 100% as a function of applied pressure on interfaces with the multi-scale self-affine property, will be adopt for the current model.

3.3. Computational methods

3.3.1. Electro-Chemical Model definition

A 1-D model was constructed to simulate the discharge process of an all-solid-state Li-ion battery. The model includes a Li metal negative electrode, a 1500 nm-thick LiPON like solid-electrolyte, referred as Li₃PO₄, and a 320-nm thick LiCoO₂ positive electrode, as shown in Figure 3-1 (a). At the interface of electrolyte/negative electrode (x=0), the electrochemical charge transfer reaction is

$$Li \rightleftharpoons Li^+ + e^-$$
 Eq. 3-1.

The net current was described as Butler-Volmer kinetics

$$i_{\text{neg}} = FA_0 k_{\text{neg}} \left(\frac{C_{\text{Li}^+}}{C_{\text{Li all}}} \right)^{\alpha_{\text{neg}}} \left(e^{\frac{\alpha_{\text{neg}}F\eta}{RT}} - e^{-\frac{(1-\alpha_{\text{neg}})F\eta}{RT}} \right)$$
 Eq. 3-2,

where k_{neg} (SI unit: $mol/(m^2 \cdot s)$) is the rate constant of the reaction Eq. 3-1, R is the molar gas constant, F is the Faraday constant (96485 $C \cdot mol^{-1}$), T is the temperature, C_{Li^+} is the concentration of mobile Li, $C_{Li,all}$ is the total concentration of Li in the electrolyte, \propto_{neg} is the charge transfer coefficient, η is the overpotential, and A_0 is the contact area that is set it is 1 cm² in this 1-D model.

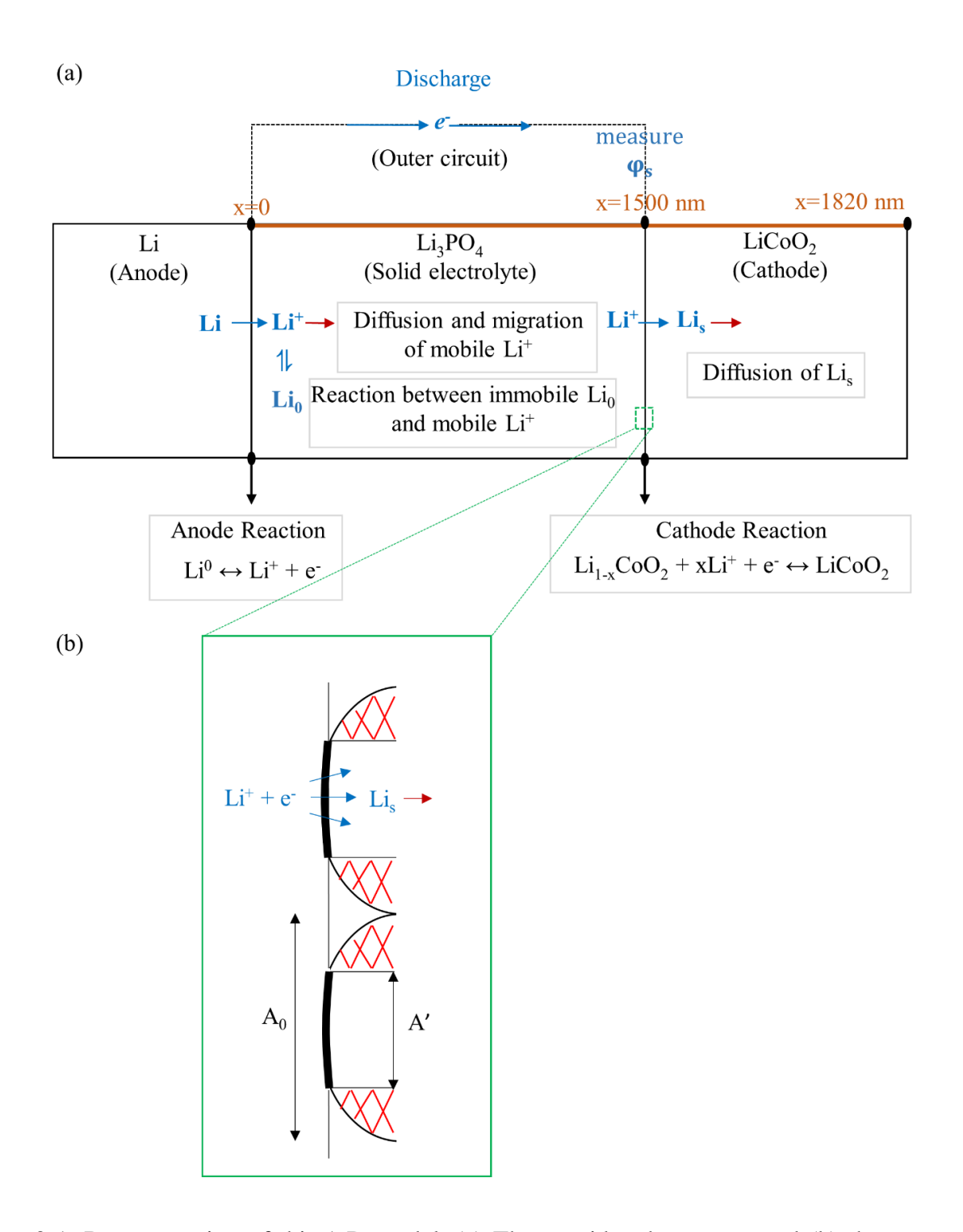


Figure 3-1. Representation of this 1-D model. (a) The considered concepts and (b) the contact between cathode and solid electrolyte.

The overpotential, η , is defined as

$$\eta = \varphi_{s} - \varphi_{ep} - E_{eq}$$
 Eq. 3-3,

where the ϕ_s is the electric potential that is same as the electrode potential, ϕ_{ep} is the solid-electrolyte potential, and E_{eq} is the equilibrium potential, which is set to be 0 for the negative electrode. Since the electron conductivity is much higher than the ionic conductivity in LiCoO₂, it is considered as a good electronic conductor [282]. Therefore, the ϕ_s is assumed to be the same everywhere in LiCoO₂ [85].

After Li⁺ being generated at the interface of electrolyte/negative electrode, only a fraction of Li⁺ can be mobile in the solid electrolyte, and this is limited by the diffusion carrier's concentration. In this case, only a fraction (denote as δ) of the total amount of Li⁺ is mobile at equilibrium is assumed,

$$C_{1,i}^{eq} = C_{n}^{eq} = \delta \cdot C_0$$
 Eq. 3-4,

where C_0 is total amount of Li and C_{n+} is the concentration of uncompensated negative charge.

Therefore, it is assumed that a portion of mobile Li⁺ would kinetically bond with the solid electrolyte and become immobile. The reactions can be expressed as

$$Li^{+} + n^{-} \stackrel{k_{r}}{\rightleftharpoons} Li_{0}$$
 Eq. 3-5,

where Li_0 is the immobile Li bonded with anions in solid-electrolyte, n^- is the uncompensated negative charges, k_d is the dissociation rate, and k_r is the reverse reaction rate. So the overall reaction rate can be written as

$$r_d = k_d C_{Li_0} - k_r C_{Li} + C_{n}$$
 Eq. 3-6.

The relationship between k_d and k_r can be described as

$$k_d = \frac{k_r C_0 \delta^2}{(1-\delta)}$$
 Eq. 3-7.

So the net production rate of mobile Li-ion that can pass through the solid electrolyte is obtained by

$$r = k_r[(C_0\delta)^2 - C_{L_i}^2]$$
 Eq. 3-8.

The transport of Li-ion in the solid electrolyte is driven by diffusion and migration, expressed by the Nernst-Planck equation and Fick's second law,

$$N_{Li^{+}} = -D_{Li^{+}} \nabla C_{Li^{+}} + \frac{F}{RT} D_{Li^{+}} C_{Li^{+}} \nabla \varphi_{1}$$
 Eq. 3-9,

$$\frac{\partial C_{Li^+}}{\partial t} = -\nabla N_{Li^+} + r$$
 Eq. 3-10,

where N_{Li^+} is the flux of Li^+ , D_{Li^+} is its diffusion coefficient, $\nabla \phi_1$ is the electrical potential gradient, and r is the net production rate of mobile Li obtained in Eq. 3-8

At the interface of solid-electrolyte/positive electrode the charge transfer reaction can be expressed as

$$\text{Li}_{1-x}\text{CoO}_2 + x\text{Li}^+ + xe^- \rightleftharpoons \text{LiCoO}_2$$
 Eq. 3-11,

with the same Butler-Volmer expression [85, 94] the net current is

$$i_{pos} = i_{0, pos} \left(e^{\frac{\alpha_{pos} F \eta}{RT}} - e^{-\frac{(1-\alpha_{pos}) F \eta}{RT}} \right)$$
 Eq. 3-12,

$$i_{0,pos} = FA_0 k_{pos} \left[\frac{(C_{\text{Li}_s,max} - C_{\text{Li}_s})C_{\text{Li}^+}}{(C_{\text{Li}_s,max} - C_{\text{Li}_s,min})C_{\text{Li},all}}) \right]^{\alpha_{pos}} \left[\frac{(C_{\text{Li}_s} - C_{\text{Li}_s,min})}{(C_{\text{Li}_s,max} - C_{\text{Li}_s,min})}) \right]^{1 - \alpha_{pos}}$$
 Eq. 3-13,

where $C_{Li_s,max}$ and $C_{Li_s,min}$ are the maximum and minimum concentration of Li in the positive electrode, respectively, and the k_{pos} is the rate constant of the reaction. The overpotential, η , is defined as the same as Eq. 3-3, but E_{eq} is the equilibrium potential of $LiCoO_2$ and it depends on the concentration of Li.

After the charge-transfer reaction, Li would be produced and intercalate into the positive electrode (denote as Li_s), and its diffusion through the positive electrode is driven by the concentration gradient, as

$$\frac{\partial C_{\text{Li}_s}}{\partial t} = -D_{\text{Li}_s} \nabla^2 C_{\text{Li}_s} + R_{\text{Li}_s}$$
 Eq. 3-14,

where D_{Li_s} , C_{Li_s} , and ∇C_{Li_s} are the diffusion coefficient, concentration, and the concentration gradient of Li_s. The reaction rate, R_{Li_s} , in the positive electrode is 0, except at the solid-electrolyte/positive electrode interface (x = 1500 nm), where R_{Li_s} (mole·s⁻¹m⁻²), would be correlated with the current.

$$R_{\text{Li}_{\text{s}}} = \frac{vI_{\text{pos}}}{n_{\text{e}}FA_{0}} = \frac{vi_{\text{pos}}}{n_{\text{e}}F}$$
 Eq. 3-15,

where I_{pos} is the current (A), i_{pos} is the current density (A/m²), v is the stoichiometric coefficient of Li, and n_e is the number of participating *electrons* in the reaction, both values are one here.

With this 1D model, a discharging process under a constant current is simulated. This process means as the constant current passing through the two interfaces, x = 0 nm and x = 1500 nm, the same amount of Li-ion will be generated and released at these two interfaces, respectively. All the Li^{+} and Li_{s} are bounded between x = 0 - 1500 nm, and x = 1500 - 1820 nm, respectively. The electroneutrality is applied in the electrolyte that gives the concentration of Li-ion equals to the negative charge. The boundary and initial conditions in this model are listed in Table 3-1. The concentration profile of Li⁺ and Li_s in the solid-electrolyte and the positive electrode, and the electrical potential at x = 1500 nm are solved. The boundary condition is the controlled value of current (C-rate) at the both end of the solid-electrolyte. Since for all-solid-state Li-ion battery, the range of C-rate usually is between 0.1 C to 10 C [6, 76, 283], the C rates are chosen to be studied in this research are 0.1, 1, 5, 10 and 20 C. The input open-circuit voltage (OCV) of Li_xCoO₂, where x varies in the range of 0.5 to 1, is given in Figure 3-3 (c). Initially, Li_{0.5}CoO₂ gives the starting voltage around 4.2 V. The simulation would end at the desired cutoff voltage. The parameters used and listed in Table 3-2 are based on the research of Danilov and Notten et al. [94], where they have fitted to the experimental data.

Table 3-1. The conditions and dependent variables in this model.

Boundary Conditions	Initial Conditions	Stop Condition	Solve for	Description	
$i_{pos} = controled$ value $\Phi_{s, neg} = 0$ $E_{eq, neg} = 0$ (Ground)	$x = 0.5$ (ratio of initial C_{Li_s}	When $C_{Li_s} = C_{Li,max}$ (at the interface of positive electrode/electrolyte)	C _{Li+} (x,t)	The electrolyte concentration of Li ions (mol/m ³)	
	to C _{Li,max})		C _{Li_s} (x,t)	The concentration of Li in LiCoO ₂	
	Ф – 1			(mol/m ³)	
	$\Phi_{s, pos} = 4$		$\Phi_{\rm s,pos}(t)$	The external electric potential of positive electrode (V)	
	$\Phi_{ m ep}=0$		$\Phi_{\rm ep}({\rm x,t})$	The electrolyte potential (V)	

Table 3-2. The parameters used in this model, which have been fitted to experimental data [94].

Control Variable	Description	Value
$\mathrm{C}_{\mathrm{Li,total}}$	The total electrolyte concentration of Li ions (mol/m³)	6.01*10 ⁴
$C_{\text{Li,max}}$ and $C_{\text{Li,min}}$	Maximum and minimum concentration of Li in the solid electrode (mol/m³)	23300 and 11650
${ m D_{Li}}^{^+}$	Li-ion diffusion coefficient in solid electrolyte_Li ₃ PO ₄ (m ² /s)	9*10 ⁻¹⁶
$D_{\mathrm{Li}_{\mathrm{s}}}$	Li _s diffusion coefficient in positive electrode_LiCoO ₂ (m ² /s)	1.76*10 ⁻¹⁵
δ	Fraction of mobile Li-ion at equilibrium	0.18
k _d and k _r	Rate constants for dissociation and recombination (mol/(m ² ·s))	2.13*10 ⁻⁵ and 9*10 ⁻⁹
k _{pos} and k _{neg}	Rate constant for reactions (mol/(m ² ·s))	5.1*10 ⁻⁴ and 0.01
$\alpha_{\rm pos}$ and $\alpha_{\rm neg}$	Charge transfer coefficient for the reactions	0.6 and 0.5

3.3.2. Incorporation of the loss of contact area in this 1-D model

As illustrated in Figure 3-1 (b), the imperfect contact at the solid electrolyte and positive electrode interface is considered. Although both electrode and electrolyte surfaces are rough, one can always reduce the contact to a flat surface with an effective rough surface. To represent the imperfect contact area, a contact factor, γ , is assigned varying

$$\gamma = \frac{A}{A_0}$$
 Eq. 3-16,

where A is the actual imperfect contact area, and A_0 is the perfect contact area (cross section area). γ ranges between 0-1.

As mentioned in the introduction part, in liquid electrolyte [284], Li-ion can diffuse through the porous electrode, fracture and disconnection of particles will only cause disconnection electronically, which means less pathways for e^- to react with Li^+ . However, for solid electrolyte, the disconnection would be even worse due to the fewer pathways for both of e^- and Li-ion to react. Therefore, the imperfect contact at the solid-electrolyte/electrode interface may cause part of the electrode material inaccessible, especially at a higher rate. The inhomogeneous Li distribution in $LiCoO_2$, observed by *in-operando* elemental mapping of an all-solid-state battery [253], may be partially caused by imperfect contact as well. Therefore, in the worst case, the loss of contact between electrode and solid-electrolyte interface would cause the loss of $LiCoO_2$ material, in which Li-ion cannot be stored. The region of the red color in Figure 3-1 (b) means the area of loss of material. In this case, the imperfect contact area, $A = \gamma A_0$ was incorporated into this model at the interface of electrolyte/positive electrode. More specifically, Eq. 3-13 is modified to represent the real contact area, as

$$i_{0,pos} = F\gamma A_0 k_{pos} \left[\frac{(C_{Li,max} - C_{Li})C_{Li+}}{(C_{Li,max} - C_{Li,min})C_{Li+,0}}) \right]^{\alpha_{pos}} \left[\frac{(C_{Li} - C_{Li,min})}{(C_{Li,max} - C_{Li,min})}) \right]^{1-\alpha_{pos}}$$
Eq. 3-17.

Since constant current discharge process is simulated and the C-rate is fixed, the current density at the solid-electrolyte side of the interface is not affected by the loss of contact area, but the production rate of Li on the positive electrode side of the interface would be scaled to match the same current. Therefore, the Eq. 3-15, which is the production rate of Li, should be adjusted by γ , as

$$R_{\text{Li}_{\text{s}}} = \frac{vI_{\text{pos}}}{n_{\text{e}}FA_{0}\gamma} = \frac{vI_{\text{pos}}}{n_{\text{e}}F\gamma}$$
 Eq. 3-18.

3.3.3. Calculate the contact area under applied load at self-affine rough interfaces

Persson's multi-scale contact mechanics theory [281] was used to establish the relationship between the contact stress and the real contact area, A, in order to provide the key parameter γ used in the above electrochemical model. The advantage of Persson's model is that it captures the fact that the real contact area depends on the observation length scale. For example, an interface may look like contact perfectly with uniform contact pressure at macroscopic view, but at microscopic view, the surface roughness will lead to non-perfect contact and non-uniform contact stress. By assuming that surface roughness has self-affined property [277-280], this model can calculate the real contact area at every length scale. Thus, it is important to define the length scales for the battery systems.

The contact mechanics is at multi-length scale, as shown in Figure 3-2 (a), where the largest contact area A_0 and the corresponding length is $L = A_0^{1/2}$, assuming isotropic in x-y direction. In the reciprocal space, the smallest wavelength is $q_L = 2\pi/L$. Therefore, any wavelength, q, can be defined via a magnification, ξ , as $q = \xi q_L$. For the longest length scale and the smallest wave length, ξ is 1. The smallest length scale for contacting would be observed in the atomic scale, which sets the upper limit of wave length q.

The surfaces are composed of asperities for both the film-type or bulk-type battery. The surface roughness power spectrum can be calculated by the Fourier transform of the height-height correlation function [285]:

$$C(q) = \frac{1}{(2\pi)^2} \int d^2x < h(x)h(0) > e^{-iq \cdot x}$$
 Eq. 3-19,

where C(q) is the power spectrum of wavelength q; $h(\mathbf{x})$ is the height of the surface above a flat reference plane that is chosen for $h(\mathbf{x})=0$. The angular bracket <---> is the ensemble averaging operator. Solid surfaces are approximately self-affine fractals, which means if observing the surface in different magnification, it looks the same because the surface pattern repeats. That being said, when the length scale changes in the self-affine region, C follows a power law of q, as $C \propto q^m \times 10^I$, as shown in Figure 3-2 (b), where m is the slope and I is the y-intercept. The lower limit of q or ξ defines the scale when the self-affine property is not held anymore. In this case, the self-affine property is considered to be non-distinguishable. For example if the diffusion-length of Li at IC rate is used to be the observed length scale, Li distribution can be considered as uniform at this scale, then the contact is not self-affined anymore. This length scale is estimated to be 3.6 μm , based on $\sqrt{4Dt}$. So the lower limit of the q is defined by the magnification ξ of around 2700 for $A_0 = 1 cm^2$ in this model. The contact area for this length scale was computed.

C(q) would be obtained from the surface information, such as root-mean-square (RMS) roughness and peak-valley value. As other research investigated the surfaces by atomic force microscopy (AFM), for the film-type cathode, such as LiMn₂O₄, LiCoO₂, LiNi_{1/3}Co_{1/3}Mn_{1/3}O₂, the RMS roughness is around 10 - 20 nm [286-290]. On the other hand, for the bulk-type cathode, the RMS roughness is around 100 - 200 nm, such as LiFePO₄, CoO+Co₃O₄, and LiNi_{0.8}Co_{0.2}O₂[291-293]. Currently, C(q) is not available for all-solid-state battery electrode and solid-electrolyte surface yet. Therefore, we rationalize C(q) for the observed RMS based on the surface analysis by Flys et

al. [279]. In their study, they also used AFM to investigate the surface profile and obtained C(q) for samples prepared with different RMS roughness, ranging from 2 to 120 nm. The result of C(q) at RMS roughness of 15 and 120 nm from the research of Flys et al. were chosen to represent the film-type and bulk-type cathode, respectively. Figure 3-2 (b) shows the power spectrum-wavelengh logarithm relationship for these two different RMS roughness. Also, it indicates that the rougher surface, which is the RMS roughness of 120 nm, has a larger slope, m, and smaller y-intercept, I.

Based on the Persson's contact mechanics theory [281], the stress distribution at the magnification, ξ , which refers to any arbitrarily chosen length scale, can be defined as

$$P(\sigma, \xi) = \frac{1}{A_0} \int_A d^2x \, \delta(\sigma - \sigma(x, \xi))$$
 Eq. 3-20,

where $P(\sigma, \xi)$ is the probability of stress distribution, $\sigma(x, \xi)$ is the interface stress distribution at any position x in the spatial coordinate, and δ is the delta function. By this definition, the real contact area A, which is projected on the interface-plane, can be directly calculated from this stress distribution as the following

$$\gamma = \frac{A}{A_0} = \int d\sigma P(\sigma, \xi)$$
 Eq. 3-21.

The integration of stress should be equal to the applied load. Therefore, the stress distribution can be obtained by solving [294],

$$\frac{\partial P}{\partial \xi} = f(\xi) \frac{\partial^2 P}{\partial \sigma^2}$$
 Eq. 3-22,

$$f(\xi) = \frac{\pi}{4} (\frac{E}{1-v^2})^2 q_L q^3 C(q)$$
 Eq. 3-23,

where E and ν are the effective Young's modulus and Poisson's ratio averaged from the two materials. C(q) is the power spectrum obtained from Eq. 3-19.

$$\frac{1-v^2}{E} = \frac{1-v_1^2}{E_1} + \frac{1-v_2^2}{E_2}$$
 Eq. 3-24,

where subscript 1 and 2 refer to the two solid materials. In this research, the solid electrolyte material Li₃PO₄ and LGPS; and the cathode materials LiCoO₂ and TiS₂ are chosen to be calculated. Their elastic properties are listed in Table 3-3.

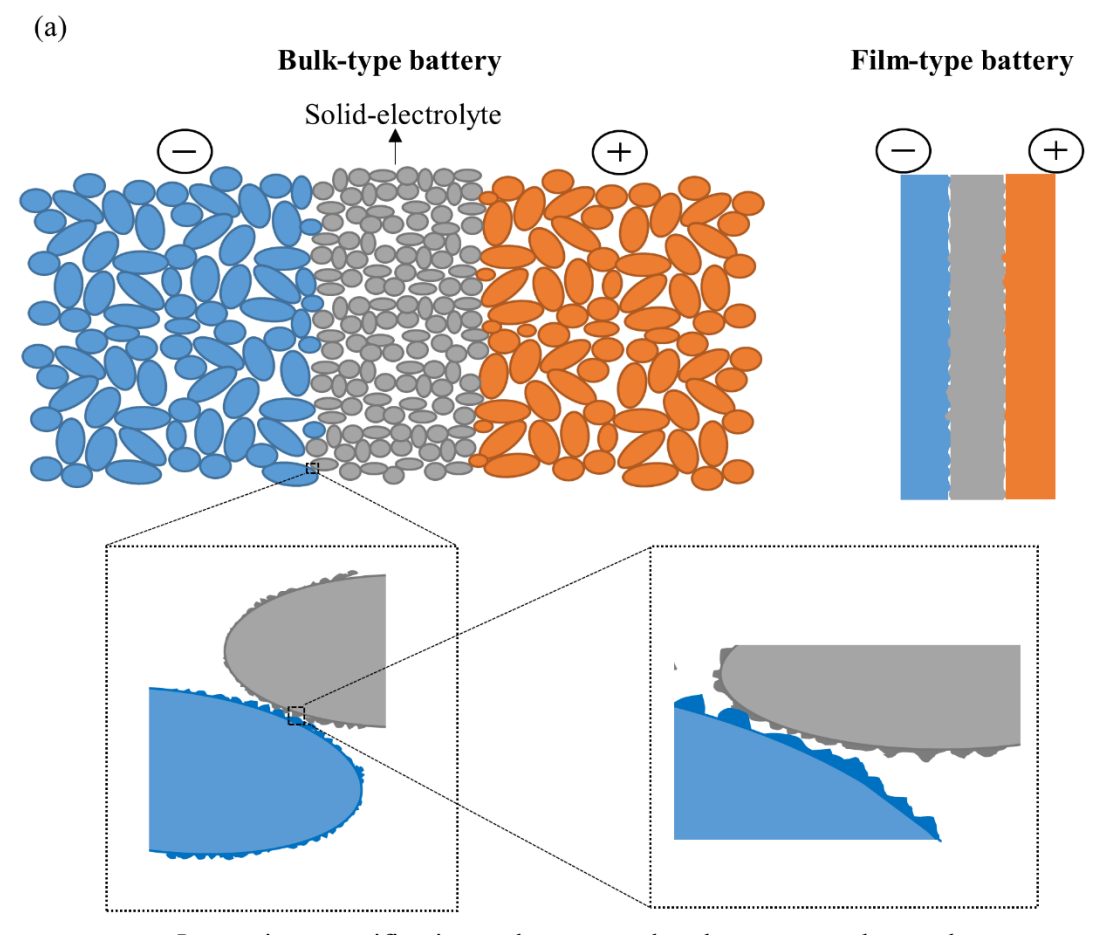
The different properties of the contact, such as elastic contact, adhesion or elastoplastic contact can be addressed by changing the initial and boundary conditions of Eq. 3-22. Since both Li₃PO₄ and LiCoO₂ are ceramic materials, the contact is considered to be elastic without adhesion in this study. For the initial condition, which means the lowest magnification $\xi = 1$, the contact area would be the cross-section area and looks like a flat and full contact. So the stress distribution P(σ ,1) = $\delta(\sigma - \sigma_0)$, σ_0 represents the applied pressure. There are also two other boundary conditions along the σ -axis are necessary. For elastic contact, P(σ , ξ) would be 0 when $\sigma \to \infty$, when $\sigma < 0$ the P(σ , ξ) should be 0 as well since there is no adhesion. With the initial and boundary conditions, the stress distribution of Eq. 3-22 can be solved, and the real contact area in Eq. 3-21 can be further obtained by

$$\gamma = \frac{A(\xi)}{A_0} = \frac{1}{\sqrt{\pi}} \int_0^{\sqrt{G}} dx \ e^{\frac{-x^2}{4}} = erf(\frac{1}{2\sqrt{G}})$$
 Eq. 3-25,

$$G(\xi) = \frac{\pi}{4} \left(\frac{E}{(1-v^2)\sigma_0} \right) \int_{q_L}^{\xi q_L} dq \ q^3 C(q)$$
 Eq. 3-26.

Table 3-3. Elastic properties for solid electrolyte and cathode materials.

	Li ₃ PO ₄	LiCoO ₂	LGPS	TiS ₂
Young's Modulus	103.4	171	21.7	228
(GPa)	[268]	[269]	[241]	[295]
Poisson Ratio	0.26	0.2	0.37	0.11
	[268]	[296]	[241]	[295]



Increasing magnification and wave number, less contact observed

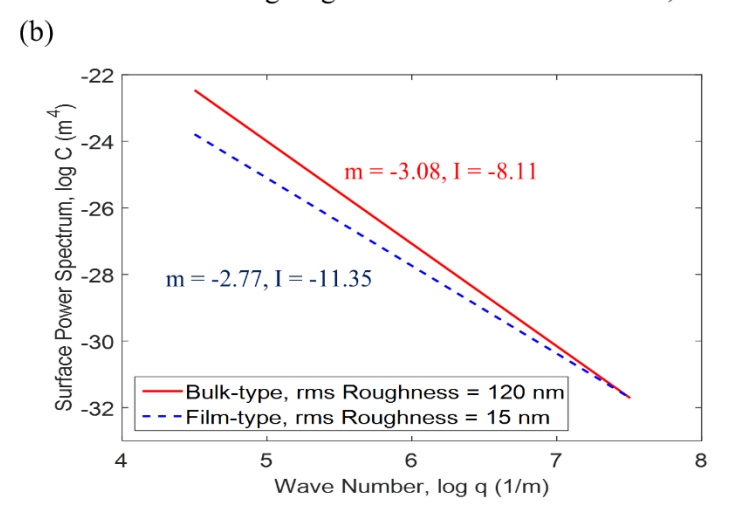


Figure 3-2. (a) Schematic of the interfacial contact for bulk-type and film-type batteries, and the contact area observed at different length scale. (b) Logarithm relationship between power spectrum and wave number at different RMS roughness [279]. Only the self-affine region is shown.

3.4. Results and discussion

3.4.1. The effect of the loss of contact area causing accumulation of Li on electrode surface

In this simulation, the battery is discharged at a constant current, and the cell voltage is the potential difference between the positive electrode and negative electrode. Since the negative electrode is grounded, which gives the potential, $\phi_{s, neg}$, is maintained as 0. The cell voltage is determined by the potential at positive electrode, $\phi_{s, pos}$, which is affected by the equilibrium potential of positive electrode, ϕ_{eq} , the over potential and the solid-electrolyte potential. The local Li concentration at the solid-electrolyte/cathode interface decides the equilibrium potential, ϕ_{eq} . Therefore, it is necessary to first check the concentration of Li on the cathode surface when the contact area is not perfect. Figure 3-3 (a) and (b) shows the variation of the local concentration of Li, C_{Li_8} , with time at the Li₃PO₄/LiCoO₂ interface (x = 1500 nm) under different contact area and two separate discharge rates, 1C and 10C, respectively.

Comparing Figure 3-3 (a) and (b), at the same discharging time, the concentration of Li is higher at 10 C than at 1 C, since higher C-rate means larger current, which causes more Li produced on the LiCoO₂ surface. If the diffusion rate is not as fast as the production rate, Li is accumulated at the LiCoO₂ surface. In both rates, at the same discharging time, the local concentration of Li in LiCoO₂ (Li₈) at the cathode surface increased when the contact area is reduced. It is because the constant current imposed the same amount of Li produced at LiCoO₂ surface, so the local concentration of Li is higher when the contact area is reduced. The local Li₈ concentration would then be continuously increased to the maximum Li concentration, which is 23000 mol/m³ for LiCoO₂.

When the local concentration of Li on LiCoO₂ surface increases with reduced contact area, it results in the reduction of OCV and the potential of LiCoO₂. Therefore, the battery voltage will reduce due to the loss of contact area, this is further analyzed in the cell discharge voltage vs. capacity plot.

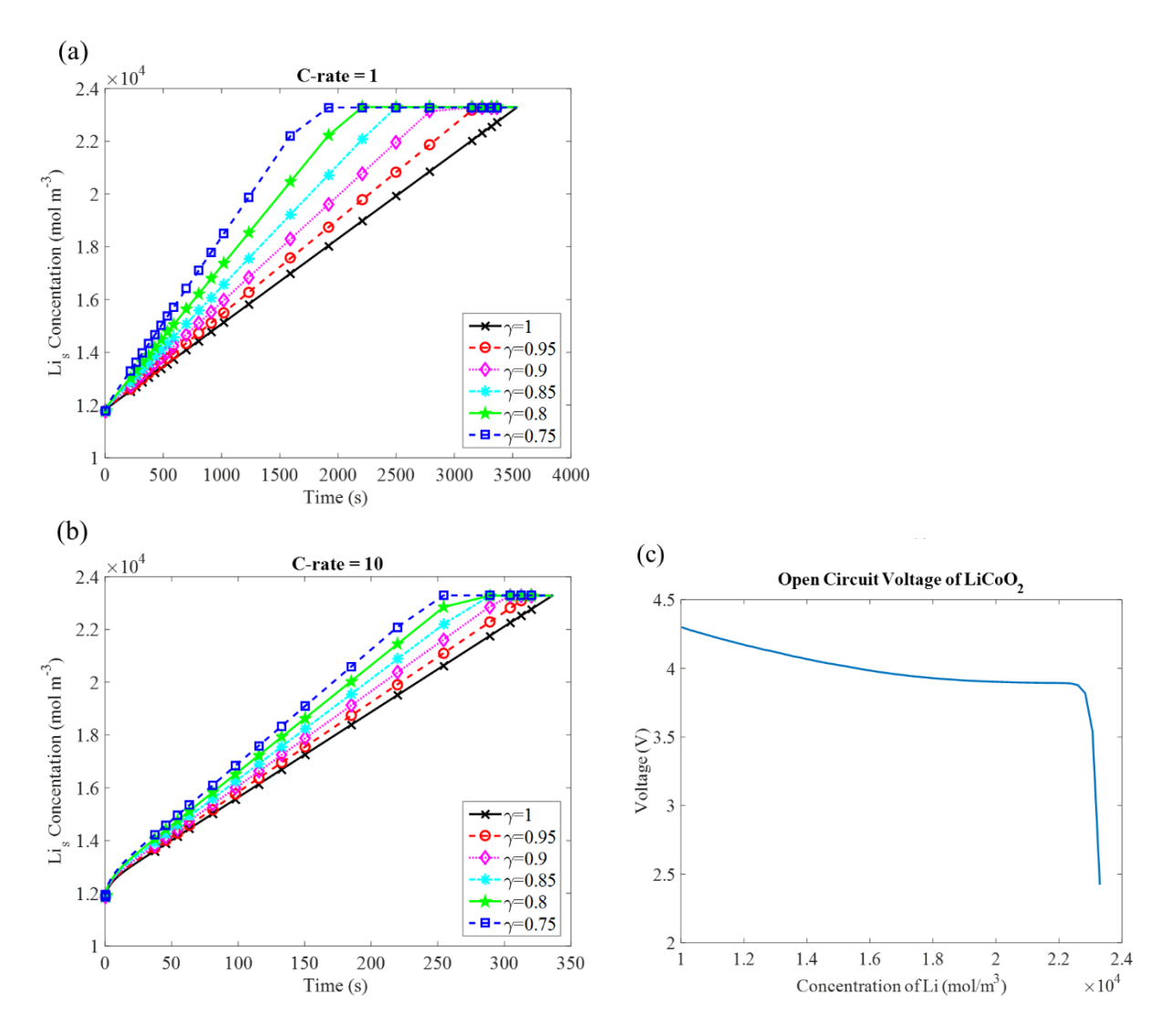


Figure 3-3. The effect of the contact area on the concentration of Li at electrolyte/cathode interface (x = 1500 nm) at different discharge time. (a) 1 C-rate (b) 10 C-rate. (c) The open circuit voltage of LiCoO₂ at different amount of inserted Li.

3.4.2. The effect of the loss of contact area on the discharge voltage and capacity

Comparing the effect of the different discharging rate, ranging from 0.1 to 20 C, with the contact area, which is expressed by contact factor, γ , varying from 1 to 0.75. Figure 3-4 shows the results of discharging curves. The cutoff range of 3.7-4.2 V for the battery voltage is used because most of the batteries operate between these values. Q_{out} is the discharging capacity per unit area, which is calculated by

$$Q_{out} = \frac{t \times C_{rate}}{A_0}$$
 Eq. 3-27,

where t is the discharging time (s). The dashed line stands for the critical capacity, which is defined as 80% of the maximum capacity since typically the battery for transport application would be seen as "end of life" when the capacity is less than 80%.

Figure 3-4 (a) shows the discharge curves with the perfect contact (γ =1) at different C rates. It shows the discharge curves for 0.1 C and 1 C are very similar. With increasing discharging rate, both the cell voltage and capacity are reduced. This result is similar to other models with perfect contact area [85, 262]. With the current model and parameter setting, the discharge capacity can still be maintained above 80% of the maximum capacity even at 20 C with perfect contact area. Figure 3-4 (b) and (c) show the discharge curves with imperfect contact at C =1 and 10, respectively. At the same discharging rate, both the discharge voltage and capacity dropped with the reduced contact factor, γ . The drop of voltage can be considered as the increase of interface resistance and ohmic loss due to loss of interface contact area. The decrease of capacity is rate dependent. For example, if discharging at 1 C, the battery would lose 20% of the capacity if the contact area is less than 80% of the cross-section area (γ = 0.8). If discharging at 10 C, the battery would be at the "end of life" if the contact area is less than 85%. This is because of the accumulation of Li on cathode surface due to reduction of contact area and the high rate. Since the diffusion rate

of Li_s is not as fast as the reaction rate, the high surface concertation of Li_s leads to less utilized electrode particles at the cutoff voltage, thus lost contact area and higher C-rate give less discharge capacity.

The definition of discharging capacity depends on the cutoff voltages, which is also known as the depth of discharge of the battery. Figure 3-5 compares the capacity loss due to contact area loss at two cutoff voltages, namely 3.8 V and 4.0 V. Here, the 100% of remaining capacity stands for the capacity that is obtained at 0.1 C discharge. Both higher rate and loss of contact area reduce the capacity. Interestingly, the loss of capacity due to contact area loss shows almost a linear relationship. At the cutoff voltages of 3.8V, the slopes of all the lines are almost 1; and at the cutoff of 4.0V, the absolute value of the slopes are all smaller than 1. For example, the slope of 0.1 C is -0.34 and the slope of 20 C is -0.26. Thus, at the cutoff of 4.0 V, the magnitude of slope is larger at lower C-rate.

It can be seen from Figure 3-4 that the cutoff voltage of 3.8 V means the cathode surface is fully lithiated, the capacity does not change with voltage much anymore. Therefore, the remaining capacity at the cutoff voltage of 3.8 V is limited by the material available on the cathode surface. Since we have assumed loss of material due to the loss of contact area, the capacity loss drops with loss of contact area with a slope of 1. For the cutoff voltage of 4.0 V, the discharging capacity is still very sensitive to the voltage, which is related to the local Li_s concertation. The local Li_s concentration depends on the Li generation rate and diffusion rate, thus the capacity is not dominated by the amount of materials only. Therefore, the slopes for capacity drop due to loss of contact area are smaller than 1, and the slope for lower C-rate (like 0.1 and 1 C) is larger than the higher C-rate when the cutoff voltage is 4.0 V. At higher rate, less diffusion time, the role of loss contact area will be more dominating, such the slope increases with increasing C rate.

The linear relationship may be due to the simplified 1D model and the assumption of worst scenario (losing accessible cathode material due to loss of contact), more sophisticated 2D and 3D models that can describe the local concentration change and the amount of accessible cathode material more accurately are being developed for further study. Nevertheless, the 1-D continuum model have directly correlated the loss of contact are with loss of capacity. So the next question if the loss of contact area can be recovered by the applied pressure, and how to calculate the necessary applied pressure. In the following part, calculations for the applied pressure would be discussed.

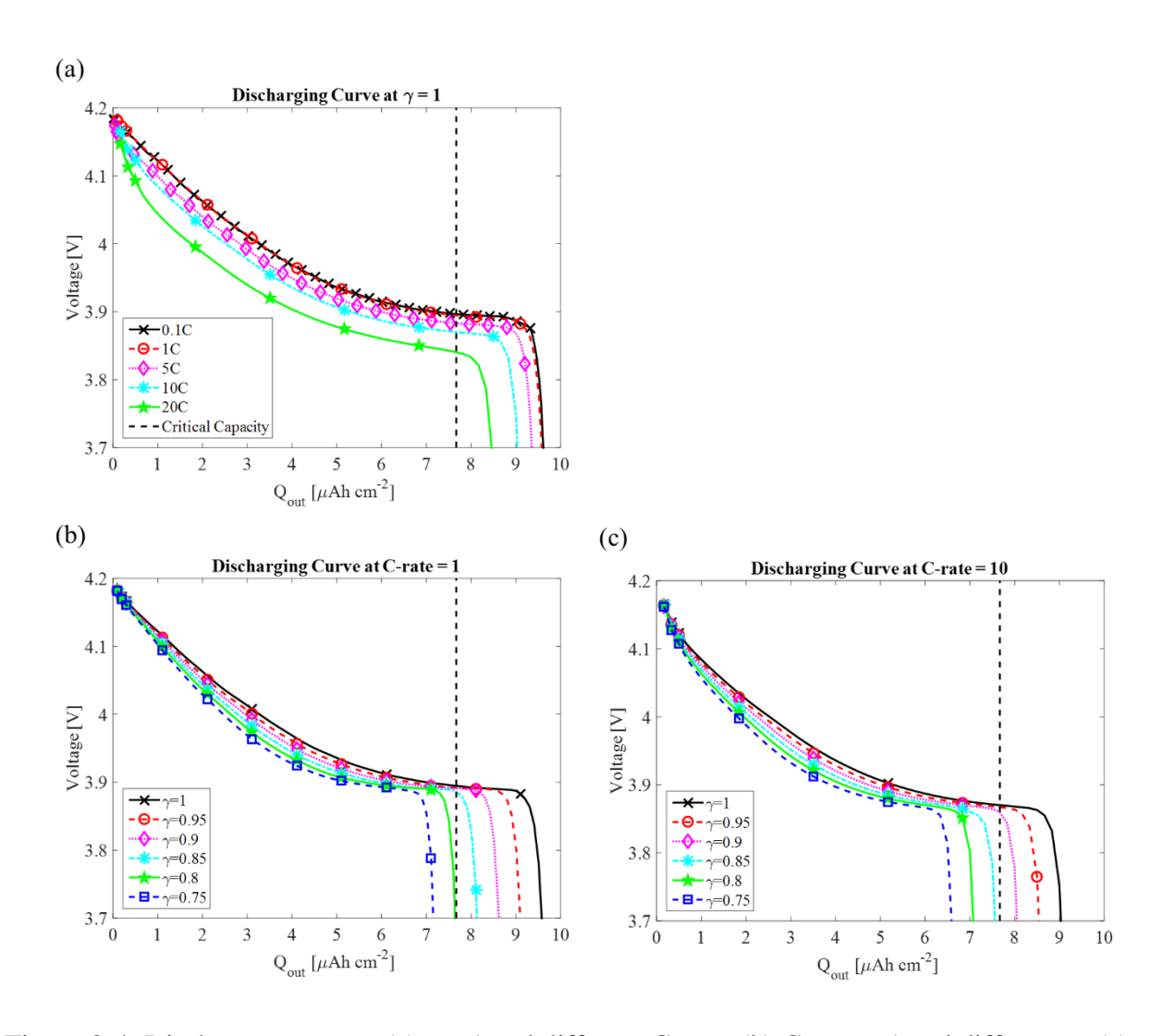


Figure 3-4. Discharge curves at (a) $\gamma = 1$ and different C-rate, (b) C-rate = 1 and different γ , (c) C-rate = 10 and different contact factor, γ .

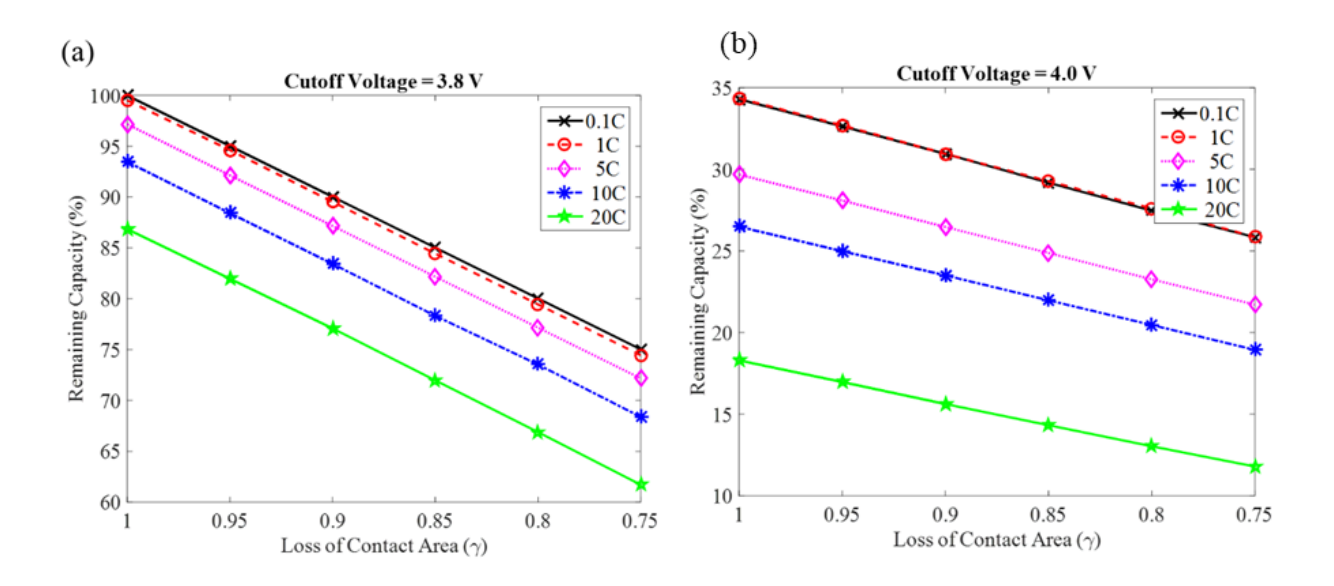


Figure 3-5. The relationship between the discharging capacity and the loss of contact area at cutoff voltage of (a) 3.8 V and (b) 4.0 V.

3.4.3. Estimation of needed pressure for recovering the loss of contact area

As introduced in section 3.3.3, for a given C(q), the contact area ratio, γ , can be calculated in different applied pressure, σ . Two all-solid-state batteries were considered, a film-type contact at $Li_3PO_4/LiCoO_2$ interface, and a bulk-type contact at $LGPS/TiS_2$, respectively. The previous battery discharge model is based on parameters fitted for the first case. It can be expected the predicted capacity loss due to contact area loss relationship is general for other all-solid-state batteries. In order to make a comparison with the experiments of Li et al. [76], the second case was modeled. As introduced in section 3.3.3 and plotted in Figure 3-2 (c), the initial C(q) has been determined based on measured RMS roughness for the thin film type and bulk-type and relationship between C(q) and RMS discussed by Flys et al. [279]. After cycling, experimental studies [286, 288, 290, 297] have reported the RMS roughness would increase. Also, based on the study of surface morphology [277, 278, 298], the absolute value of m, of the plot in Figure 3-2 (b) would increase,

and the intercept, I, would be decreased when the RMS roughness is increased. (m, I) values were changed to mimic the effect interface roughening due to battery cycling.

Figure 3-6 shows the surface contact ratio as a function of the applied pressure. As Figure 3-6 shows, at low applied pressure, the increase of contact area with the applied pressure is nearly linear, which agrees with other contact models, such as the theories of Hertz [299], Greenwood-Williamson [275], and Bush [276]. When the contact area ratio is greater than 60% (A/A $_0$ = 0.6), it would need much more pressure to increase the contact area further. The two black lines stand for the contact area before cycling, where m= -2.77, I=-11.35 for film-type battery in Figure 3-6 (a) and m= -3.08, I=-8.61 for the bulk-type batter in Figure 3-6 (b). Comparing the film-type and bulk-type all-solid-state batteries, at the same applied pressure the film-type has more contact area than the bulk-type. Both Figure 3-6 (a) and (b) show that with increasing surface roughness (increasing m and decreasing I) due to cycling, the contact ratio decreased. Furthermore, increasing the applied pressure can increase the contact ratio.

To demonstrate this model leads to reasonable contact area estimations, the results shown in Figure 3-6 (b) can be compared with the experiments by Li et al. [76], in which they investigate an In-Li/LGPS/TiS₂ all-solid-state Li-ion battery. They applied two different pressures, 19 and 230 MPa, for the fabrication process and during the operation of the battery. From the calculation, at 19 MPa, the contact area is only about 40%, which results in the poor capacity retention as shown in their experimental result. If increasing the pressure to 230 MPa, the contact area is estimated to be around 95%, and so they observed effectively enhanced capacity retention.

With this model, it is now possible to calculate the proper applied pressure for al-solid-state batteries. For example, if the initial condition for the film-type battery is under 20 MPa, as starting from point A in Figure 3-6 (a), the contact area is around 70%. After cycling, it may decrease to

point B, since the surface becomes much rougher, it also means around 20% of the contact area is lost. Then to get the original contact area and the capacity back, it needs to follow the pink line, for instance, increasing the contract pressure to 60 MPa will recover the contact area to 70% again. Therefore, based on Figure 3-5, the lost contact area can be estimated by the capacity drop. Then, based on Figure 3-6, the applied pressure needed to recover the contact area and capacity can be obtained. By connecting these two calculations, one could calculate how much contact area lost during cycling, and how much pressure should be applied to get the contact area back, to prevent the degradation of the all-solid-state Li-ion battery.

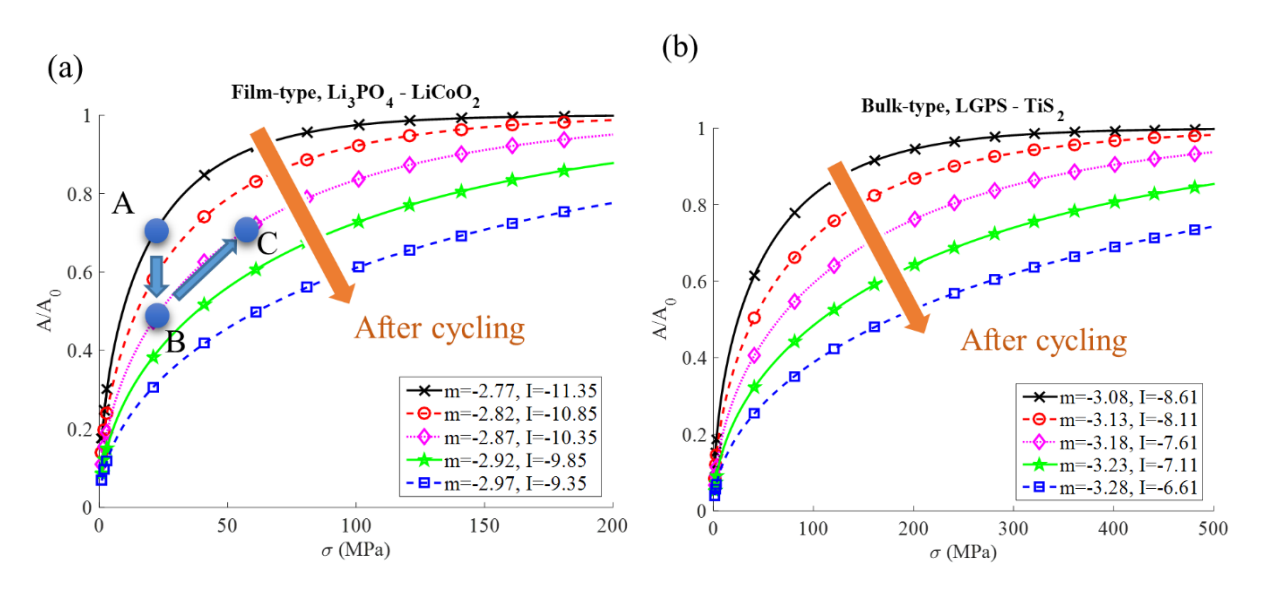


Figure 3-6. The relationship between the ratio of real contact area to the maximum contact area (A/A_0) and the applied external pressure (σ) for the interface of (a) film-type and (b) bulk-type battery.

3.5. Conclusion

The imperfect contact between the solid electrolyte and the electrodes is not only due to the fabrication process but also the operation of the battery. During cycling, the contact area would be decreased continuously because of the volume change of the electrodes, and it results in the degradation of the battery. To study the effect of the loss of contact area on the performance of the

battery, the imperfect contact is incorporated into a 1-D Newman battery model that simulates the discharging process of an all-solid-state battery. This model assumes the Li concentration will be localized at the reduced contact area, and it was solved by finite element analysis. It is found that the discharging voltage and capacity drop much faster due to loss of contact area at higher rate. The capacity drop was correlated with the contact area loss. At lower cutoff voltage (3.8V), the correlation is almost linear with a slope of 1; while at higher cut off voltage (4.0), the dropping rate is slower than 1 and the dropping rate decreases with increasing discharging rate.

To establish the relationship of the applied pressure and the contact area, Persson's contact mechanics theory was applied, as it uses self-affined surfaces to simplify the multi-length scale contacts in all-solid-state batteries. Taking measured surface roughness and elastic properties of solid electrolytes and electrodes, the contact area as a function of the applied pressure was calculated for film-type Li/Li₃PO₄/LiCoO₂ and bulk-type Li/LGPS/TiS₂ all-solid-state batteries. The results agree well with experimental observations of bulk type In-Li/LGPS/TiS₂ all-solid-state batteries. The model is further applied to suggest how much pressures should be applied to recover the contact area and capacity loss due to cycling.

One limitation of the current 1D model is that it assumes the loss of contact area leads to inaccessible positive electrode materials, which is the worst scenario. For future work, 2-D or 3-D continuum models need to be developed to capture the 2-D and 3-D diffusion of Li in the positive electrode after losing contact. The Li concentration gradient due to contact area loss will be calculated more accurately, thus the amount of lost material inside the electrode can be correlated with the contact area loss.

Another limitation of the current 1D model is that it inherited many assumptions and electrochemical equations derived in liquid electrolyte systems. These approximations may not

apply to all-solid-state batteries. For example, the ionic transport in solid and liquid electrolytes may be different. The ionic conductivity in solid electrolytes is carried by charged defects, such as vacancies or interstitials, whose concentration varies with the electrochemical Fermi level relative to the conduction and valance bands in the solid electrolyte [300]. Near the electrode surface, liquid electrolyte can form double-layer structure, however the solid electrolyte will be polarized. The difference in the double layer structure may lead to different charge transfer kinetics described by Butler-Volmer equations. These relationships need to be further developed and validated in all-solid-state batteries [18].

CHAPTER 4. Evaluation of the electrochemo-mechanically induced stress in all-solid-state Li-ion batteries

4.1. Summary

The mechanical degradation of all-solid-state Li-ion batteries (ASSLB) is expected to be more severe than that in traditional Li-ion batteries with liquid electrolytes due to the additional mechanical constraints imposed by the solid electrolyte on the deformation of electrodes. Cracks and fractures could occur both inside the solid electrolyte (SE) and at the SE/electrode interface. A coupled electrochemical-mechanical model was developed and solved by the Finite Element Method (FEM) to evaluate the stress development in ASSLB. Two sources of volume change, namely the expansion/shrinkage of electrodes due to lithium concentration change and the interphase formation at the SE/electrode interface due to the decomposition of SEs, were considered. The favorable SE decomposition reactions and the associated volume change were predicted by density functional theory calculations. It was found that the volume change due to SE-decomposition, and the resulting stress can be much more significant than the electrode volumetric change associated with Li insertion/extraction. This model can be used to design 3D ASSLB architectures to minimize the stress generation in ASSLB.

4.2. Introduction

Most Li-ion battery electrode materials experience volume changes during lithiation and de-lithiation. The Li compositional inhomogeneity causes stress, which is referred to as the "diffusion-induced stress" and leads to mechanical failure of electrodes during battery cycling. As the mechanical fractures and the structural disintegration result in battery capacity loss, models to predict the mechanical degradation of the electrodes were established and developed, either at the

single-particle level or the electrode composite level, especially in the past decade for traditional Li-ion batteries [222, 301-312]. With the increasing interest in ASSLB [313-317] owing to their improved endurance and safety, mechanical degradation in ASSLB becomes a critical and unsolved issue that impacts the performance and life of ASSLBs [31].

The mechanical degradation of ASSLBs is expected to be more severe than that of traditional Li-ion batteries, since the solid electrolyte, unlike the mechanically compliant liquid electrolyte, imposes additional mechanical constraints on the deformation of electrodes. Indeed, cracks have been observed in the solid electrolytes and at the electrode/electrolyte interfaces in ASSLBs. For example, cracks and fractures were found across the $\text{Li}_{1+x}\text{Al}_x\text{Ge}_{2-x}(\text{PO}_4)_3$ (LAGP) solid electrolyte (SE) during electrochemical cycling of symmetric Li/LAGP/Li coin cells caused by the growth of the interphase [42]. The LAGP/Li metal interface was also found to undergo amorphization and volume expansion in a symmetric Li/LAGP/Li coin cell, which causes fracture of the SE along with a massive increase in impedance [38, 105]. Interface delamination of $\text{LiNi}_{1-x-y}\text{Co}_x\text{Mn}_y\text{O}_2$ (NMC) electrode from $\beta\text{-Li}_3\text{PS}_4$ SE in a composite positive electrode was observed during charging, as the interfacial decomposition of the sulfide SE and the contraction of NMC [318] causes a loss of interfacial contact and results in capacity loss [76, 187]. Despite its importance, a modeling framework to evaluate the coupled electrochemical-mechanical stress generation has not been fully established for ASSLBs.

Various sources of chemical strains and the mechanical constraints imposed by the solidstate architecture contribute to the stress generation in ASSLBs. Solid electrolytes, especially those based on stiff ceramics, form non-perfect contacts at the interfaces with the electrodes in ASSLBs, causing non-uniform local stress [187]. Chemical strain due to Li concentration-induced volume changes on one or both sides of the electrode/SE interface will directly lead to stress generation. Several numerical studies have tackled this source of chemical strain and its impact on the crack propagation in electrode-SE composite, electrode/SE interface delamination [167, 188], and damages of the electrodes [304]. The stress generation in ASSLBs is further complicated by the interphase layer that forms due to the electrode and solid electrolyte chemical reactions. Earlier reports claimed improved electrochemical stability for SEs compared to liquid electrolytes based on cyclic voltammetry (CV) measurements [19, 205, 319, 320]. However, it was later revealed that many promising SEs decompose via reduction/oxidation [24, 25], forming an interphase layer at the electrode/SE interface. The interphase formation is accompanied by a volume change at the SE/electrode interface. As we shall show in this paper, this source of chemical strain can lead to higher stress generation. The mechanical constraints highly depend on ASSLB architectures [113]. It is expected that the stress distribution will be different in 2D thin-film batteries that have planar geometries [16], in 2.5D batteries with one planar and one needle-like structure [85], and 3D batteries with fully interdigitated electrodes and SEs architectures [82-84].

The primary goal of this paper is to develop a general continuum modeling framework to evaluate the stress generation caused by the volume changes in electrodes due to electrochemical reactions and in the interphase layer due to the decomposition of solid electrolyte in ASSLBs with nanoscale architectures, as shown in Figure 4-1. The continuum model takes inputs from both experiments and first-principles calculations. In this paper, the volume change due to the decomposition of the SE is obtained by assuming the products of the most energetically favorable reaction at Li chemical potential [24, 25]. These reaction energetics and volume changes can be calculated based on density functional theory (DFT) calculations. One architecture and two boundary conditions are used to mimic the geometry and constraints in a 2.5D nanostructured ASSLB deposited by Talin *et al.* [85]. The 2.5D ASSLB was fabricated by sputtering LiCoO₂ positive electrode on substrates

of conical micro-columns, followed by sputter-coating a Lithium Phosphorous Oxynitride (LiPON) electrolyte and depositing a thin film Si negative electrode. This battery geometry was motivated to reduce the Li diffusion length within the cathode and anode electrodes and to be a while increasing areal energy density. The electrochemical performance of this 2.5D battery has been investigated by both experiments and continuum modeling, but the stress generation in this architecture has not been addressed yet. The stress distribution is expected to be highly inhomogeneous across the 2.5D conical geometry, thus causing fractures in specific regions associated with stress concentration. Furthermore the observed voids in between the microcolumns additionally impact the stress generation. This model can be easily adapted for evaluating various electrode/SE materials 3D ASSLB geometries.

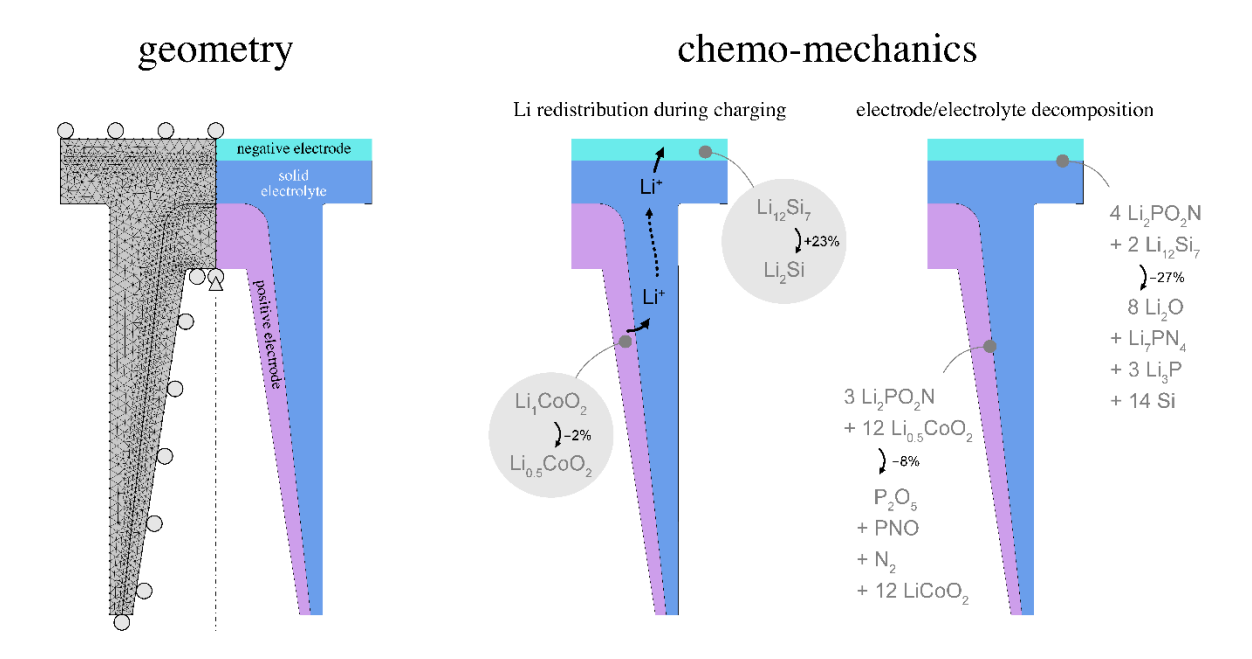


Figure 4-1. A schematic that shows the whole idea in this work, a chemo-mechanical model that includes the volume change and resulting stress from the lithiation/de-lithiation and the SEI formation.

4.3. Computation methods

All stress calculations and the charging of the batteries were carried out at the continuum level using the commercially available COMSOL Multiphysics software version 5.4. The

distribution of the first principal stress in the ASSLB was used as a metric to determine the location of possible crack propagation and failures based on the maximum stress that can be generated.

4.3.1. Battery Architecture

Figure 4-2 (a) and (b) show the 2.5D nanostructured ASSLB consisting of Si electrode, LiCoO₂ (LCO) positive electrode, and LiPON solid electrolyte. The 2.5D geometry was built from a 360⁰ rotation of a 2D plane around the center axis and mimics the geometry of a 2.5D battery that was deposited and characterized through Scanning Electron Microscopy (SEM) [85], as shown in Figure 4-2 (c). Note that in the experiments, the 2.5D nanostructured ASSLB is not fully dense. Voids between the LiPON phases were observed [85], but their sizes are not well characterized. Therefore, two boundary conditions were adopted to study the effect of the voids, namely the free-side and fix-side boundary conditions, as labeled with green lines in Figure 4-2 (a). The boundaries with blue color in Figure 4-2 (a) are the axis center of the battery and the interfaces between electrodes and the current collector, which are set to be fixed in this model, and the internal boundaries of the interphase layers in the LiPON electrolytes have matching nodes at the interface to simulate a well-bonded interface formed by a Chemical Vapor Deposition (CVD) process.

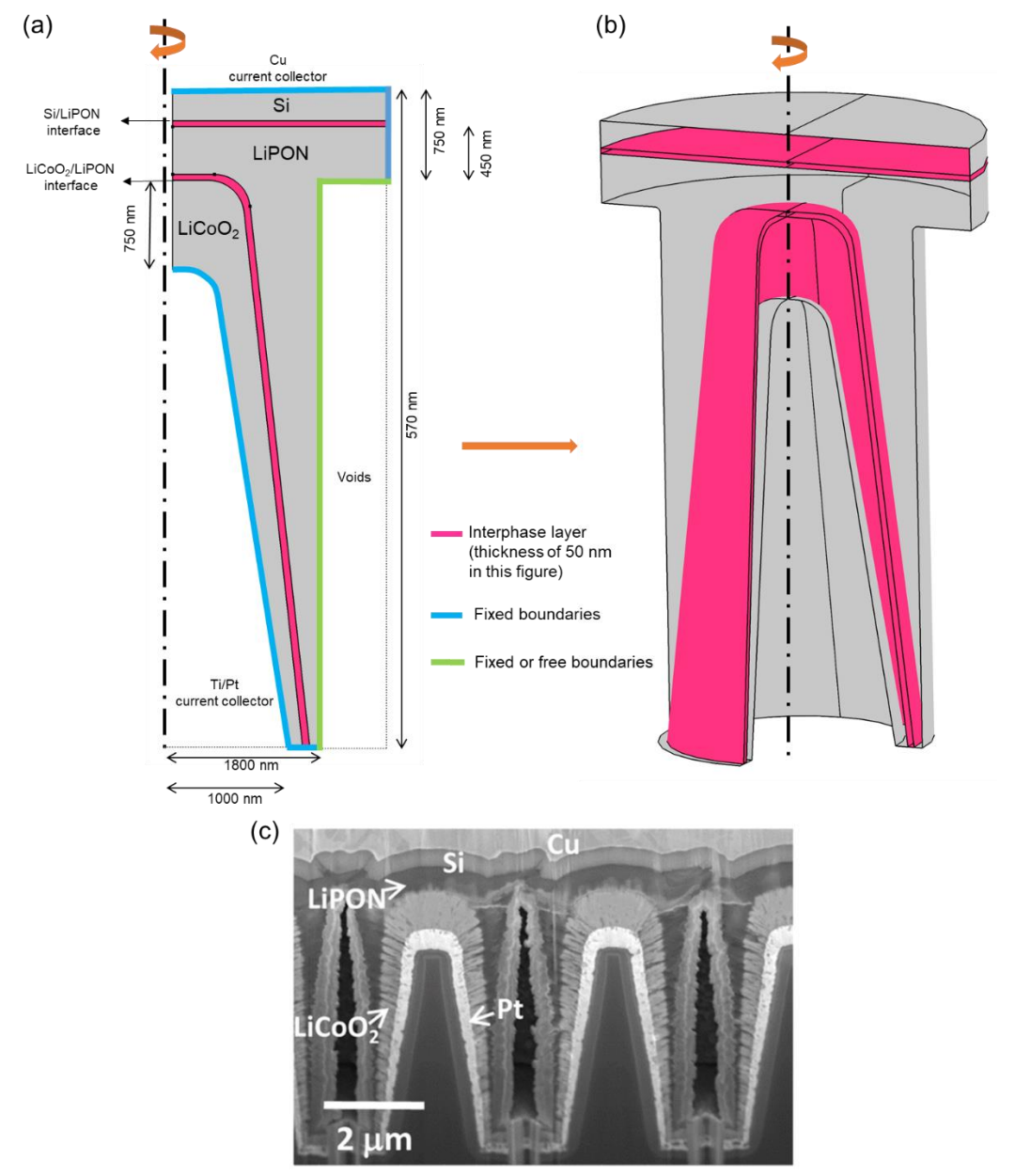


Figure 4-2. 2D plane geometry (a) that is rotated around the y-axis to result in the full 3D battery geometry. (b) The electrochemical reactions occur at the two interfaces that are labeled in (a). (c) SEM cross-section image of 2.5D ASSLB [85].

4.3.2. Volume change induced by Li concentration gradient during charging

To obtain the volume change as a linear function of Li concentration in the electrodes, the Li concentration variation during the battery charging process was first calculated based on the Newman model [157, 321] of Li-atom diffusion in both electrodes, Li-ion migration and diffusion in the solid electrolyte, and the charge transfer reactions at the electrode/electrolyte interfaces. The

interphase layers were not explicitly modeled in this simulation as their impact on interface impedance was ignored at the moment.

In the positive LCO electrode and the negative Si electrode, the diffusion of Li atoms was described by Fick's law of diffusion [322]:

$$\frac{\partial c_{Li}}{\partial t} + \nabla(-D_{Li}\nabla C_{Li}) = 0$$
 Eq. 4-1,

where C_{Li} is the local concentration of Li in electrodes, and D_{Li} is the diffusion coefficient of Li. The diffusion of Li is isotropic in Li_xSi and anisotropic in Li_yCoO₂ as reported previously [85]. In the latter, Li diffuses laterally along the LCO surface faster than normal to LCO surface.

In the LiPON SE, since both concentration and electrostatic potential gradient exist, the transport of Li ions was described by the Nernst–Planck equation [323]:

$$\frac{\partial C_i}{\partial t} + \nabla \left(-D_i \nabla C_i - Z_i \frac{D_i}{RT} F C_i \nabla \varphi_{electrolyte} \right) = 0$$
 Eq. 4-2,

where C_i is the concentration of species i (including Li-ion and negative charges [94, 187]), D_i is the diffusion coefficient of species i, $\varphi_{electrolyte}$ is the solution potential, Z_i is the charge of species i, R is the gas constant, T is the absolute temperature, and F is the Faraday constant. To maintain charge neutrality in the solid electrolyte, the following equation was implemented everywhere in the electrolyte:

$$\sum Z_i C_i = 0$$
 Eq. 4-3.

The charge transfer reactions at SE/electrode interfaces were described by Butler–Volmer kinetics [324]. All the following variables with subscript "electrode" have a different value for the positive (LCO) and negative (Si) electrode, as listed in Table 4-3.

The current per area (unit: Ampere/m²), *i_{electrode}*, is expressed as:

$$i_{electrode} = i_{electrode}^{0} \left[e^{-\alpha_{electrode} \frac{F}{RT} \eta} - e^{(1-\alpha_{electrode}) \frac{F}{RT} \eta} \right]$$
 Eq. 4-4,

where $i_{electrode}^{0}$ is the exchange current density at the electrode, which is the current at equilibrium and can be defined as:

$$i_{electrode}^{0} = Fk_{electrode} \left[\frac{\left(c_{Li_max} - c_{Li} \right) c_{Li^{+}}}{\left(c_{Li_max} - c_{Li_min} \right) c_{Li^{+}}^{0}} \right]^{\alpha} \times \left[\frac{c_{Li}}{c_{Li_max}} \right]^{1-\alpha}$$
Eq. 4-5,

 α is the charge transfer coefficient, $k_{electrode}$ is a kinetic constant. C_{Li_max} and C_{Li_min} are the maximum and minimum Li concentration in the electrode, respectively. C_{Li} is the Li ion concentration in the SE, and C_{Li}^0 is the initial concentration of Li ions in the SE, these are the mobile Li ions, which is around 20% of the total Li concentration in LiPON electrolyte [94]. η is the overpotential at the SE/electrode interface that is described as:

$$\eta = \varphi_{electrode} - \varphi_{electrolyte} - E_{electrode}$$
Eq. 4-6,

where φ is the electric potential and $E_{electrode}$ is the equilibrium potential of the electrode. The equilibrium potentials at the negative and positive electrodes, $E_{negative}$ and $E_{positive}$, were obtained from the previously fitted numerical functions [325], the Eq. 4-14 and Eq. 4-15 in Appendix. $\varphi_{electrolyte}$ at the negative electrode was set to zero.

A constant current charge/discharge process requires that the total current, I_{total} (unit: Ampere), passing through the negative electrode/electrolyte interface and the positive electrode/electrolyte interface (as labeled in Figure 4-2) are equal, as

$$I_{total} = \int_{Area_{(negative_electrode/electrolyte)}} i_{negative} = \int_{Area_{(positive_electrode/electrolyte)}} i_{positive}$$
 Eq. 4-7

Note that this boundary condition implies that the reaction rate and Li concentration is not uniform over the electrode surface. All the other surfaces were described as no-flux.

This simulation solved the time-dependent Li concentration profile in the ASSLB during the charging process, followed by the steady-state simulation, which means the time-independent

simulation, to calculate the stress caused by the local Li concentration variation, ΔC_{Li} , in the electrodes. The induced stress from the non-uniform chemical strain due to the inhomogeneous C_{Li} was considered to occur instantly [306]. Assume a linear interoperation for the volume change within the range of Li concentration in the electrodes as:

$$\Delta V_{Li} = a_v \Delta C_{Li}$$
 Eq. 4-8,

where ΔV_{Li} is the volume change (%) due to the change of Li local concentration during lithiation and de-lithiation, a_v is the volume expansion coefficient, which is defined as the volume change of the electrode normalized by the range of concentration change. The volume change of LiPON electrolyte due to Li concentration change is not included in this model, because as it will be shown later that the overall change in Li ion concentration during charging process is only around 5% of the total Li-ion concentration in the LiPON electrolyte, so the volume change is minimal compared to the electrodes.

4.3.3. Volume change induced by the decomposition of solid electrolyte

The volume change of the two interphase layers was calculated based on the decomposition products that were the stable phases at the Li chemical potential, which was related to the electrode potential. The equilibrium phases were obtained from the grand potential phase diagram introduced in [24, 25]. The corresponding decomposition reactions were obtained from the DFT-computed database in Material Project [326] through its Application Programming Interface (API) [327]. In this study, we selected $\text{Li}_2\text{PO}_2\text{N}$ to represent LiPON, since it has been reported that the thin-film LiPON synthesized through Atomic Layer Deposition (ALD) is characterized as $\text{Li}_2\text{PO}_2\text{N}$ [192, 193]. Considering the equilibrium potential of Li_xSi (x = 0 – 4) and Li_yCoO_2 (y = 0.5 – 1) during cycling is in the range of 0 – 0.6 V and 2.5 – 4.2 V vs. Li chemical potential, respectively, different reaction routes and products correspond to different Li chemical potentials

as shown in Table 4-1. The unit volume of each solid compound was obtained from the database of Material Project. The volume change for the decomposition reaction is defined as

$$\Delta V_d = \frac{V_2 - V_1}{V_1}$$
 Eq. 4-9,

where V_1 and V_2 are the total volume of all reactants and products in the decomposition reaction, respectively.

Note that the two interphase layers are still in the solid-electrolyte region (i.e., having the properties of the electrolyte), as Figure 4-2 (a) shows. Two different interphase layer thicknesses of 10 nm and 50 nm were chosen for this model based on the typical thickness of Solid Electrolyte Interphase (SEI) in the range of 10-100 nm [328, 329].

4.3.4. Stress induced by the volume change from different sources

Assuming the volume change is isotropic, the chemical strain is

$$\varepsilon_c = \sqrt[3]{\Delta V + 1} - 1 \approx \frac{1}{3} \Delta V$$
 Eq. 4-10,

where ε_c is the chemical strain that can be caused by the lithiation/de-lithiation of electrodes or the decomposition of solid electrolyte. ΔV is the volume change as either the ΔV_c and ΔV_d are computed from Eq.1 and Eq. 9, respectively. Assuming linear isotropic elastic deformation, the induced stress can be calculated based on the continuum equilibrium conditions:

$$\nabla \cdot \boldsymbol{\sigma} = 0$$
 Eq. 4-11,

$$\sigma = \mathbf{C} : \varepsilon_{el} = \mathbf{C} : (\varepsilon - \varepsilon_{\mathbf{C}})$$
 Eq. 4-12,

$$\boldsymbol{\varepsilon} = \frac{1}{2} [\boldsymbol{\nabla} \boldsymbol{u} + (\boldsymbol{\nabla} \boldsymbol{u})^T]$$
 Eq. 4-13,

where σ is the stress tensor, ε is the total strain tensor, ε_{el} is the elastic strain tensor, u is the displacement vector, and c is the fourth-order elasticity tensor that is a function of Young's modulus and Poisson's ratio.

The mechanical properties of different materials and the parameters used in this model are listed in Table 4-3 in the Appendix.

4.4. Results and discussion

4.4.1. Stress due to Li composition gradient during Charging

It is well known the chemical strains due to Li concentration induced volume changes in the electrode will directly lead to stress generation. The lithium concentration in the electrode particles was first obtained by simulating the charging process of the 2.5D nanostructured ASSLB. The charging curve is shown in Figure 4-3, different C-rates (1.2C, 0.6C, and 0.16C) were selected for testing in order to compare with the previous experiments. The voltage of the battery was calculated by $\varphi_{cathode} - \varphi_{anode}$, which were obtained from Eq. 4-6. The simulated charging curve and the charging capacities at 4V in this study: 3.8, 9.2, and 22 μ Ah/cm², are in good agreement with the experimental results [85], which also validates the parameters used in this model. The discharge curves (not shown) also agree with the experiments.

The volume change within the concentration range in Li_xSi electrode and Li_yCoO₂ electrode was obtained from the previous computational study [222]. Si shows 263% volume expansion from when its composition changes from Si to Li_{3.75}Si. LiCoO₂ shows a 2% volume increase when its Li ratio changes from 0.5 to 1. Assume a linear relationship between the volume change and Li concentration, as shown in Eq. 4-8, the value of the a_v for Si and LCO electrodes are listed in Table 4-3 in the Appendix. Although some research has considered the volume change in the solid-electrolyte due to Li concentration change, for this study, the deviation of mobile Li concentration in LiPON was found to be little (~5% in total Li concentration) while charging, so the chemical strain in LiPON electrolyte was not included. As shown in Figure 4-4, the variation of Li-ion

concentration in LiPON electrolyte is around $5x10^3$ mol/m³, while the total Li-ion concentration is $1x10^5$ mol/m³, as only 20% of the total Li-ions are mobile in LiPON electrolyte [94].

The Li concentration profile at different charging time is shown in Figure 4-4, the direction of arrows stands for the flux direction of Li-ions in LiPON electrolyte. The charging process stops when the 'x' of Li_xSi at any point of the Si electrode surface reaches 3.75 or when the 'y' of Li_yCoO₂ at any point of the LCO electrode surface hits 0.5. These constraints imply no phase change nor diffusion coefficient change during the cycling simulation. As Figure 4 shows, when the charging process stops (~480 s), only a thin layer of Li is consumed from the Li_yCoO₂, and the same as in Li_xSi that only the surface layer got lithiated. The variation of Li ratio in Li_xSi and Li_yCoO₂ during the whole charging process are x = 1.68 - 2 and y = 1 - 0.5, respectively.

The charging results revealed that only a small portion of Li in Li_yCoO₂ was used (released to LiPON electrolyte), which is due to the short distance between the top of LCO electrode and Si electrode surface. This makes the Li concentration on the top of LCO electrode reduce more than the bottom of the LCO electrode, thus the battery voltage increase quickly and the capacity is poor.

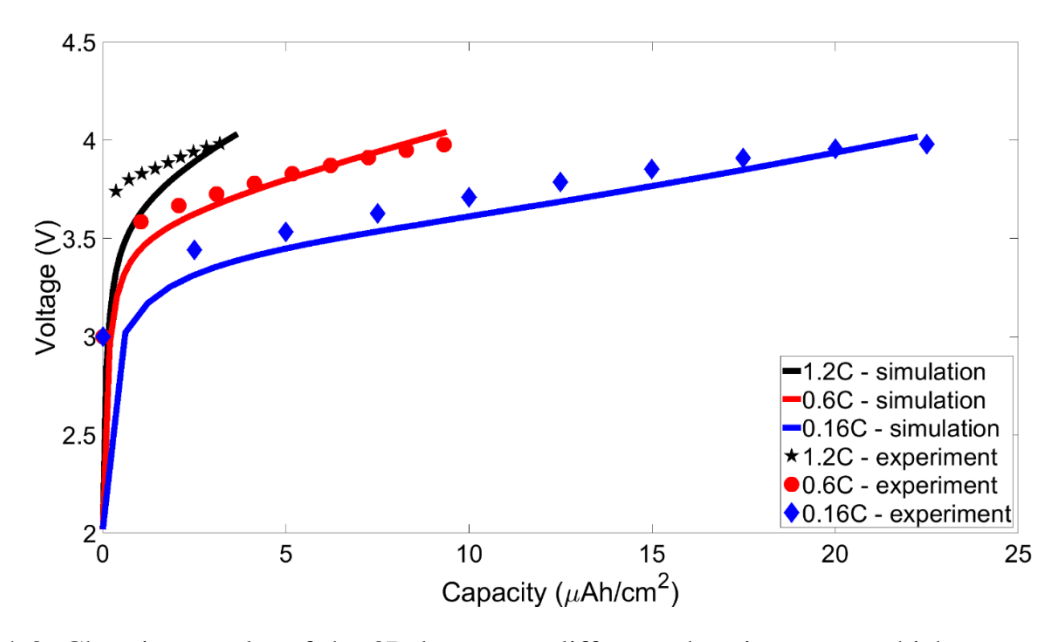


Figure 4-3. Charging results of the 3D battery at different charging rates, which are to compare with experimental results [85].

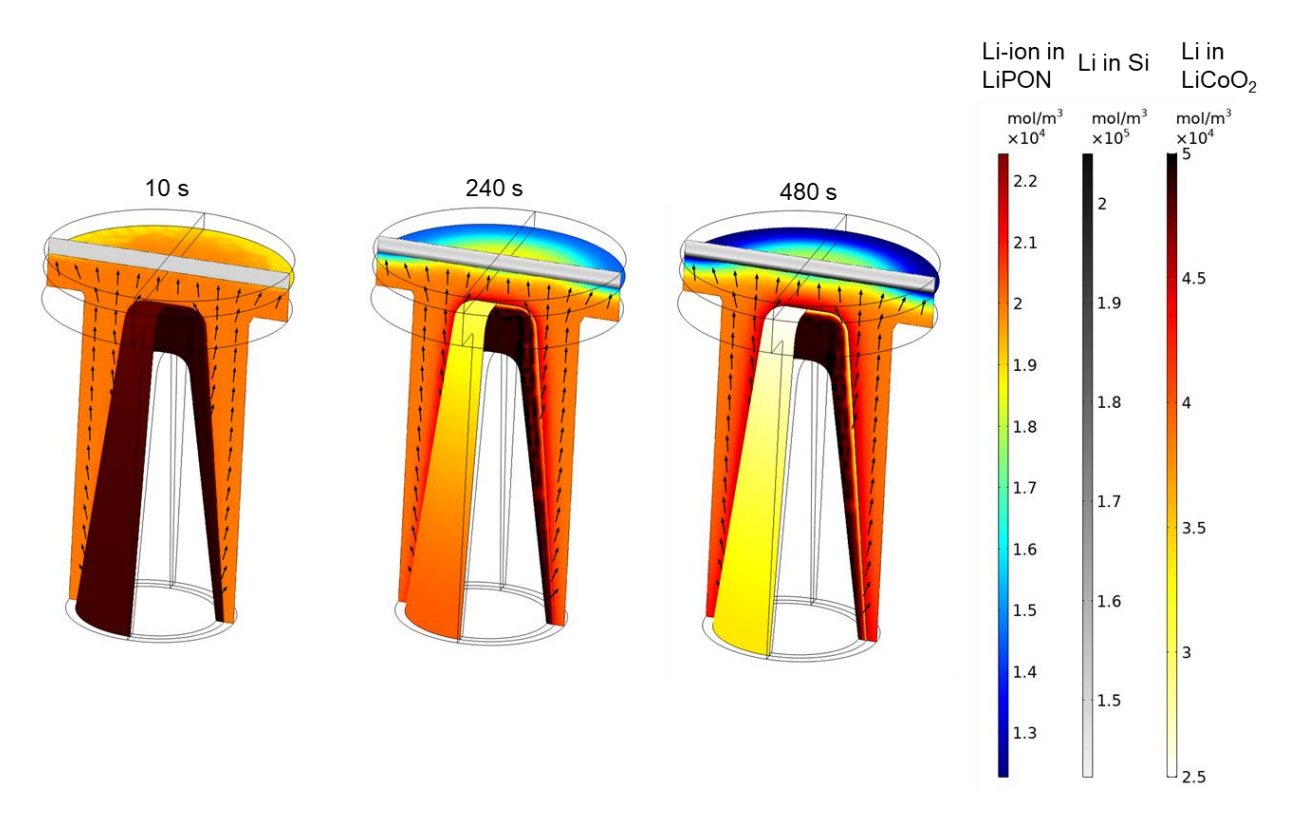


Figure 4-4. Li concentration profile at different charging time at 1.2 C. The arrows in LiPON electrolyte represent the transport direction of Li-ions.

From the Li concentration profile at different time, the induced-stress from the expansion/shrinking of electrodes can be calculated, as shown in Figure 4-5. The stress distribution results show that a thin layer of LCO electrode surface is under tensile stress while the surrounding area is under the compressive state of stress. This is due to the stripping of Li from the LCO surface that causes the volume reduction and the stress being tensile. The LiPON electrolyte is mostly under compressive stress, so not much of cracks are expected. On the other side, there is much more severe tensile stress generated in Si electrode except for the surface layer. Since the volume change of Si electrode is more significant (84.2% increase from 1.68 to 2 of Li ratio in Li_xSi) than that of in LCO (2% increase from 0.5 to 1 of Li ratio in Li_yCoO₂), higher stresses are induced in Si electrode even though the Young's modulus of LCO is higher as compared to Si. The thin layer under compressive stress on the Si negative electrode surface is due to the expansion that tries to

push out the surrounding area. Another noticeable difference between the fixed and free side conditions lies at the stress distribution on the top of LiPON electrolyte near the Si electrode. A more considerable tensile stress formed in free side case than fixed side case, which is opposite to the stress distribution of the decomposition of LiPON electrolyte that was introduced earlier. This is due to the fact that Si is expanding during charging, in which if there are voids on the side, the side area would be pushed away by Si negative electrode and resulting in large tensile stress. However, if there are no voids, and the side surfaces are constrained, the expansion of Si negative electrode would make this area more compressive. Therefore, in this specific condition (charging batteries of Si electrode and LCO electrode), the cracks are more likely to propagate in Si electrode and the top side of LiPON, if there are voids on the side.

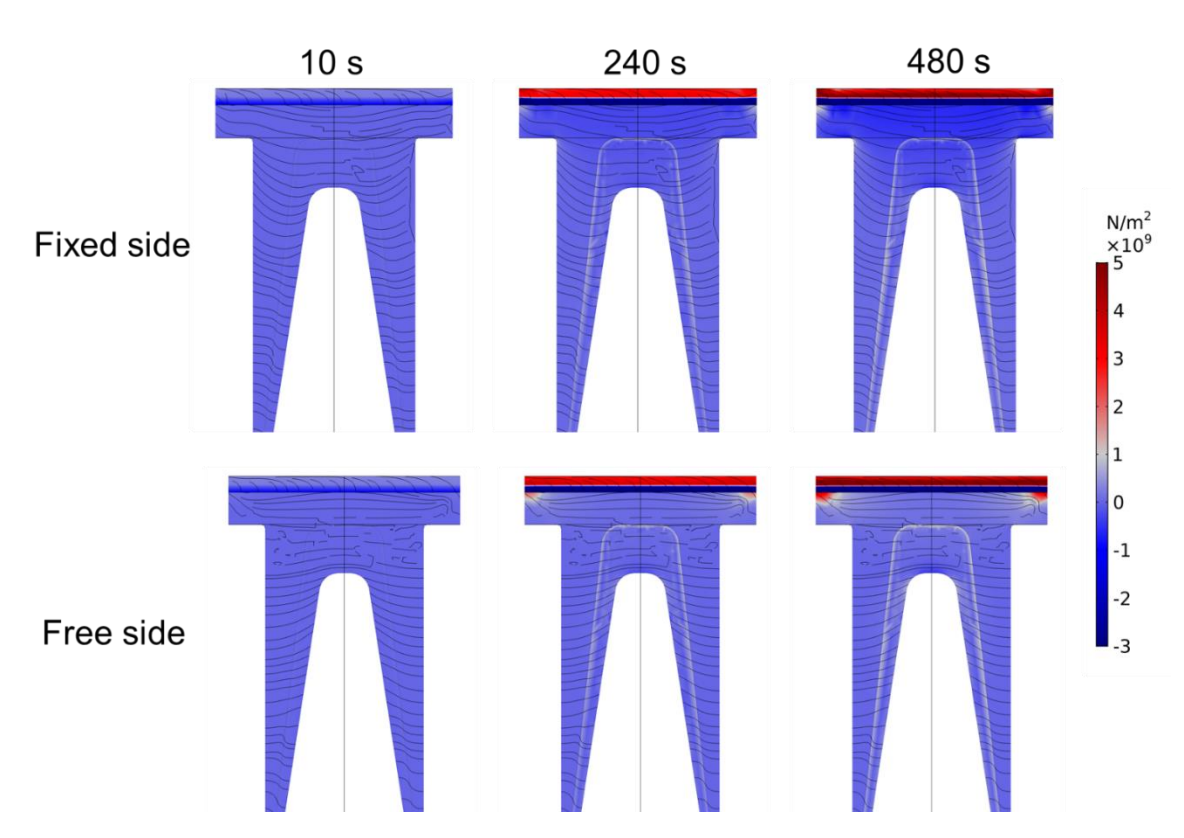


Figure 4-5. Induced first principal stress during charging process for two different cases. The lines represent the direction of the stress. Positive and negative stress mean the tensile and compressive stress, respectively.

4.4.2. Strain due to the Solid Electrolyte Decomposition

Table 4-1 lists the thermodynamically favored LiPON decomposition reactions and the corresponding molar volume change based on the DFT computed data collected in Materials Project. Note that these are full reactions from the oxidation/reduction of the electrodes and electrolyte.

At the Li₂PO₂N /Si interface, as Si becomes lithiated, the Li chemical potential drops with increasing x in Li_xSi. So Li₂PO₂N decomposition reaction varies respect to the electrode potential, as Si becomes LiSi, Li₁₂Si₇, Li₇Si₃, Li₁₃Si₄, and Li₂₁Si₅ [330, 331]. In this study, we focused on the "worst" cases within the range of Li ratio variation, as it is associated with the most significant volume changes of -27% at the Li₂PO₂N/Si interface, which occurs at the potential of Li₁₂Si₇. Based on the simulation of the charging process that will be discussed later, the Li ratio varies from Li_{1.68}Si to Li₂Si, suggesting this worst case will be reached experimentally.

At the $\text{Li}_2\text{PO}_2\text{N/LCO}$ interface, $\text{Li}_2\text{PO}_2\text{N}$ is oxidized by Li_yCoO_2 and gas generation was predicted. In fact, bubbles (O₂ or N₂) formation has been found in the LiPON SE after applying high voltage in experiments [320]. In this study, the volume of N₂ was excluded in the molar volume change, as gas may diffuse out. At the voltage above 3.63V, the most significant volume change is -8% at the $\text{Li}_2\text{PO}_2\text{N/Li}_{0.5}\text{CoO}_2$ interfaces.

Therefore, on both the positive electrode side (Li_yCoO₂) and the negative electrode side (Li_xSi), the volumes of the interphase layer shrink. So, the corresponding linear strain due to the decomposition of Li₂PO₂N at the negative Si and positive LCO electrode side is -8.3% and -2%, respectively, based on Eq. 4-10, which was given as an input to the simulation of stress development. Then the corresponding stresses due to these strains were then analyzed.

Table 4-1. Grand potential equilibrium phases of Li₂PO₂N.

	Li chemical potential	Corresponding reaction	Volume change
Against Li _x Si	0-0.01 V	$21\ \text{Li}_2\text{PO}_2\text{N} + 8\ \text{Li}_{21}\text{Si}_5 -> 42\ \text{Li}_2\text{O} + 21\ \text{Li}_3\text{N} + 21\ \text{Li}_3\text{P} + 40\ \text{Si}$	-19%
	0.01-0.53 V	$52 \text{ Li}_2\text{PO}_2\text{N} + 24 \text{ Li}_{13}\text{Si}_4 -> 104 \text{ Li}_2\text{O} + 13 \text{ Li}_7\text{PN}_4 + 39 \text{ Li}_3\text{P} + 96 \text{ Si}$	-24%
		$28 \text{ Li}_2\text{PO}_2\text{N} + 24 \text{ Li}_7\text{Si}_3 -> 56 \text{ Li}_2\text{O} + 7 \text{ Li}_7\text{PN}_4 + 21 \text{ Li}_3\text{P} + 72 \text{ Si}$	-23%
		$4 \text{ Li}_2\text{PO}_2\text{N} + 2 \text{ Li}_{12}\text{Si}_7 -> 8 \text{ Li}_2\text{O} + \text{Li}_7\text{PN}_4 + 3 \text{ Li}_3\text{P} + 14 \text{ Si}$	-27%
		$4 \text{ Li}_2\text{PO}_2\text{N} + 24 \text{ LiSi} \rightarrow 8 \text{ Li}_2\text{O} + \text{Li}_7\text{PN}_4 + 3 \text{ Li}_3\text{P} + 24 \text{ Si}$	-29%
	0.53-0.65 V	$6\ Li_{2}PO_{2}N+32\ LiSi_{3} \ -> \ Li_{14}P_{2}(N_{2}O)_{3}+9\ Li_{2}O+4\ Li_{3}P+96\ Si$	-22%
Against Li _y CoO ₂	2.64–3.04 V	$7 \text{ Li}_2 PO_2 N + 24 \text{ Li}_{0.75} CoO_2 \rightarrow 2 \text{ Li}_4 P_2 O_7 + P_3 N_5 + \frac{N_2}{2} + 24 \text{ Li} CoO_2$	-2%
	> 3.63 V	$3 \text{ Li}_2 PO_2 N + 12 \text{ Li}_{0.5} CoO_2 \rightarrow P_2 O_5 + PNO + N_2 + 12 \text{ Li}_{0.5} CoO_2$	-8%

4.4.3. Stress due to the Solid Electrolyte Decomposition

Figure 4-6 shows the corresponding first principal stress generated due to the decomposition of solid electrolyte and the associated formation of the interphase layer. On the plane through the rotating axis at the center, the positive stress means "tension" and the negative means "compression", and lines represent the direction of the first principal stress. Table 4-2 collects the maximum first principal stress in different domains and boundary conditions. Note that it only shows the value of tensile stress (positive) since those are responsible for crack initiation and propagation [188].

From the results shown in Figure 4-6, the volume shrinkage due to the interphase formation causes tensile stress in the most part of the ASSLB. The magnitude of the stress and the region with high stress (higher than 1GPa) increases with the thickness of the interphase layer. For an interphase layer of 10 nm, lower stresses are generated, while for the 50 nm thick interphase layer, it is observed that most regions are under significantly higher stresses. As shown in Table 4-2, the maximum first principal tensile stress in Si electrode and the SE are much higher than that in the LCO electrode.

The voids seen in the 2.5D nanostructured ASSLB had a large impact on the stress development. The stress generated by the same 50 nm interphase layer formation but under different boundary conditions, fixed and free void side, shows different distributions. The former seems to cause the top region under high tensile stress while the later has a less stressed area on the sides. Without the constraint from the side surfaces, the induced stress in LCO electrode seems to point to the normal direction to the LCO electrode surface, while the stress in LCO electrode for the latter case is mostly towards the Si electrode. As shown in Table 4-2, the highest stress occurs in the SE is under fixed side condition, which is as high as ~27 GPa. However, if there are voids on the side (free side condition), the maximum stress drops significantly from 26.8 to 4.79 GPa in the SE and from 14.68 to 7.68 GPa in the Si electrode.

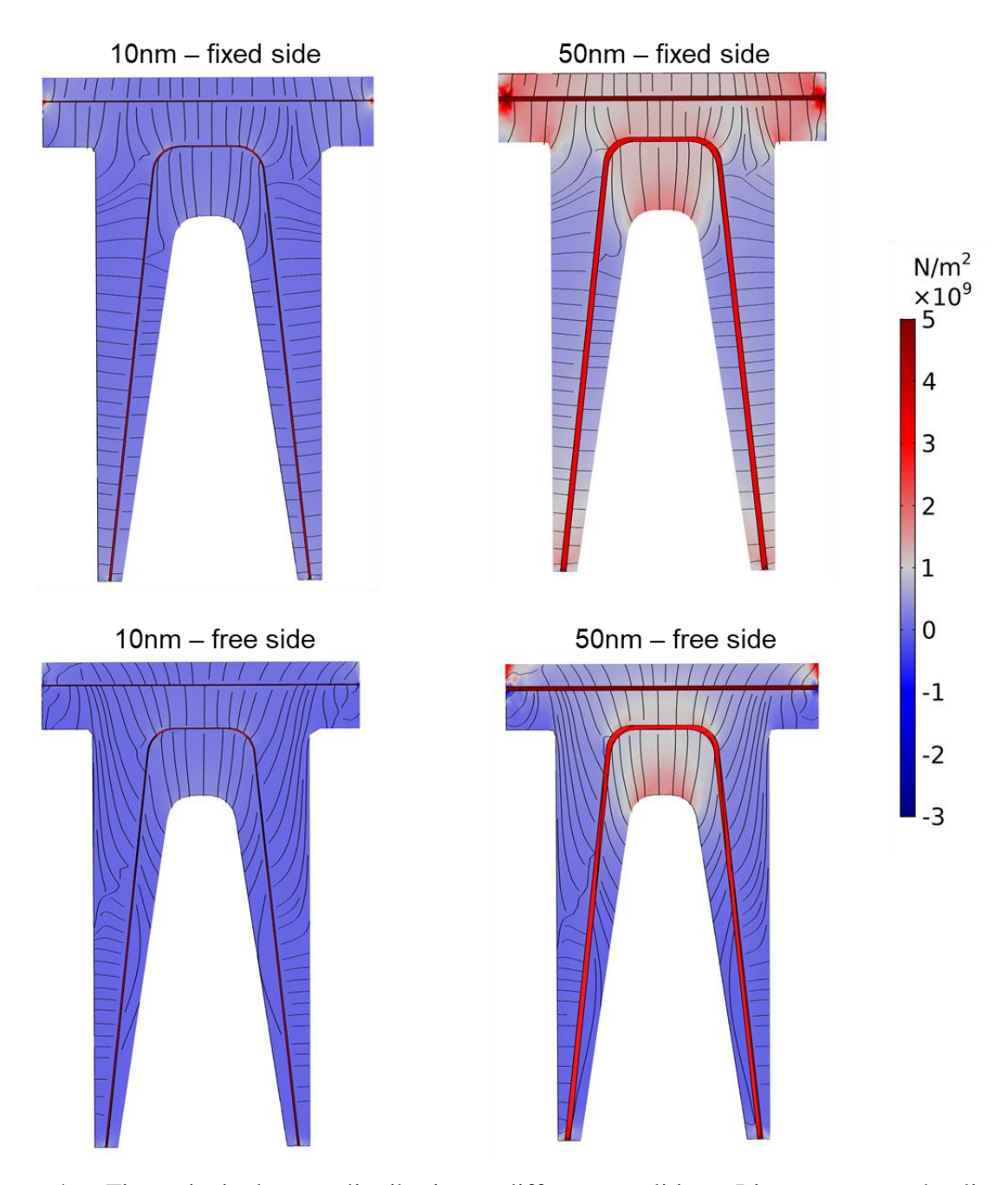


Figure 4-6. First principal stress distribution at different conditions. Lines represent the direction of the stress. Positive and negative stress mean the tensile and compressive stress, respectively.

Table 4-2. The maximum first principal stress in different domains and boundary conditions.

Maximum first principal stress (GPa)		Interphase layer thickness	
		50 nm	10 nm
	Si electrode	14.68	12.59
Fixed side	LCO electrode	3.64	1.82
	LiPON electrolyte	26.80	9.90
	Si electrode	7.68	4.29
Free side	LCO electrode	2.82	1.68
	LiPON electrolyte	4.79	3.76

The simulated stress induced by the interphase layer formation reveals the importance of the thickness of interphase layers and the presence of voids in the 2.5D nanostructured solid-state batteries; the thickness of the interphase layer decides how large the region is affected by the decomposition: with 10 nm decomposition layer showing not much of an influence, while the stresses for a 50 nm thickness could be as high as ~27 GPa, as observed in the LiPON electrolyte. If there are no voids in between the battery units, high tensile stresses are formed on the top of the LCO electrode and the sides of the Si electrode, which could further result in crack propagation. With voids on the sides, as the SEM images show in the previous study [85], the tensile stress on the sides could be effectively compensated. However, there is still high tensile stress on the top region of the LCO electrode. Even with voids on the side, the direction of lines in Figure 4-6 implies that the cracks may propagate up. In this specific case (Si-LiPON-LiCoO₂), most of the stress occurred on the top of the battery because that the volume change of the decomposition of LiPON electrolyte (-27%) is much more significant than that of LCO side (-8%). This decomposition-induced stress could be different when using different material combinations and applied potential, depends on the equilibrium interphases on both electrode/electrolyte interfaces.

4.5. Discussions

Other than the stress distribution, it is also essential to compare the maximum first principal tensile stresses in different domains and conditions, as shown in Figure 4-7. The decomposition-induced stress was considered to be generated at the beginning of the cycling, and the charging-induced stress increased with charging time. The comparison shows that the decomposition-induced stress would be more significant than the charging-induced stress if there are no voids in this battery, especially in Si negative electrode and LiPON electrolyte. With the existence of voids, the induced maximum stress from either source is around 2-10 GPa. One interesting result with the charginginduced stress; it seems like irrespective of whether the side surfaces are fixed or not, the maximum stress in LCO electrode and Si electrode is very similar, 6 GPa and 2 GPa at the end of charging, respectively. However, the stress is even higher with voids on the side than the case without voids, which is opposite to the results of the decomposition of the electrolyte. Even though the charginginduced maximum stress is still not as high as the decomposition-induced stress, these results show that the decomposition of electrolyte could be much severe than the cycling of the batteries in terms of the mechanical failure in this specific battery geometry and material combinations. In either case, the LiPON electrolyte is the one that is most likely to have crack propagation since it is where the maximum first principal stress is generated.

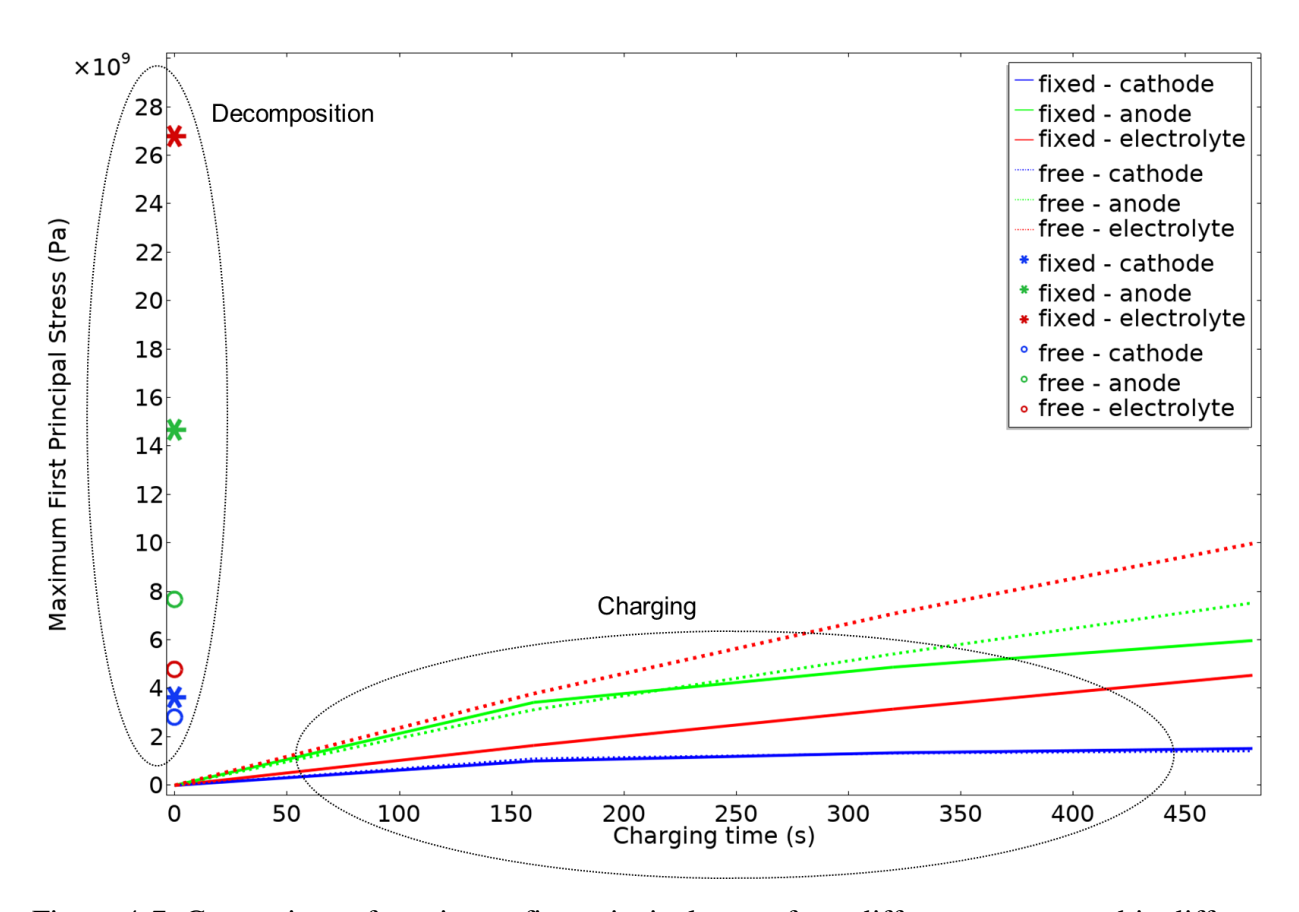


Figure 4-7. Comparison of maximum first principal stress from different sources and in different domains at different charging time at 1.2C. The data of 50 nm interphase layer is used in this plot. Decomposition-induced stress occurs before charging the battery.

4.6. Conclusion

Mechanical failures and cracks are much detrimental in ASSLB than the traditional liquid-based Li-ion batteries, but the related studies are limited. To evaluate the induced-stress in ASSLB, we built up a 3D continuum model with Finite Element Analysis and incorporated two different sources of induced-stress in a 2.5D ASSLB: volume change from the decomposition of LiPON electrolyte and from the charging process that causes the volume change in Si negative electrode and LCO electrode. The decomposition of LiPON and the formation of 50 nm interphase layers caused -27% and -8% reduction in volume at the Si electrode and LCO electrode interfaces, respectively, and generated tensile stress in most of the area with a maximum of ~27 GPa value

for the first principal stress. However, if voids exist on the sides in between the battery units, the maximum first principal stress could be effectively reduced down to ~5 GPa. On the other hand, the induced-stress from the expansion of Si electrode and the contraction of LCO electrode while charging is only 5 GPa at the maximum, and it only affected the surface layer of LCO and inside of Si. In opposite to the decomposition results, the voids on the side would increase the maximum tensile stress to 10 GPa in LiPON instead because Si electrode expands in this case. These results suggested the chemical-stress from the decomposition of solid electrolyte could be much severe than that in the electrode due to the electrochemical cycling. Both will depend largely on the electrode/electrolyte materials used in ASSLB. Furthermore, this continuum model can be used for evaluating the induced stresses for different material combinations and different architecture of ASSLB in terms of developing a less-stressed and high energy density ASSLB.

APPENDIX

Table 4-3. Parameters used in this simulation.

Control variables	Description	Value	
C_{Li}^0 +	Initial concentration of Li-ion in Li ₂ PO ₂ N electrolyte	2x10 ⁴ [mol/m ³]	
$\mathcal{C}^0_{Li_negative}$	Initial concentration of Li in Li _x Si negative electrode	1.4x10 ⁵ [mol/m ³]	
$C^0_{Li_positive}$	Initial concentration of Li in Li _y CoO ₂ positive electrode	4.9x10 ⁴ [mol/m ³]	
$a_{ m v,Si}$	Volume change coefficient of Si electrode (within Si and Li _{3.75} Si)	8.45x10 ⁻⁴ [%/(mol·m ⁻³)]	
a _{v,LiCoO2}	Volume change coefficient of LCO electrode (within Li _{0.5} CoO ₂ and LiCoO ₂)	8x10 ⁻⁵ [%/(mol·m ⁻³)]	
D_{Li_normal}	Normal diffusion coefficient of Li in Li _y CoO ₂ positive electrode	2.5x10 ⁻¹⁸ [m ² /s]	
$D_{Li_lateral}$	Lateral diffusion coefficient of Li in Li _y CoO ₂ positive electrode	1x10 ⁻²¹ [m ² /s]	
D_{Li} +	Diffusion coefficient of Li-ion in Li ₂ PO ₂ N electrolyte	5x10 ⁻¹⁷ [m ² /s]	
D_n	Diffusion coefficient of negative charge in Li ₂ PO ₂ N electrolyte	5x10 ⁻¹⁷ [m ² /s]	
$lpha_{negative}$	Charge transfer coefficient at Li _x Si negative electrode	0.5	
$lpha_{positive}$	Charge transfer coefficient at Li _y CoO ₂ positive electrode	0.5	
$C_{Li_negative_max}$	Maximum concentration of Li-ion in Li _x Si negative electrode	3.11x10 ⁵ [mol/m ³]	
$C_{Li_negative_min}$	Minimum concentration of Li-ion in Li _x Si negative electrode	0 [mol/m ³]	
$C_{Li_positive_max}$	Maximum concentration of Li-ion in Li _y CoO ₂ positive electrode	5x10 ⁴ [mol/m ³]	

Table 4-3 (cont'd).

$C_{Li_positive_min}$	Minimum concentration of Li-ion in Li _y CoO ₂ positive electrode	2.5x10 ⁴ [mol/m ³]
$k_{negative}$	Kinetic constant at the negative electrode/electrolyte surface	1x10 ⁻² [mol/(m ² ·s)]
$k_{positive}$	Kinetic constant at the positive electrode/electrolyte surface	1x10 ⁻⁴ [mol/(m ² ·s)]
Z_{Li} +	Charge on Li-ion in Li ₂ PO ₂ N electrolyte	+1
Z_n	Charge on negative charge in Li ₂ PO ₂ N electrolyte	-1
E_{Si}	Young's modulus of Si electrode	96 [GPa] [222]
$ u_{si}$	Poisson's ratio of Si electrode	0.29 [222]
$ ho_{Si}$	Density of Si electrode	2209 [kg/m ³] [332]
E_{LiCoO_2}	Young's modulus of LiCoO2 electrode	191 [GPa] [333]
$ u_{LiCoO_2}$	Poisson's ratio of LiCoO ₂ electrode	0.24 [333]
$ ho_{LiCoO_2}$	Density of LiCoO ₂ electrode	4790 [kg/m ³] [333]
E_{LiPON}	Young's modulus of LiPON electrolyte	77 [GPa] [45]
$ u_{LiPON}$	Poisson's ratio of LiPON electrode	0.25 [45]
$ ho_{LiPON}$	Density of LiPON electrode	2300 [kg/m ³] [334]

$$E_{negative}(a) = -4.76 \cdot a^6 + 9.34 \cdot a^5 - 1.8 \cdot a^4 - 7.13 \cdot a^3 + 5.8 \cdot a^2 - 1.94 \cdot a + 0.62$$
 Eq. 4-14,

 $E_{positive}(b)$

$$=\frac{207.168\cdot b^{10}-467.807\cdot b^{8}+354.911\cdot b^{6}-198.242\cdot b^{4}+322.003\cdot b^{2}-219.027}{80.310\cdot b^{10}-182.567\cdot b^{8}+113.081\cdot b^{6}-3.43\cdot b^{4}+35.463\cdot b^{2}-44.337}$$

Eq. 4-15,

where a and b is the Li ratio in negative electrode and positive electrode as a =

$$\frac{c_{\textit{Li_negative}}}{c_{\textit{Li_negative_max}}} \; (0-3.75) \; \text{and} \; b = \frac{c_{\textit{Li_positive}}}{c_{\textit{Li_positive_max}}} (0.5-1).$$

BIBLIOGRAPHY

BIBLIOGRAPHY

- 1. Nishi, Y., *Lithium ion secondary batteries; past 10 years and the future.* Journal of Power Sources, 2001. **100**(1-2): p. 101-106.
- 2. Armand, M. and J.-M. Tarascon, *Building better batteries*. nature, 2008. **451**(7179): p. 652.
- 3. Li, W., J.R. Dahn, and D.S. Wainwright, *Rechargeable lithium batteries with aqueous electrolytes*, Science, 1994. **264**(5162): p. 1115-1118.
- 4. Owens, B. and P. Skarstad, *Ambient temperature solid state batteries*. Solid state ionics, 1992. **53**: p. 665-672.
- 5. Yao, X., et al., *All-solid-state lithium batteries with inorganic solid electrolytes: Review of fundamental science.* Chinese Physics B, 2015. **25**(1): p. 018802.
- 6. Li, J.C., et al., *Solid Electrolyte: the Key for High-Voltage Lithium Batteries*. Advanced Energy Materials, 2015. **5**(4): p. 6.
- 7. Ogawa, M., K. Yoshida, and K. Harada, *All-Solid-State Lithium Batteries with Wide Operating Temperature Range*. Sei technical review, 2012(74): p. 89.
- 8. Tarascon, J.M. and M. Armand, *Issues and challenges facing rechargeable lithium batteries*. Nature, 2001. **414**(6861): p. 359-367.
- 9. Sousa, R., et al. *All-solid-state batteries: an overview for bio applications.* in 2013 IEEE 3rd Portuguese Meeting in Bioengineering (ENBENG). 2013. IEEE.
- 10. Leng, F., C.M. Tan, and M. Pecht, *Effect of temperature on the aging rate of Li ion battery operating above room temperature*. Scientific reports, 2015. **5**: p. 12967.
- 11. Takada, K., *Progress and prospective of solid-state lithium batteries*. Acta Materialia, 2013. **61**(3): p. 759-770.
- 12. Bachman, J.C., et al., *Inorganic solid-state electrolytes for lithium batteries: mechanisms and properties governing ion conduction.* Chemical reviews, 2015. **116**(1): p. 140-162.
- 13. Boukamp, B. and R. Huggins, *Lithium ion conductivity in lithium nitride*. Physics Letters A, 1976. **58**(4): p. 231-233.
- 14. Zhao, Y. and L.L. Daemen, *Superionic conductivity in lithium-rich anti-perovskites*. Journal of the American Chemical Society, 2012. **134**(36): p. 15042-15047.
- 15. Yu, X.H., et al., A stable thin-film lithium electrolyte: Lithium phosphorus oxynitride. Journal of the Electrochemical Society, 1997. **144**(2): p. 524-532.

- 16. Bates, J., et al., *Thin-film lithium and lithium-ion batteries*. Solid state ionics, 2000. **135**(1-4): p. 33-45.
- 17. Neudecker, B., N. Dudney, and J. Bates, "Lithium-free" thin-film battery with in situ plated Li anode. Journal of the Electrochemical Society, 2000. **147**(2): p. 517-523.
- 18. Luntz, A.C., J. Voss, and K. Reuter, *Interfacial Challenges in Solid-State Li Ion Batteries*. Journal of Physical Chemistry Letters, 2015. **6**(22): p. 4599-4604.
- 19. Kamaya, N., et al., A lithium superionic conductor. Nature materials, 2011. **10**(9): p. 682.
- 20. Lin, X., et al., *High temperature electrical energy storage: advances, challenges, and frontiers.* Chemical **Society** Reviews, 2016. **45**(21): p. 5848-5887.
- 21. Guerard, D. and A. Herold, *Intercalation of lithium into graphite and other carbons*. Carbon, 1975. **13**(4): p. 337-345.
- 22. Janek, J. and W.G. Zeier, *A solid future for battery development*. Energy, 2016. **500**(400): p. 300.
- 23. Liang, Z., et al., Composite lithium metal anode by melt infusion of lithium into a 3D conducting scaffold with lithiophilic coating. Proceedings of the National Academy of Sciences, 2016. **113**(11): p. 2862-2867.
- 24. Zhu, Y., X. He, and Y. Mo, *Origin of outstanding stability in the lithium solid electrolyte materials: insights from thermodynamic analyses based on first-principles calculations*. ACS applied materials & interfaces, 2015. **7**(42): p. 23685-23693.
- 25. Zhu, Y.Z., X.F. He, and Y.F. Mo, First principles study on electrochemical and chemical stability of solid electrolyte-electrode interfaces in all-solid-state Li-ion batteries. Journal of Materials Chemistry A, 2016. **4**(9): p. 3253-3266.
- 26. Mizushima, K., et al., *LixCoO2* (0< x<-1): A new cathode material for batteries of high energy density. Materials Research Bulletin, 1980. **15**(6): p. 783-789.
- 27. Hayashi, A., et al., *All-solid-state Li/S batteries with highly conductive glass–ceramic electrolytes.* Electrochemistry communications, 2003. **5**(8): p. 701-705.
- 28. Kobayashi, Y., et al., 5 V class all-solid-state composite lithium battery with Li3 PO 4 coated LiNio. 5Mn1. 5 O 4. Journal of the Electrochemical Society, 2003. **150**(12): p. A1577-A1582.
- 29. Li, J., et al., *Solid electrolyte: the key for high-voltage lithium batteries*. Advanced Energy Materials, 2015. **5**(4): p. 1401408.
- 30. Schnell, J., et al., *All-solid-state lithium-ion and lithium metal batteries—paving the way to large-scale production.* Journal of Power Sources, 2018. **382**: p. 160-175.

- 31. Lewis, J.A., et al., *Chemo-Mechanical Challenges in Solid-State Batteries*. Trends in Chemistry, 2019.
- 32. Yao, X.Y., et al., *All-solid-state lithium batteries with inorganic solid electrolytes: Review of fundamental science.* Chinese Physics B, 2016. **25**(1): p. 14.
- 33. Kato, A., et al., *High-Temperature Performance of All-Solid-State Lithium-Metal Batteries Having Li/Li3PS4 Interfaces Modified with Au Thin Films*. Journal of The Electrochemical Society, 2018. **165**(9): p. A1950-A1954.
- 34. Choudhury, S. and L.A. Archer, *Lithium fluoride additives for stable cycling of lithium batteries at high current densities.* Advanced Electronic Materials, 2016. **2**(2): p. 1500246.
- 35. Qian, J., et al., *High rate and stable cycling of lithium metal anode*. Nature communications, 2015. **6**: p. 6362.
- 36. Greer, J.R.; Available from: https://www.caltech.edu/about/news/building-better-batteries-53344.
- 37. He, Y., et al., *Interfacial Incompatibility and Internal Stresses in All-Solid-State Lithium Ion Batteries*. Advanced Energy Materials, 2019: p. 1901810.
- 38. Lewis, J.A., et al., *Interphase morphology between a solid-state electrolyte and lithium controls cell failure*. ACS Energy Letters, 2019. **4**(2): p. 591-599.
- 39. Du, M., et al., Recent advances in the interface engineering of solid-state Li-ion batteries with artificial buffer layers: challenges, materials, construction, and characterization. Energy & Environmental Science, 2019.
- 40. Xu, J., et al., *Mechanical and Electronic Stabilization of Solid Electrolyte Interphase with Sulfite Additive for Lithium Metal Batteries*. Journal of The Electrochemical Society, 2019. **166**(14): p. A3201-A3206.
- 41. Lin, Y.-X., et al., Connecting the irreversible capacity loss in Li-ion batteries with the electronic insulating properties of solid electrolyte interphase (SEI) components. Journal of Power Sources, 2016. **309**: p. 221-230.
- 42. Tippens, J., et al., *Visualizing Chemo-Mechanical Degradation of a Solid-State Battery Electrolyte*. ACS Energy Letters, 2019.
- 43. Monroe, C. and J. Newman, *The impact of elastic deformation on deposition kinetics at lithium/polymer interfaces*. Journal of the Electrochemical Society, 2005. **152**(2): p. A396-A404.
- 44. Baranowski, L.L., et al., *Multi-scale mechanical behavior of the Li3PS4 solid-phase electrolyte*. ACS applied materials & interfaces, 2016. **8**(43): p. 29573-29579.

- 45. Herbert, E.G., et al., *Mechanical characterization of LiPON films using nanoindentation*. Thin Solid Films, 2011. **520**(1): p. 413-418.
- 46. Deng, Z., et al., *Elastic properties of alkali superionic conductor electrolytes from first principles calculations*. Journal of The Electrochemical Society, 2016. **163**(2): p. A67-A74.
- 47. Ni, J.E., et al., *Room temperature elastic moduli and Vickers hardness of hot-pressed LLZO cubic garnet.* Journal of Materials Science, 2012. **47**(23): p. 7978-7985.
- 48. Ishiguro, K., et al., *Stability of Nb-doped cubic Li7La3Zr2O12 with lithium metal.* Journal of The Electrochemical Society, 2013. **160**(10): p. A1690-A1693.
- 49. Ishiguro, K., et al., *Ta-doped Li7La3Zr2O12 for water-stable lithium electrode of lithium-air batteries*. Journal of The Electrochemical Society, 2014. **161**(5): p. A668-A674.
- 50. Sudo, R., et al., *Interface behavior between garnet-type lithium-conducting solid electrolyte and lithium metal.* Solid State Ionics, 2014. **262**: p. 151-154.
- 51. Fudong Han, A.S.W., Jie Yue, Xiulin Fan, Fei Wang, Miaofang Chi, Donovan N. Leonard, Nancy J. Dudney, Howard Wang, Chunsheng Wang *High electronic conductivity as the origin of lithium dendrite formation within solid electrolytes*. Nature energy, 2019.
- 52. Porz, L., et al., *Mechanism of Lithium Metal Penetration through Inorganic Solid Electrolytes*. Advanced Energy Materials, 2017. **7**(20): p. 12.
- 53. Tsai, C.L., et al., *Li7La3Zr2O12 Interface Modification for Li Dendrite Prevention*. Acs Applied Materials & Interfaces, 2016. **8**(16): p. 10617-10626.
- 54. Yang, C.P., et al., *Garnet/polymer hybrid ion-conducting protective layer for stable lithium metal anode*. Nano Research, 2017. **10**(12): p. 4256-4265.
- 55. Raj, R. and J. Wolfenstine, *Current limit diagrams for dendrite formation in solid-state electrolytes for Li-ion batteries*. Journal of Power Sources, 2017. **343**: p. 119-126.
- 56. Tsai, C.-L., et al., *Li7La3Zr2O12 interface modification for Li dendrite prevention*. ACS applied materials & interfaces, 2016. **8**(16): p. 10617-10626.
- 57. Cheng, E.J., A. Sharafi, and J. Sakamoto, *Intergranular Li metal propagation through polycrystalline Li6*. 25Al0. 25La3Zr2O12 ceramic electrolyte. Electrochimica Acta, 2017. **223**: p. 85-91.
- 58. Yonemoto, F., et al., *Temperature effects on cycling stability of Li plating/stripping on Tadoped Li7La3Zr2O12*. Journal of Power Sources, 2017. **343**: p. 207-215.
- 59. Kerman, K., et al., practical challenges hindering the development of solid state Li ion batteries. Journal of The Electrochemical Society, 2017. **164**(7): p. A1731-A1744.

- 60. Porz, L., et al., *Mechanism of lithium metal penetration through inorganic solid electrolytes*. Advanced Energy Materials, 2017. **7**(20): p. 1701003.
- 61. Suzuki, Y., et al., Transparent cubic garnet-type solid electrolyte of Al 2 O 3-doped Li 7 La 3 Zr 2 O 12. Solid State Ionics, 2015. **278**: p. 172-176.
- 62. Hongahally Basappa, R., et al., *Grain boundary modification to suppress lithium penetration through garnet-type solid electrolyte*. Journal of Power Sources, 2017. **363**: p. 145-152.
- 63. Taylor, N.J., et al., Demonstration of high current densities and extended cycling in the garnet Li 7 La 3 Zr 2 O 12 solid electrolyte. Journal of Power Sources, 2018. **396**: p. 314-318.
- 64. Xu, B.Y., et al., *Li3PO4-added garnet-type Li6.5La3Zr1.5Ta0.5O12 for Li-dendrite suppression.* Journal of Power Sources, 2017. **354**: p. 68-73.
- 65. Cheng, L., et al., Effect of surface microstructure on electrochemical performance of garnet solid electrolytes. ACS applied materials & interfaces, 2015. **7**(3): p. 2073-2081.
- 66. Aguesse, F., et al., *Investigating the Dendritic Growth during Full Cell Cycling of Garnet Electrolyte in Direct Contact with Li Metal.* Acs Applied Materials & Interfaces, 2017. **9**(4): p. 3808-3816.
- 67. Thompson, T., et al., *Electrochemical Window of the Li-Ion Solid Electrolyte Li7La3Zr2O12*. Acs Energy Letters, 2017. **2**(2): p. 462-468.
- 68. Yang, Y., et al., *Elastic properties, defect thermodynamics, electrochemical window, phase stability, and Li+ mobility of Li3PS4: Insights from first-principles calculations.* ACS applied materials & interfaces, 2016. **8**(38): p. 25229-25242.
- 69. Davidge, R.W., Mechanical behaviour of ceramics. 1979: CUP Archive.
- 70. Mecholsky, J.J., S. Freimam, and R.W. Rice, *Fracture surface analysis of ceramics*. Journal of Materials Science, 1976. **11**(7): p. 1310-1319.
- 71. Rice, R.W., *Pores as fracture origins in ceramics*. Journal of Materials science, 1984. **19**(3): p. 895-914.
- 72. Gao, Z., et al., *Promises, challenges, and recent progress of inorganic solid-state electrolytes for all-solid-state lithium batteries.* Advanced materials, 2018. **30**(17): p. 1705702.
- 73. Manthiram, A., X. Yu, and S. Wang, *Lithium battery chemistries enabled by solid-state electrolytes*. Nature Reviews Materials, 2017. **2**(4): p. 16103.

- 74. Murugan, R., V. Thangadurai, and W. Weppner, *Fast lithium ion conduction in garnet-type Li7La3Zr2O12*. Angewandte Chemie International Edition, 2007. **46**(41): p. 7778-7781.
- 75. Ohta, S., et al., *All-solid-state lithium ion battery using garnet-type oxide and Li3BO3 solid electrolytes fabricated by screen-printing.* Journal of Power Sources, 2013. **238**: p. 53-56.
- 76. Li, W.J., et al., Fabrication and All Solid-State Battery Performance of TiS2/Li10GeP2S12 Composite Electrodes. Materials Transactions, 2016. **57**(4): p. 549-552.
- 77. Sakuda, A., A. Hayashi, and M. Tatsumisago, *Interfacial observation between LiCoO2 electrode and Li2S-P2S5 solid electrolytes of all-solid-state lithium secondary batteries using transmission electron microscopy*. Chemistry of Materials, 2009. **22**(3): p. 949-956.
- 78. Danilov, D., R. Niessen, and P. Notten, *Modeling all-solid-state Li-ion batteries*. Journal of the Electrochemical Society, 2011. **158**(3): p. A215-A222.
- 79. Du, F., et al., *All solid state lithium batteries based on lamellar garnet-type ceramic electrolytes.* Journal of Power Sources, 2015. **300**: p. 24-28.
- 80. Tatsumisago, M., M. Nagao, and A. Hayashi, *Recent development of sulfide solid electrolytes and interfacial modification for all-solid-state rechargeable lithium batteries.*Journal of Asian Ceramic Societies, 2013. **1**(1): p. 17-25.
- 81. Aboulaich, A., et al., *A New Approach to Develop Safe All-Inorganic Monolithic Li-Ion Batteries*. Advanced Energy Materials, 2011. **1**(2): p. 179-183.
- 82. Notten, P.H., et al., *3-D integrated all-solid-state rechargeable batteries*. Advanced Materials, 2007. **19**(24): p. 4564-4567.
- 83. Ruzmetov, D., et al., *Electrolyte stability determines scaling limits for solid-state 3D Li ion batteries*. Nano letters, 2011. **12**(1): p. 505-511.
- 84. Arthur, T.S., et al., *Three-dimensional electrodes and battery architectures*. Mrs Bulletin, 2011. **36**(7): p. 523-531.
- 85. Talin, A.A., et al., Fabrication, Testing, and Simulation of All-Solid-State Three-Dimensional Li-Ion Batteries. Acs Applied Materials & Interfaces, 2016. **8**(47): p. 32385-32391.
- 86. Wang, P., et al., *Electro–Chemo–Mechanical Issues at the Interfaces in Solid-State Lithium Metal Batteries*. Advanced Functional Materials, 2019: p. 1900950.
- 87. Strauss, F., et al., *Impact of cathode material particle size on the capacity of bulk-type all-solid-state batteries*. ACS Energy Letters, 2018. **3**(4): p. 992-996.

- 88. Oh, D.Y., et al., Excellent Compatibility of Solvate Ionic Liquids with Sulfide Solid Electrolytes: Toward Favorable Ionic Contacts in Bulk-Type All-Solid-State Lithium-Ion Batteries. Advanced Energy Materials, 2015. 5(22): p. 1500865.
- 89. Bower, A.F., P.R. Guduru, and V.A. Sethuraman, *A finite strain model of stress, diffusion, plastic flow, and electrochemical reactions in a lithium-ion half-cell.* Journal of the Mechanics and Physics of Solids, 2011. **59**(4): p. 804-828.
- 90. McDowell, M.T., S. Xia, and T. Zhu, *The mechanics of large-volume-change transformations in high-capacity battery materials*. Extreme Mechanics Letters, 2016. **9**: p. 480-494.
- 91. Mukhopadhyay, A. and B.W. Sheldon, *Deformation and stress in electrode materials for Li-ion batteries*. Progress in Materials Science, 2014. **63**: p. 58-116.
- 92. Zeng, Z., et al., *In situ measurement of lithiation-induced stress in silicon nanoparticles using micro-Raman spectroscopy.* Nano Energy, 2016. **22**: p. 105-110.
- 93. Gao, J., S.-Q. Shi, and H. Li, *Brief overview of electrochemical potential in lithium ion batteries*. Chinese Physics B, 2015. **25**(1): p. 018210.
- 94. Danilov, D., R.A.H. Niessen, and P.H.L. Notten, *Modeling All-Solid-State Li-Ion Batteries*. Journal of the Electrochemical Society, 2011. **158**(3): p. A215-A222.
- 95. Fu, K.K., et al., Toward garnet electrolyte-based Li metal batteries: An ultrathin, highly effective, artificial solid-state electrolyte/metallic Li interface. Science Advances, 2017. 3(4): p. e1601659.
- 96. Shin, B.R., et al., *Interfacial architecture for extra Li+ storage in all-solid-state lithium batteries*. Scientific reports, 2014. **4**: p. 5572.
- 97. Shenoy, V.B., P. Johari, and Y. Qi, *Elastic softening of amorphous and crystalline Li–Si phases with increasing Li concentration: a first-principles study.* Journal of Power Sources, 2010. **195**(19): p. 6825-6830.
- 98. Dahn, J., et al., *Structure determination of Li x TiS2 by neutron diffraction*. Canadian Journal of Physics, 1980. **58**(2): p. 207-213.
- 99. Goodenough, J.B. and Y. Kim, *Challenges for rechargeable Li batteries*. Chemistry of materials, 2009. **22**(3): p. 587-603.
- 100. An, S.J., et al., The state of understanding of the lithium-ion-battery graphite solid electrolyte interphase (SEI) and its relationship to formation cycling. Carbon, 2016. **105**: p. 52-76.
- 101. Lu, D., et al., Failure mechanism for fast-charged lithium metal batteries with liquid electrolytes. Advanced Energy Materials, 2015. 5(3): p. 1400993.

- 102. Peled, E., D. Golodnitsky, and G. Ardel, *Advanced model for solid electrolyte interphase electrodes in liquid and polymer electrolytes*. Journal of The Electrochemical Society, 1997. **144**(8): p. L208-L210.
- 103. Jung, Y.S., et al., *Issues and Challenges for Bulk-Type All-Solid-State Rechargeable Lithium Batteries using Sulfide Solid Electrolytes*. Israel Journal of Chemistry, 2015. **55**(5): p. 472-485.
- 104. Liu, J., et al., *All-solid-state Lithium Ion Battery: Research and Industrial Prospects*. Acta Chimica Sinica, 2013. **71**(6): p. 869-878.
- 105. Chung, H. and B. Kang, *Mechanical and thermal failure induced by contact between a Li1.* 5Alo. 5Ge1. 5 (PO4) 3 solid electrolyte and Li metal in an all solid-state Li cell. Chemistry of Materials, 2017. **29**(20): p. 8611-8619.
- 106. West, W.C., et al., Reduction of charge-transfer resistance at the solid electrolyte–electrode interface by pulsed laser deposition of films from a crystalline Li2PO2N source. Journal of Power Sources, 2016. **312**: p. 116-122.
- 107. Kuwata, N., et al., Characterization of thin-film lithium batteries with stable thin-film Li3PO4 solid electrolytes fabricated by ArF excimer laser deposition. Journal of The Electrochemical Society, 2010. **157**(4): p. A521-A527.
- 108. Ohta, N., et al., *LiNbO3-coated LiCoO2 as cathode material for all solid-state lithium secondary batteries*. Electrochemistry communications, 2007. **9**(7): p. 1486-1490.
- 109. Wang, C., et al., Conformal, nanoscale ZnO surface modification of garnet-based solid-state electrolyte for lithium metal anodes. Nano letters, 2016. **17**(1): p. 565-571.
- 110. Nagao, M., A. Hayashi, and M. Tatsumisago, *High-capacity Li 2 S—nanocarbon composite electrode for all-solid-state rechargeable lithium batteries*. Journal of Materials Chemistry, 2012. **22**(19): p. 10015-10020.
- 111. Hayashi, A., et al., *Novel technique to form electrode–electrolyte nanointerface in all-solid-state rechargeable lithium batteries.* Electrochemistry Communications, 2008. **10**(12): p. 1860-1863.
- 112. Kitaura, H., et al., Fabrication of electrode–electrolyte interfaces in all-solid-state rechargeable lithium batteries by using a supercooled liquid state of the glassy electrolytes. Journal of Materials Chemistry, 2011. **21**(1): p. 118-124.
- 113. Ferrari, S., et al., *Latest advances in the manufacturing of 3D rechargeable lithium microbatteries*. Journal of Power Sources, 2015. **286**: p. 25-46.
- 114. Zienkiewicz, O.C., et al., *The finite element method*. Vol. 3. 1977: McGraw-hill London.
- 115. Schrödinger, E., *An undulatory theory of the mechanics of atoms and molecules*. Physical review, 1926. **28**(6): p. 1049.

- 116. Hartree, D.R. The wave mechanics of an atom with a non-Coulomb central field. Part I. Theory and methods. in Mathematical Proceedings of the Cambridge Philosophical Society. 1928. Cambridge University Press.
- 117. Møller, C. and M.S. Plesset, *Note on an approximation treatment for many-electron systems*. Physical review, 1934. **46**(7): p. 618.
- 118. Čížek, J., On the correlation problem in atomic and molecular systems. Calculation of wavefunction components in Ursell-type expansion using quantum-field theoretical methods. The Journal of Chemical Physics, 1966. **45**(11): p. 4256-4266.
- 119. Sherrill, C.D. and H.F. Schaefer III, *The configuration interaction method: Advances in highly correlated approaches*, in *Advances in quantum chemistry*. 1999, Elsevier. p. 143-269.
- 120. Nakano, H., Quasidegenerate perturbation theory with multiconfigurational self-consistent-field reference functions. The Journal of chemical physics, 1993. **99**(10): p. 7983-7992.
- 121. Kohn, W. and L.J. Sham, *Self-consistent equations including exchange and correlation effects.* Physical review, 1965. **140**(4A): p. A1133.
- 122. Hohenberg, P. and W. Kohn, *Inhomogeneous electron gas*. Physical review, 1964. **136**(3B): p. B864.
- 123. Jain, A., Y. Shin, and K.A. Persson, *Computational predictions of energy materials using density functional theory*. Nature Reviews Materials, 2016. **1**(1): p. 15004.
- 124. Perdew, J.P., et al., *Some fundamental issues in ground-state density functional theory: A guide for the perplexed.* Journal of chemical theory and computation, 2009. **5**(4): p. 902-908.
- 125. Aydinol, M., et al., *Ab initio study of lithium intercalation in metal oxides and metal dichalcogenides.* Physical Review B, 1997. **56**(3): p. 1354.
- 126. Ceder, G., et al., *Identification of cathode materials for lithium batteries guided by first-principles calculations.* Nature, 1998. **392**(6677): p. 694.
- 127. Van der Ven, A., M.K. Aydinol, and G. Ceder, *First-Principles Evidence for Stage Ordering in Li x CoO2*. Journal of The Electrochemical Society, 1998. **145**(6): p. 2149-2155.
- 128. Van der Ven, A. and G. Ceder, *Lithium diffusion in layered Li x CoO2*. Electrochemical and Solid-State Letters, 2000. **3**(7): p. 301-304.
- 129. Ong, S.P., et al., *Li Fe P O2 phase diagram from first principles calculations*. Chemistry of Materials, 2008. **20**(5): p. 1798-1807.

- 130. Ong, S.P., et al., Thermal stabilities of delithiated olivine MPO4 (M= Fe, Mn) cathodes investigated using first principles calculations. Electrochemistry Communications, 2010. **12**(3): p. 427-430.
- 131. Kang, K., et al., *Electrodes with high power and high capacity for rechargeable lithium batteries*. Science, 2006. **311**(5763): p. 977-980.
- 132. Ong, S.P., et al., *Phase stability, electrochemical stability and ionic conductivity of the Li* 10±1 MP 2 X 12 (M= Ge, Si, Sn, Al or P, and X= O, S or Se) family of superionic conductors. Energy & Environmental Science, 2013. **6**(1): p. 148-156.
- 133. He, X., Y. Zhu, and Y. Mo, *Origin of fast ion diffusion in super-ionic conductors*. Nature communications, 2017. **8**: p. 15893.
- 134. Meier, K., T. Laino, and A. Curioni, *Solid-state electrolytes: revealing the mechanisms of Li-ion conduction in tetragonal and cubic LLZO by first-principles calculations.* The Journal of Physical Chemistry C, 2014. **118**(13): p. 6668-6679.
- 135. Cohen, A.J., P. Mori-Sánchez, and W. Yang, *Insights into current limitations of density functional theory*. Science, 2008. **321**(5890): p. 792-794.
- 136. Grazioli, D., M. Magri, and A. Salvadori, *Computational modeling of Li-ion batteries*. Computational Mechanics, 2016. **58**(6): p. 889-909.
- 137. Peukert, W., Über die Abhängigkeit der Kapazität von der Entladestromstärke bei Bleiakkumulatoren. Elektrotechnische Zeitschrift, 1897. **20**: p. 20-21.
- 138. Doerffel, D. and S.A. Sharkh, A critical review of using the Peukert equation for determining the remaining capacity of lead-acid and lithium-ion batteries. Journal of power sources, 2006. **155**(2): p. 395-400.
- 139. Chen, M. and G.A. Rincon-Mora, *Accurate electrical battery model capable of predicting runtime and IV performance*. IEEE transactions on energy conversion, 2006. **21**(2): p. 504-511.
- 140. Rong, P. and M. Pedram, *An analytical model for predicting the remaining battery capacity of lithium-ion batteries*. IEEE Transactions on Very Large Scale Integration (VLSI) Systems, 2006. **14**(5): p. 441-451.
- 141. Fares, R.L. and M.E. Webber, *Combining a dynamic battery model with high-resolution smart grid data to assess microgrid islanding lifetime*. Applied Energy, 2015. **137**: p. 482-489.
- 142. von Srbik, M.-T., et al., A physically meaningful equivalent circuit network model of a lithium-ion battery accounting for local electrochemical and thermal behaviour, variable double layer capacitance and degradation. Journal of Power Sources, 2016. **325**: p. 171-184.

- 143. Widanage, W., et al., *Design and use of multisine signals for Li-ion battery equivalent circuit modelling. Part 2: Model estimation.* Journal of Power Sources, 2016. **324**: p. 61-69.
- 144. Buller, S., et al., *Impedance-based simulation models of supercapacitors and Li-ion batteries for power electronic applications*. IEEE Transactions on Industry Applications, 2005. **41**(3): p. 742-747.
- 145. Gao, L., S. Liu, and R.A. Dougal, *Dynamic lithium-ion battery model for system simulation*. IEEE transactions on components and packaging technologies, 2002. **25**(3): p. 495-505.
- 146. Gold, S. A PSPICE macromodel for lithium-ion batteries. in The Twelfth Annual Battery Conference on Applications and Advances. 1997. IEEE.
- 147. Cahn, J.W. and J.E. Hilliard, *Free energy of a nonuniform system. I. Interfacial free energy.* The Journal of chemical physics, 1958. **28**(2): p. 258-267.
- 148. Han, B., et al., *Electrochemical modeling of intercalation processes with phase field models*. Electrochimica Acta, 2004. **49**(26): p. 4691-4699.
- 149. Li, Y., et al., Current-induced transition from particle-by-particle to concurrent intercalation in phase-separating battery electrodes. Nature materials, 2014. **13**(12): p. 1149.
- 150. Deng, J., G.J. Wagner, and R.P. Muller, *Phase field modeling of solid electrolyte interface formation in lithium ion batteries*. Journal of the Electrochemical Society, 2013. **160**(3): p. A487-A496.
- 151. Taflove, A. and S.C. Hagness, *Computational electrodynamics: the finite-difference time-domain method.* 2005: Artech house.
- 152. Mayneord, W.V., *John Alfred Valentine Butler*, *14 February 1899-16 July 1977*. 1979, The Royal Society London.
- 153. Santhanagopalan, S., et al., *Review of models for predicting the cycling performance of lithium ion batteries*. Journal of Power Sources, 2006. **156**(2): p. 620-628.
- 154. Arora, P., et al., Comparison between computer simulations and experimental data for high-rate discharges of plastic lithium-ion batteries. Journal of power Sources, 2000. **88**(2): p. 219-231.
- 155. Botte, G.G., V.R. Subramanian, and R.E. White, *Mathematical modeling of secondary lithium batteries*. Electrochimica Acta, 2000. **45**(15-16): p. 2595-2609.
- Doyle, M., et al., *Comparison of modeling predictions with experimental data from plastic lithium ion cells.* Journal of the Electrochemical Society, 1996. **143**(6): p. 1890-1903.

- 157. Fuller, T.F., M. Doyle, and J. Newman, *Relaxation phenomena in lithium-ion-insertion cells*. Journal of the Electrochemical Society, 1994. **141**(4): p. 982-990.
- 158. Gomadam, P.M., et al., *Mathematical modeling of lithium-ion and nickel battery systems*. Journal of power sources, 2002. **110**(2): p. 267-284.
- 159. Ning, G., R.E. White, and B.N. Popov, *A generalized cycle life model of rechargeable Liion batteries*. Electrochimica acta, 2006. **51**(10): p. 2012-2022.
- 160. Ramadass, P., et al., *Development of first principles capacity fade model for Li-ion cells.* Journal of the Electrochemical Society, 2004. **151**(2): p. A196-A203.
- 161. Ramadass, P., et al., *Mathematical modeling of the capacity fade of Li-ion cells*. Journal of Power Sources, 2003. **123**(2): p. 230-240.
- 162. Newman, J., et al., *Modeling of lithium-ion batteries*. Journal of power sources, 2003. **119**: p. 838-843.
- 163. Bates, A., et al., *Modeling and simulation of 2D lithium-ion solid state battery*. International Journal of Energy Research, 2015. **39**(11): p. 1505-1518.
- 164. Chen, Y. and J.W. Evans, *Three-dimensional thermal modeling of lithium-polymer batteries under galvanostatic discharge and dynamic power profile.* Journal of the Electrochemical Society, 1994. **141**(11): p. 2947-2955.
- 165. Becker-Steinberger, K., et al., A mathematical model for all solid-state lithium-ion batteries. ECS Transactions, 2010. **25**(36): p. 285-296.
- 166. Tang, M., et al., *Model for the particle size, overpotential, and strain dependence of phase transition pathways in storage electrodes: application to nanoscale olivines.* Chemistry of Materials, 2009. **21**(8): p. 1557-1571.
- 167. Bucci, G., et al., *Mechanical instability of electrode-electrolyte interfaces in solid-state batteries*. Physical Review Materials, 2018. **2**(10): p. 105407.
- 168. Tian, H.-K., et al., *Interfacial Electronic Properties Dictate Li Dendrite Growth in Solid Electrolytes*. Chemistry of Materials, 2019.
- 169. Kim, K.J., et al., *Atomistic simulation derived insight on the irreversible structural changes of Si electrode during fast and slow delithiation*. Nano letters, 2017. **17**(7): p. 4330-4338.
- 170. Tian, H.-K., B. Xu, and Y. Qi, Computational study of lithium nucleation tendency in Li 7 La 3 Zr 2 O 12 (LLZO) and rational design of interlayer materials to prevent lithium dendrites. Journal of Power Sources, 2018. **392**: p. 79-86.
- 171. Kim, J.G., et al., *A review of lithium and non-lithium based solid state batteries*. Journal of Power Sources, 2015. **282**: p. 299-322.

- 172. Goodenough, J.B. and Y. Kim, *Challenges for Rechargeable Li Batteries*. Chemistry of Materials, 2010. **22**(3): p. 587-603.
- 173. Ren, Y.Y., et al., *Direct observation of lithium dendrites inside garnet-type lithium-ion solid electrolyte.* Electrochemistry Communications, 2015. **57**: p. 27-30.
- 174. Sharafi, A., et al., Characterizing the Li–Li7La3Zr2O12 interface stability and kinetics as a function of temperature and current density. Journal of Power Sources, 2016. **302**: p. 135-139.
- 175. Ren, Y., et al., *Direct observation of lithium dendrites inside garnet-type lithium-ion solid electrolyte*. Electrochemistry Communications, 2015. **57**: p. 27-30.
- 176. Schmidt, R.D. and J. Sakamoto, *In-situ*, *non-destructive acoustic characterization of solid state electrolyte cells*. Journal of Power Sources, 2016. **324**: p. 126-133.
- 177. Aguesse, F., et al., *Investigating the dendritic growth during full cell cycling of garnet electrolyte in direct contact with Li metal.* ACS applied materials & interfaces, 2017. **9**(4): p. 3808-3816.
- 178. Sharafi, A., et al., Controlling and correlating the effect of grain size with the mechanical and electrochemical properties of Li 7 La 3 Zr 2 O 12 solid-state electrolyte. Journal of Materials Chemistry A, 2017. 5(40): p. 21491-21504.
- 179. Sharafi, A., et al., Surface Chemistry Mechanism of Ultra-Low Interfacial Resistance in the Solid-State Electrolyte Li7La3Zr2O12. Chemistry of Materials, 2017. **29**(18): p. 7961-7968.
- 180. Basappa, R.H., T. Ito, and H. Yamada, *Contact between garnet-type solid electrolyte and lithium metal anode: influence on charge transfer resistance and short circuit prevention.*Journal of The Electrochemical Society, 2017. **164**(4): p. A666-A671.
- 181. Garcia-Mendez, R., et al., *Effect of processing conditions of 75Li2S-25P2S5 solid electrolyte on its DC electrochemical behavior*. Electrochimica Acta, 2017. **237**: p. 144-151.
- 182. Han, F., et al., Suppressing Li dendrite formation in Li2S-P2S5 solid electrolyte by LiI incorporation. Advanced Energy Materials, 2018. **8**(18): p. 1703644.
- 183. Nagao, M., et al., *In situ SEM study of a lithium deposition and dissolution mechanism in a bulk-type solid-state cell with a Li 2 S–P 2 S 5 solid electrolyte.* Physical Chemistry Chemical Physics, 2013. **15**(42): p. 18600-18606.
- 184. Monroe, C. and J. Newman, *The effect of interfacial deformation on electrodeposition kinetics*. Journal of The Electrochemical Society, 2004. **151**(6): p. A880-A886.
- 185. Basappa, R.H., et al., *Grain boundary modification to suppress lithium penetration through garnet-type solid electrolyte.* Journal of Power Sources, 2017. **363**: p. 145-152.

- 186. Wang, H., et al., Fabrication of ultrathin solid electrolyte membranes of β-Li 3 PS 4 nanoflakes by evaporation-induced self-assembly for all-solid-state batteries. Journal of Materials Chemistry A, 2016. **4**(21): p. 8091-8096.
- 187. Tian, H.-K. and Y. Qi, *Simulation of the Effect of Contact Area Loss in All-Solid-State Li-Ion Batteries*. Journal of The Electrochemical Society, 2017. **164**(11): p. E3512-E3521.
- 188. Bucci, G., et al., Modeling of internal mechanical failure of all-solid-state batteries during electrochemical cycling, and implications for battery design. Journal of Materials Chemistry A, 2017. **5**(36): p. 19422-19430.
- 189. Gallium arsenide (GaAs), intrinsic carrier concentration, electrical and thermal conductivity, ed. O. Madelung, U. Rössler, and M. Schulz. Vol. 41A1β. Springer-Verlag Berlin Heidelberg.
- 190. Song, Y., et al., Revealing the Short-Circuiting Mechanism of Garnet-Based Solid-State Electrolyte. Advanced Energy Materials, 2019: p. 1900671.
- 191. Ma, C., et al., *Interfacial Stability of Li Metal-Solid Electrolyte Elucidated via in Situ Electron Microscopy*. Nano Letters, 2016. **16**(11): p. 7030-7036.
- 192. Kozen, A.C., et al., *Atomic layer deposition of the solid electrolyte LiPON*. Chemistry of Materials, 2015. **27**(15): p. 5324-5331.
- 193. George, S.M., *Atomic Layer Deposition: An Overview.* Chemical Reviews, 2010. **110**(1): p. 111-131.
- 194. Lin, C.F., et al., Solid Electrolyte Lithium Phosphous Oxynitride as a Protective Nanocladding Layer for 3D High-Capacity Conversion Electrodes. Acs Nano, 2016. **10**(2): p. 2693-2701.
- 195. Pearse, A.J., et al., *Nanoscale Solid State Batteries Enabled by Thermal Atomic Layer Deposition of a Lithium Polyphosphazene Solid State Electrolyte*. Chemistry of Materials, 2017. **29**(8): p. 3740-3753.
- 196. Senevirathne, K., et al., *A new crystalline LiPON electrolyte: Synthesis, properties, and electronic structure.* Solid State Ionics, 2013. **233**: p. 95-101.
- 197. Chen, L., et al., *Modulation of dendritic patterns during electrodeposition: A nonlinear phase-field model.* Journal of Power Sources, 2015. **300**: p. 376-385.
- 198. Liang, L., et al., *Nonlinear phase-field model for electrode-electrolyte interface evolution.* Physical Review E, 2012. **86**(5): p. 051609.
- 199. Zhang, H.-W., et al., *Understanding and predicting the lithium dendrite formation in Liion batteries: Phase field model.* ECS Transactions, 2014. **61**(8): p. 1-9.

- 200. Zhang, S., Chemomechanical modeling of lithiation-induced failure in high-volume-change electrode materials for lithium ion batteries. npj Computational Materials, 2017. 3(1): p. 7.
- 201. Simmons, J., et al., *Microstructural development involving nucleation and growth phenomena simulated with the phase field method*. Materials Science and Engineering: A, 2004. **365**(1-2): p. 136-143.
- 202. Cheng, E.J., A. Sharafi, and J. Sakamoto, *Intergranular Li metal propagation through polycrystalline Li6.25Al0.25La3Zr2O12 ceramic electrolyte*. Electrochimica Acta, 2017. **223**: p. 85-91.
- 203. Kresse, G. and J. Furthmüller, *Efficient iterative schemes for ab initio total-energy calculations using a plane-wave basis set.* Physical review B, 1996. **54**(16): p. 11169.
- 204. Kresse, G. and D. Joubert, *From ultrasoft pseudopotentials to the projector augmented-wave method.* Physical Review B, 1999. **59**(3): p. 1758.
- 205. Liu, Z., et al., *Anomalous high ionic conductivity of nanoporous* β -*Li3PS4*. Journal of the American Chemical Society, 2013. **135**(3): p. 975-978.
- 206. Perdew, J.P., K. Burke, and M. Ernzerhof, *Generalized gradient approximation made simple*. Physical review letters, 1996. **77**(18): p. 3865.
- 207. Heyd, J., G.E. Scuseria, and M. Ernzerhof, *Hybrid functionals based on a screened Coulomb potential*. The Journal of chemical physics, 2003. **118**(18): p. 8207-8215.
- 208. Krukau, A.V., et al., *Influence of the exchange screening parameter on the performance of screened hybrid functionals.* The Journal of chemical physics, 2006. **125**(22): p. 224106.
- 209. Monkhorst, H.J. and J.D. Pack, *Special points for Brillouin-zone integrations*. Physical review B, 1976. **13**(12): p. 5188.
- 210. Ong, M.T., et al., *Lithium ion solvation and diffusion in bulk organic electrolytes from first-principles and classical reactive molecular dynamics*. The Journal of Physical Chemistry B, 2015. **119**(4): p. 1535-1545.
- 211. Awaka, J., et al., *Synthesis and structure analysis of tetragonal Li7La3Zr2O12 with the garnet-related type structure.* Journal of Solid State Chemistry, 2009. **182**(8): p. 2046-2052.
- 212. Yoder, M.N., *Wide bandgap semiconductor materials and devices*. IEEE Transactions on Electron Devices, 1996. **43**(10): p. 1633-1636.
- 213. Trasatti, S., *The absolute electrode potential: an explanatory note (Recommendations 1986)*. Pure and Applied Chemistry, 1986. **58**(7): p. 955-966.

- 214. Leung, K. and K.L. Jungjohann, *Spatial heterogeneities and onset of passivation breakdown at lithium anode interfaces*. The Journal of Physical Chemistry C, 2017. **121**(37): p. 20188-20196.
- 215. Peljo, P. and H.H. Girault, *Electrochemical potential window of battery electrolytes: the HOMO–LUMO misconception*. Energy & Environmental Science, 2018. **11**(9): p. 2306-2309.
- 216. Cui, J., J. Ristein, and L. Ley, *Electron affinity of the bare and hydrogen covered single crystal diamond (111) surface.* Physical Review Letters, 1998. **81**(2): p. 429.
- 217. Zu, C.X. and H. Li, *Thermodynamic analysis on energy densities of batteries*. Energy & Environmental Science, 2011. **4**(8): p. 2614-2624.
- 218. Robie, R.A. and B.S. Hemingway, *Thermodynamic properties of minerals and related substances at 298.15 K and 1 bar (10*^ 5 Pascals) pressure and at higher temperatures. US Geol. Survey Bull., vol. 2131, p. 461-461 (1995). 1995. **2131**: p. 461-461.
- 219. Zhu, Y.Z., X.F. He, and Y.F. Mo, Strategies Based on Nitride Materials Chemistry to Stabilize Li Metal Anode. Advanced Science, 2017. **4**(8): p. 11.
- 220. Yue, J. and Y.-G. Guo, *The devil is in the electrons*. Nature Energy, 2019. **4**(3): p. 174-175.
- 221. Song, Y., et al., Revealing the Short-Circuiting Mechanism of Garnet-Based Solid-State Electrolyte. Advanced Energy Materials, 2019. **0**(0): p. 1900671.
- 222. Qi, Y., et al., Lithium concentration dependent elastic properties of battery electrode materials from first principles calculations. Journal of The Electrochemical Society, 2014. **161**(11): p. F3010-F3018.
- 223. Ahmad, Z., et al., Machine learning enabled computational screening of inorganic solid electrolytes for suppression of dendrite formation in lithium metal anodes. ACS central science, 2018. **4**(8): p. 996-1006.
- 224. Botros, M., et al., Field assisted sintering of fine-grained Li7– 3xLa3Zr2AlxO12 solid electrolyte and the influence of the microstructure on the electrochemical performance. Journal of Power Sources, 2016. **309**: p. 108-115.
- 225. Hood, Z.D., et al., Fabrication of Sub-Micrometer-Thick Solid Electrolyte Membranes of beta-Li3PS4 via Tiled Assembly of Nanoscale, Plate-Like Building Blocks. Advanced Energy Materials, 2018. 8(21): p. 7.
- 226. Wu, B., et al., *The role of the solid electrolyte interphase layer in preventing Li dendrite growth in solid-state batteries*. Energy & Environmental Science, 2018.
- 227. Liu, Y., et al., *Stabilizing the interface of NASICON solid electrolyte against Li metal with atomic layer deposition*. ACS applied materials & interfaces, 2018. **10**(37): p. 31240-31248.

- 228. Zhang, Z., et al., An advanced construction strategy of all-solid-state lithium batteries with excellent interfacial compatibility and ultralong cycle life. Journal of Materials Chemistry A, 2017. 5(32): p. 16984-16993.
- 229. Han, F.D., et al., *Electrochemical Stability of Li10GeP2S12 and Li7La3Zr2O12 Solid Electrolytes*. Advanced Energy Materials, 2016. **6**(8): p. 9.
- 230. Luo, W., et al., Reducing Interfacial Resistance between Garnet-Structured Solid-State Electrolyte and Li-Metal Anode by a Germanium Layer. Advanced Materials, 2017. **29**(22): p. 7.
- 231. Han, X.G., et al., Negating interfacial impedance in garnet-based solid-state Li metal batteries. Nature Materials, 2017. **16**(5): p. 572-+.
- 232. Rangasamy, E., J. Wolfenstine, and J. Sakamoto, *The role of Al and Li concentration on the formation of cubic garnet solid electrolyte of nominal composition Li7La3Zr2O12*. Solid State Ionics, 2012. **206**: p. 28-32.
- 233. Xie, H., et al., *Lithium Distribution in Aluminum-Free Cubic Li7La3Zr2O12*. Chemistry of Materials, 2011. **23**(16): p. 3587-3589.
- 234. Cussen, E.J., *The structure of lithium garnets: cation disorder and clustering in a new family of fast Li+ conductors.* Chemical Communications, 2006(4): p. 412-413.
- 235. O'Callaghan, M.P. and E.J. Cussen, *Lithium dimer formation in the Li-conducting garnets* Li5+xBaxLa3-xTa2O12 (0 < x <= 1.6). Chemical Communications, 2007(20): p. 2048-2050.
- 236. Homma, K., et al., *Crystal structure and phase transitions of the lithium ionic conductor Li3PS4*. Solid State Ionics, 2011. **182**(1): p. 53-58.
- 237. Lepley, N.D., N.A.W. Holzwarth, and Y.J.A. Du, Structures, Li+ mobilities, and interfacial properties of solid electrolytes Li3PS4 and Li3PO4 from first principles. Physical Review B, 2013. **88**(10): p. 11.
- 238. Aono, H., et al., *IONIC-CONDUCTIVITY OF THE LITHIUM TITANIUM PHOSPHATE* (LI1+XALXTI2-X(PO4)3), (LI1+XSCXTI2-X(PO4)3), (LI1+XYXTI2-X(PO4)3), (LI1+XLAXTI2-X(PO4)3 SYSTEMS. Journal of the Electrochemical Society, 1989. **136**(2): p. 590-591.
- 239. Dashjav, E. and F. Tietz, *Neutron Diffraction Analysis of NASICON-type Li1+ xAlxTi2-xP3O12*. Zeitschrift für anorganische und allgemeine Chemie, 2014. **640**(15): p. 3070-3073.
- 240. Redhammer, G., et al., A single crystal X-ray and powder neutron diffraction study on NASICON-type Li 1+x Al x Ti 2-x (PO 4) 3 ($0 \le x \le 0.5$) crystals: Implications on ionic conductivity. Solid state sciences, 2016. **60**: p. 99-107.

- 241. Deng, Z., et al., *Elastic Properties of Alkali Superionic Conductor Electrolytes from First Principles Calculations*. Journal of the Electrochemical Society, 2016. **163**(2): p. A67-A74.
- 242. Lang, B., B. Ziebarth, and C. Elsasser, *Lithium Ion Conduction in LiTi2(PO4)(3) and Related Compounds Based on the NASICON Structure: A First-Principles Study.* Chemistry of Materials, 2015. **27**(14): p. 5040-5048.
- 243. Yang, J., et al., A High-Rate and Ultralong-Life Sodium-Ion Battery Based on NaTi2(PO4)(3) Nanocubes with Synergistic Coating of Carbon and Rutile TiO2. Small, 2015. 11(31): p. 3744-3749.
- 244. Holzwarth, N., First Principles Modeling of Electrolyte Materials in All-Solid-State Batteries. Physics Procedia, 2014. **57**: p. 29-37.
- 245. Chen, L.J., et al., Oxygen vacancy in LiTiPO5 and LiTi2(PO4)(3): A first-principles study. Physics Letters A, 2011. **375**(5): p. 934-938.
- 246. Murugan, R., V. Thangadurai, and W. Weppner, *Fast lithium ion conduction in garnet-type Li7La3Zr2O12*. Angewandte Chemie-International Edition, 2007. **46**(41): p. 7778-7781.
- 247. Bates, J.B., et al., *Thin-film lithium and lithium-ion batteries*. Solid State Ionics, 2000. **135**(1-4): p. 33-45.
- 248. Dudney, N.J., *Solid-state thin-film rechargeable batteries*. Materials Science and Engineering B-Solid State Materials for Advanced Technology, 2005. **116**(3): p. 245-249.
- 249. Kamaya, N., et al., *A lithium superionic conductor*. Nature Materials, 2011. **10**(9): p. 682-686.
- 250. Inaguma, Y., et al., *High ionic conductivity in lithium lanthanum titanate*. Solid State Communications, 1993. **86**(10): p. 689-693.
- 251. Braga, M., et al., *Alternative strategy for a safe rechargeable battery*. Energy & Environmental Science, 2017.
- 252. Wenzel, S., et al., *Interphase formation on lithium solid electrolytes-An in situ approach to study interfacial reactions by photoelectron spectroscopy.* Solid State Ionics, 2015. **278**: p. 98-105.
- 253. Santhanagopalan, D., et al., *Interface Limited Lithium Transport in Solid-State Batteries*. Journal of Physical Chemistry Letters, 2014. **5**(2): p. 298-303.
- 254. Sakuda, A., A. Hayashi, and M. Tatsumisago, *Intefacial Observation between LiCoO2 Electrode and Li2S-P2S5 Solid Electrolytes of All-Solid-State Lithium Secondary Batteries Using Transmission Electron Microscopy*. Chemistry of Materials, 2010. **22**(3): p. 949-956.

- 255. Vieira, E., et al. Flexible solid-state Li-ion battery using Ge thin film anode and LiCoO2 cathode. in 26th Micromechanics and Microsystems Europe Conference (MME2015). 2015.
- 256. Du, F.M., et al., *All solid state lithium batteries based on lamellar garnet-type ceramic electrolytes.* Journal of Power Sources, 2015. **300**: p. 24-28.
- 257. Aboulaich, A., et al., *A New Approach to Develop Safe All-Inorganic Monolithic Li-Ion Batteries*. Advanced Energy Materials, 2011. **1**(2): p. 179-183.
- 258. West, W.C., et al., Reduction of charge-transfer resistance at the solid electrolyte electrode interface by pulsed laser deposition of films from a crystalline Li2PO2N source. Journal of Power Sources, 2016. **312**: p. 116-122.
- 259. Ohta, N., et al., *LiNbO 3-coated LiCoO 2 as cathode material for all solid-state lithium secondary batteries*. Electrochemistry communications, 2007. **9**(7): p. 1486-1490.
- 260. Wang, C.W., et al., Conformal, Nanoscale ZnO Surface Modification of Garnet-Based Solid-State Electrolyte for Lithium Metal Anodes. Nano Letters, 2017. **17**(1): p. 565-571.
- 261. Kitaura, H., et al., Fabrication of electrode-electrolyte interfaces in all-solid-state rechargeable lithium batteries by using a supercooled liquid state of the glassy electrolytes. Journal of Materials Chemistry, 2011. **21**(1): p. 118-124.
- 262. Fabre, S.D., et al., *Charge/discharge simulation of an all-solid-state thin-film battery using a one-dimensional model.* Journal of the Electrochemical Society, 2011. **159**(2): p. A104-A115.
- 263. Chu, K.T. and M.Z. Bazant, *Electrochemical thin films at and above the classical limiting current.* Siam Journal on Applied Mathematics, 2005. **65**(5): p. 1485-1505.
- 264. Zadin, V., et al., Modelling electrode material utilization in the trench model 3D-microbattery by finite element analysis. Journal of Power Sources, 2010. **195**(18): p. 6218-6224.
- 265. Landstorfer, M., S. Funken, and T. Jacob, *An advanced model framework for solid electrolyte intercalation batteries*. Physical Chemistry Chemical Physics, 2011. **13**(28): p. 12817-12825.
- 266. Bucci, G., et al., Measurement and modeling of the mechanical and electrochemical response of amorphous Si thin film electrodes during cyclic lithiation. Journal of the Mechanics and Physics of Solids, 2014. **62**: p. 276-294.
- 267. Klinsmann, M., et al., *Modeling Crack Growth during Li Extraction in Storage Particles Using a Fracture Phase Field Approach*. Journal of the Electrochemical Society, 2016. **163**(2): p. A102-A118.

- 268. Yang, Y.H., et al., Elastic Properties, Defect Thermodynamics, Electrochemical Window, Phase Stability, and Li+ Mobility of Li3PS4: Insights from First-Principles Calculations. Acs Applied Materials & Interfaces, 2016. **8**(38): p. 25229-25242.
- 269. Qu, M., et al., *Nanomechanical Quantification of Elastic, Plastic, and Fracture Properties of LiCoO2*. Advanced Energy Materials, 2012. **2**(8): p. 940-944.
- 270. Wang, Y. and Y.-T. Cheng, *A nanoindentation study of the viscoplastic behavior of pure lithium*. Scripta Materialia, 2017. **130**: p. 191-195.
- 271. Munichandraiah, N., L. Scanlon, and R. Marsh, *Surface films of lithium: an overview of electrochemical studies*. Journal of power sources, 1998. **72**(2): p. 203-210.
- 272. Iriyama, Y., et al., Reduction of charge transfer resistance at the lithium phosphorus oxynitride/lithium cobalt oxide interface by thermal treatment. Journal of power sources, 2005. **146**(1): p. 745-748.
- 273. Yamada, I., et al., *Lithium-ion transfer on a Li x CoO 2 thin film electrode prepared by pulsed laser deposition—effect of orientation.* Journal of Power Sources, 2007. **172**(2): p. 933-937.
- 274. Hertz, H. and J.R. Angew, Math, 1882. 92: p. 156.
- 275. Greenwood, J. and J. Williamson. *Contact of nominally flat surfaces*. in *Proceedings of the Royal Society of London A: Mathematical, Physical and Engineering Sciences*. 1966. The Royal Society.
- 276. Bush, A., R. Gibson, and T. Thomas, *The elastic contact of a rough surface*. Wear, 1975. **35**(1): p. 87-111.
- 277. Karan, S. and B. Mallik, *Power spectral density analysis and photoconducting behavior in copper(II) phthalocyanine nanostructured thin films*. Physical Chemistry Chemical Physics, 2008. **10**(45): p. 6751-6761.
- 278. Itoh, T. and N. Yamauchi, Surface morphology characterization of pentacene thin film and its substrate with under-layers by power spectral density using fast Fourier transform algorithms. Applied Surface Science, 2007. **253**(14): p. 6196-6202.
- 279. Flys, O., et al., *Characterization of surface topography of a newly developed metrological gloss scale*. Surface Topography-Metrology and Properties, 2015. **3**(4): p. 10.
- 280. Wang, X.H., et al., Self-stratified semiconductor/dielectric polymer blends: vertical phase separation for facile fabrication of organic transistors. Journal of Materials Chemistry C, 2013. **1**(25): p. 3989-3998.
- 281. Persson, B.N.J., *Contact mechanics for randomly rough surfaces*. Surface Science Reports, 2006. **61**(4): p. 201-227.

- 282. Park, M., et al., *A review of conduction phenomena in Li-ion batteries*. Journal of Power Sources, 2010. **195**(24): p. 7904-7929.
- 283. Chen, B., et al., *A new composite solid electrolyte PEO/Li10GeP2S12/SN for all-solid-state lithium battery.* Electrochimica Acta, 2016. **210**: p. 905-914.
- 284. Nakayama, M., et al., Factors affecting cyclic durability of all-solid-state lithium polymer batteries using poly(ethylene oxide)-based solid polymer electrolytes. Energy & Environmental Science, 2010. **3**(12): p. 1995-2002.
- 285. Jackle, J. and K. Kawasaki, *Intrinsic roughness of glass surfaces*. Journal of Physics: condensed matter, 1995. **7**(23): p. 4351.
- 286. Zeng, K.Y. and J. Zhu, Surface morphology, elastic modulus and hardness of thin film cathodes for Li-ion rechargeable batteries. Mechanics of Materials, 2015. **91**: p. 323-332.
- 287. Bouwman, P.J., et al., *Influence of diffusion plane orientation on electrochemical properties of thin film LiCoO2 electrodes.* Journal of the Electrochemical Society, 2002. **149**(6): p. A699-A709.
- 288. Patil, V., et al., *LiCoO2 thin film cathodes grown by sol-gel method*. Journal of Electroceramics, 2009. **23**(2-4): p. 214-218.
- 289. Cho, S.I. and S.G. Yoon, *Characterization of LiCoO2 thin film cathodes deposited by liquid-delivery metallorganic chemical vapor deposition for rechargeable lithium batteries.*Journal of the Electrochemical Society, 2002. **149**(12): p. A1584-A1588.
- 290. Zhu, J., et al., *In situ study of topography, phase and volume changes of titanium dioxide anode in all-solid-state thin film lithium-ion battery by biased scanning probe microscopy.* Journal of Power Sources, 2012. **197**: p. 224-230.
- 291. Barreca, D., et al., *Cobalt Oxide Nanomaterials by Vapor-Phase Synthesis for Fast and Reversible Lithium Storage*. Journal of Physical Chemistry C, 2010. **114**(21): p. 10054-10060.
- 292. Zhang, X., et al., *Diagnostic characterization of high power lithium-ion batteries for use in hybrid electric vehicles*. Journal of the Electrochemical Society, 2001. **148**(5): p. A463-A470.
- 293. Ramdon, S. and B. Bhushan, *High resolution morphology and electrical characterization of aged Li-ion battery cathode*. Journal of Colloid and Interface Science, 2012. **380**: p. 187-191.
- 294. Persson, B.N., *Theory of rubber friction and contact mechanics*. The Journal of Chemical Physics, 2001. **115**(8): p. 3840-3861.
- 295. Lorenz, T., et al., *Theoretical Study of the Mechanical Behavior of Individual TiS2 and MoS2 Nanotubes*. Journal of Physical Chemistry C, 2012. **116**(21): p. 11714-11721.

- 296. Xiao, X.R., W. Wu, and X.S. Huang, *A multi-scale approach for the stress analysis of polymeric separators in a lithium-ion battery*. Journal of Power Sources, 2010. **195**(22): p. 7649-7660.
- 297. Zhu, J., K.Y. Zeng, and L. Lu, Cycling effects on surface morphology, nanomechanical and interfacial reliability of LiMn2O4 cathode in thin film lithium ion batteries. Electrochimica Acta, 2012. **68**: p. 52-59.
- 298. Lorenz, B., et al., *Adhesion: role of bulk viscoelasticity and surface roughness*. Journal of Physics-Condensed Matter, 2013. **25**(22): p. 16.
- 299. Hertz, H.R., Über die Berührung fester elastischer Körper und über die Härte. 2006.
- 300. Shi, S.Q., et al., Defect Thermodynamics and Diffusion Mechanisms in Li2CO3 and Implications for the Solid Electrolyte Interphase in Li-Ion Batteries. Journal of Physical Chemistry C, 2013. 117(17): p. 8579-8593.
- 301. Sethuraman, V.A., et al., *In situ measurements of stress-potential coupling in lithiated silicon*. Journal of The Electrochemical Society, 2010. **157**(11): p. A1253-A1261.
- 302. Lee, S.W., et al., *Fracture of crystalline silicon nanopillars during electrochemical lithium insertion.* Proceedings of the National Academy of Sciences, 2012. **109**(11): p. 4080-4085.
- 303. Koerver, R., et al., *Chemo-mechanical expansion of lithium electrode materials—on the route to mechanically optimized all-solid-state batteries*. Energy & Environmental Science, 2018. **11**(8): p. 2142-2158.
- 304. Behrou, R. and K. Maute, *Numerical modeling of damage evolution phenomenon in solid-state lithium-ion batteries*. Journal of The Electrochemical Society, 2017. **164**(12): p. A2573-A2589.
- 305. Deshpande, R., Y.-T. Cheng, and M.W. Verbrugge, *Modeling diffusion-induced stress in nanowire electrode structures*. Journal of Power Sources, 2010. **195**(15): p. 5081-5088.
- 306. Siegel, J.B., et al., *Expansion of lithium ion pouch cell batteries: Observations from neutron imaging.* Journal of The Electrochemical Society, 2013. **160**(8): p. A1031-A1038.
- 307. Barai, P., et al., *Reduced order modeling of mechanical degradation induced performance decay in lithium-ion battery porous electrodes.* Journal of The Electrochemical Society, 2015. **162**(9): p. A1751-A1771.
- 308. Yang, H., et al., *A chemo-mechanical model of lithiation in silicon*. Journal of the Mechanics and Physics of Solids, 2014. **70**: p. 349-361.
- 309. Miehe, C., et al., *A phase-field model for chemo-mechanical induced fracture in lithium-ion battery electrode particles*. International Journal for Numerical Methods in Engineering, 2016. **106**(9): p. 683-711.

- 310. Roberts, S.A., et al., A framework for three-dimensional mesoscale modeling of anisotropic swelling and mechanical deformation in lithium-ion electrodes. Journal of The Electrochemical Society, 2014. **161**(11): p. F3052-F3059.
- 311. Huttin, M. and M. Kamlah, *Phase-field modeling of stress generation in electrode particles of lithium ion batteries*. Applied Physics Letters, 2012. **101**(13): p. 133902.
- 312. Li, J., et al., A single particle model with chemical/mechanical degradation physics for lithium ion battery State of Health (SOH) estimation. Applied energy, 2018. **212**: p. 1178-1190.
- 313. Thangadurai, V., S. Narayanan, and D. Pinzaru, *Garnet-type solid-state fast Li ion conductors for Li batteries: critical review.* Chemical Society Reviews, 2014. **43**(13): p. 4714-4727.
- 314. Agrawal, R. and G. Pandey, *Solid polymer electrolytes: materials designing and all-solid-state battery applications: an overview.* Journal of Physics D: Applied Physics, 2008. **41**(22): p. 223001.
- 315. Sun, C., et al., *Recent advances in all-solid-state rechargeable lithium batteries*. Nano Energy, 2017. **33**: p. 363-386.
- 316. Song, J., Y. Wang, and C.C. Wan, *Review of gel-type polymer electrolytes for lithium-ion batteries*. Journal of power sources, 1999. **77**(2): p. 183-197.
- 317. Hassoun, J. and B. Scrosati, *Moving to a solid-state configuration: a valid approach to making lithium-sulfur batteries viable for practical applications*. Advanced Materials, 2010. **22**(45): p. 5198-5201.
- 318. Koerver, R., et al., Capacity fade in solid-state batteries: interphase formation and chemomechanical processes in nickel-rich layered oxide cathodes and lithium thiophosphate solid electrolytes. Chemistry of Materials, 2017. **29**(13): p. 5574-5582.
- 319. Thangadurai, V. and W. Weppner, *Li6ALa2Ta2O12* (*A*= *Sr*, *Ba*): novel garnet-like oxides for fast lithium ion conduction. Advanced Functional Materials, 2005. **15**(1): p. 107-112.
- 320. Yu, X., et al., *A stable thin-film lithium electrolyte: lithium phosphorus oxynitride.* Journal of the electrochemical society, 1997. **144**(2): p. 524-532.
- 321. Doyle, M., T.F. Fuller, and J. Newman, *Modeling of galvanostatic charge and discharge of the lithium/polymer/insertion cell.* Journal of the Electrochemical society, 1993. **140**(6): p. 1526-1533.
- 322. Fick, A., *V. On liquid diffusion*. The London, Edinburgh, and Dublin Philosophical Magazine and Journal of Science, 1855. **10**(63): p. 30-39.
- 323. Probstein, R.F., *Physicochemical hydrodynamics: an introduction*. 2005: John Wiley & Sons.

- 324. Bard, A.J., et al., *Electrochemical methods: fundamentals and applications*. Vol. 2. 1980: wiley New York.
- 325. Sethuraman, V.A., V. Srinivasan, and J. Newman, *Analysis of electrochemical lithiation and delithiation kinetics in silicon*. Journal of the Electrochemical Society, 2013. **160**(2): p. A394-A403.
- 326. Jain, A., et al., Commentary: The Materials Project: A materials genome approach to accelerating materials innovation. Apl Materials, 2013. 1(1): p. 011002.
- 327. Ong, S.P., et al., The Materials Application Programming Interface (API): A simple, flexible and efficient API for materials data based on REpresentational State Transfer (REST) principles. Computational Materials Science, 2015. 97: p. 209-215.
- 328. Peled, E. and S. Menkin, *SEI: past, present and future.* Journal of The Electrochemical Society, 2017. **164**(7): p. A1703-A1719.
- 329. Wang, A., et al., Review on modeling of the anode solid electrolyte interphase (SEI) for lithium-ion batteries. npj Computational Materials, 2018. **4**(1): p. 15.
- 330. Lyalin, A., et al., *Lithiation of Silicon Anode based on Soft X-ray Emission Spectroscopy: A Theoretical Study*. arXiv preprint arXiv:1801.01983, 2018.
- 331. Kim, H., et al., *Structure and properties of Li– Si alloys: a first-principles study.* The Journal of Physical Chemistry C, 2011. **115**(5): p. 2514-2521.
- 332. Custer, J., et al., *Density of amorphous Si.* Applied physics letters, 1994. **64**(4): p. 437-439.
- 333. Cheng, E.J., et al., *Elastic properties of lithium cobalt oxide (LiCoO2)*. Journal of Asian Ceramic Societies, 2017. **5**(2): p. 113-117.
- 334. Lacivita, V., N. Artrith, and G. Ceder, *Structural and Compositional Factors That Control the Li-Ion Conductivity in LiPON Electrolytes*. Chemistry of Materials, 2018. **30**(20): p. 7077-7090.